Informes Técnicos Ciemat 1509
Setiembre, 2022

LABORATORY TESTS ON BENTONITE HOMOGENISATION PERFORMED BY CIEMAT: SATURATION OF BLOCK/PELLETS SYSTEMS (PROJECT BEACON)

Villar Galicia, M.V.
Iglesias Martínez, R.J.
Gutiérrez Álvarez, C.
Carbonell Barrios, B.
Real Fernández, E.
Brea Núñez, N.

GOBIERNO DE ESPAÑA
MINISTERIO DE CIENCIA E INNOVACIÓN
Ciemat
Centro de Investigaciones Energéticas, Medioambientales y Tecnológicas

Publication available in catalog of official publications

ISSN:2695-8864
NIPO:832-22-005-4

Edition and Publication:
Editorial CIEMAT
Avda. Complutense, 40 28040-MADRID
e-mail: editorial@ciemat.es
Editorial news

ENSAYOS DE LABORATORIO SOBRE HOMOGENEIZACIÓN DE BENTONITA REALIZADOS EN CIEMAT: SATURACIÓN DE BARRERAS BLOQUE/PELLETS (PROYECTO BEACON)

Villar Galicia, M.V.; Iglesias Martínez, R.J.; Gutiérrez Álvarez,C.; Carbonell Barrios, B.; Real Fernández, R.; Brea Núñez, N.

62 pp, 66 fig., 7 tbl., 49 ref., 1 An

Resumen:

Algunos conceptos de almacenamiento geológico de residuos nucleares consideran el uso de barreras de ingeniería constituidas por bloques de bentonita compactada sobre los que apoyar los contenedores, y un material de granular (pellets de bentonita) para rellenar el resto de la galería. El uso combinado de bloques y pellets en una misma sección de la barrera supone una dificultad adicional para la compresión y modelado de su funcionamiento. Para mejorar el conocimiento sobre la evolución hidro-mecánica de estos sistemas mixtos (bloque/pellets) como consecuencia de su hidratación, se ha llevado a cabo una serie de ensayos de laboratorio a escala decimétrica. En la mayoría de ellos se midió la entrada de agua y la presión axial en función del tiempo; en otros, realizados en celdas transparentes, fue posible seguir visualmente los cambios macroscópicos en la textura de la bentonia resultantes de la hidratación. Finalmente, en uno de los ensayos se midieron humedades relativas y presiones radiales. Este último se realizó con bentonita MX-80, y el resto con la bentonita española FEBEX. Al desmontar los ensayos después de diferentes tiempos de operación se analizó el estado físico de la bentonita y su microestructura.

LABORATORY TESTS ON BENTONITE HOMOGENISATION PERFORMED BY CIEMAT: SATURATION OF BLOCK/PELLETS SYSTEMS (PROJECT BEACON)

Villar Galicia, M.V.; Iglesias Martínez, R.J.; Gutiérrez Álvarez,C.; Carbonell Barrios, B.; Real Fernández, R.; Brea Núñez, N.

62 pp, 66 fig., 7 tbl., 49 ref., 1 an

Abstract:

Some deep geological nuclear waste disposal concepts are considering the installation around the waste canisters of bentonite barriers made up of two components: highly compacted blocks to support the canister and a granular buffer material consisting of bentonite pellets to fill the rest of the disposal gallery. The combined use of pellets and blocks in the same section of the barrier introduces difficulties in the understanding and modelling of the system performance. With the aim of obtaining information about the hydro-mechanical evolution of initially inhomogeneous bentonite samples (pellets/blocks) upon hydration under isothermal conditions, a series of laboratory tests in decimetre-scale cells was carried out. In most tests axial stress and water intake were measured over time; in others, performed in transparent cells, it was possible to visually follow the bentonite macroscopic changes upon hydration. Finally, in one of the tests, relative humidity and radial pressure were measured. Except for the latter, which was performed with MX-80 bentonite, all the other tests used the Spanish FEBEX bentonite. Upon dismantling the final physical state and microstructure of the samples were analysed.

ACKNOWLEDGEMENTS

The research leading to these results was financed by the Beacon project, which received funding from the Euratom Research and Training Programme 2014–2018 under grant agreement number 745942. The data acquisition system and the sensors' connection systems of test CT31 were prepared by Dr. José Miguel Barcala and the selection of sensors was done by Dr. Pedro Luis Martín, who also contributed to the design of tests in transparent cell. The mercury intrusion porosimetry tests were performed at the Petrophysical laboratory of CIEMAT. The XRD measurements were performed at the High-Level Radioactive Waste Unit of CIEMAT by L. Gutiérrez-Nebot. Juan Aroz and Guillermo García-Herrera participated at different phases in the laboratory work.

CONTENT

LIST OF FIGURES

LIST OF TABLES

1 INTRODUCTION

The backfilling and sealing of deposition galleries or holes and access galleries and shafts is an important part of the nuclear waste underground repository design. Openings created during the construction of the repository are potential preferential pathways for water, gas and radionuclides migration, and have to be effectively sealed. Bentonite or bentonite-based mixtures have been proposed as backfill and sealing materials for their low permeability, high swelling capacity and high retention capacity. To enhance these properties bentonite has to be compacted, and dry density values of between 1.45 and 1.65 g/cm^3 are usually considered appropriate to ensure the main safety functions of the clay barrier (Sellin and Leupin 2013). The design of clay barriers has been mainly based on using blocks of compacted bentonite and for this reason these materials have been widely characterised in the form of high-density pre-compacted blocks, which have also been used in large-scale experiments (e.g. Dixon et al. 2002, ENRESA 2006, SKB 2010).

The use of high-density bentonite pellets (combined or not with powdered bentonite) as barrier material was also proposed several decades ago (Salo & Kukkola 1989, Volckaert et al. 1996). The manufacturing of high-density pellets usually involves the pre-heating of bentonite powder so that a drier and more compressible material can be produced and compacted. The advantage of this material is that it is easy to manufacture and install: the bentonite pellets can be emplaced using auger discharge tubes or even pneumatic projection techniques. Thus, the backfilling operation becomes an easier and potentially robotised procedure. The initial works using pellets considered vertical emplacement of the canister. However, in the case of horizontal placement, a rigid support for the canister is needed, what can be achieved by the combined use of a lower bed made of highly compacted bentonite blocks in which the waste canister rests and an upper buffer made of granular bentonite material (GBM, i.e. pellets). This disposal concept has been adopted by the Swiss waste management agency, and is described in detail in NAGRA (2019) and references therein. The pellets/blocks construction concept was initially demonstrated in the large-scale Engineered Barrier Emplacement Experiment (EB), carried out at the Mont Terri URL, which is excavated in Opalinus Clay, using FEBEX bentonite to construct the two-component barrier (ENRESA 2005, García-Siñeriz et al. 2015).

In this context, the overall objective of the BEACON (Bentonite Mechanical Evolution) project is to evaluate the consequences of heterogeneities on the performance of bentonite barriers in geological repositories for high-level radioactive waste. Although the bentonite buffer shows a natural tendency towards homogenisation, long-term observations both in large-scale and in laboratory tests revealed that a degree of heterogeneity may persist (e.g. Villar et al. 2020, Bernachy-Barbe et al. 2020). In this respect, CIEMAT carried out in the framework of this project a series of tests in cells to evaluate one of the sources of bentonite heterogeneity: the combination in the same barrier of pellets and blocks of compacted bentonite, whose initial dry densities and structures noticeably differ. The aim of this investigation was to obtain qualitative and quantitative information about the evolution, at laboratory scale, of initially inhomogeneous bentonite samples (pellets/blocks) upon hydration under isothermal conditions. Both in the

laboratory and in the real case, this evolution might be affected by the characteristics of the barrier system (the particular dry density and water content of each barrier component as well as their sizes) and by the boundary conditions, such as the existence of gaps, temperature and water salinity and availability. In the present research two factors potentially affecting the mechanical evolution of a two-component barrier were analysed: water availability and barrier configuration. Thus, the tests were performed either under constant pressure conditions, simulating a repository excavated in crystalline host rock with plenty of water, such as the underground laboratory of Grimsel or under low water inflow rate, simulating a repository with scarce water availability, which would be the case of clay host rocks (Grambow 2016), such as the underground laboratory in Mont Terri. An additional variable analysed in this work was the influence of hydrating through the pellets or the block part.

Most of the tests were performed with FEBEX bentonite in a large-scale oedometer and in a transparent cell and were described and jointly analysed in an open published paper (Villar et al. 2021a), whose contents are approximately reproduced in the following subsections. Once the project had started a new large cell was fine-tuned and a similar test using MX-80 bentonite was mounted (test CT31) and the results are also presented in this report.

2 MATERIAL

2.1 FEBEX BENTONITE

The material used in the laboratory tests performed in the large-scale oedometer and the transparent cell was a bentonite extracted from the Cortijo de Archidona quarry (Almería, Spain) in two different phases. The first batch, known as FEBEX bentonite, was extracted in 1995 and is a granulate used to obtain the compacted blocks. The second batch was extracted in 2001 and was used to manufacture in a factory the pellets used in some tests.

The FEBEX bentonite was a 900-t batch of bentonite processed in 1996 for the FEBEX project. The processing consisted in homogenisation, air-drying and manual removing of volcanic pebbles on site and, at the factory, crumbling, drying in a rotary oven at temperatures between 50 and 60°C to a water content of around 13%, and sieving through a 5-mm mesh. The physico-chemical properties of the FEBEX bentonite, as well as its most relevant thermo-hydro-mechanical and geochemical characteristics were reported in ENRESA (2006) and updated in e.g. Villar (2017).

The smectite content of the FEBEX bentonite is close to 90 wt.%. The smectitic phases are actually made up of a montmorillonite-illite mixed layer, with 10-15 wt.% of illite layers. Besides, the bentonite contains variable quantities of quartz, plagioclase, K-felspar, calcite, and cristobalite-trydimite. The cation exchange capacity is 98±2 meq/100g, the main exchangeable cations being calcium (35±2 meq/100g), magnesium (31±3 meq/100g) and sodium (27±1 meq/100g). The predominant soluble ions are chloride, sulphate, bicarbonate and sodium.

The liquid limit of the bentonite is 102±4 %, the plastic limit 53±3 %, the density of the solid particles 2.70±0.04 g/cm^3, and 67±3 % of particles are smaller than 2 µm. The hygroscopic water content in equilibrium with the laboratory atmosphere (relative humidity 50±10%, temperature 21±3 °C) is 13.7±1.3%. The total specific surface area is about 725±47 m^2/g.

The saturated hydraulic conductivity of compacted samples of the FEBEX reference bentonite is exponentially related to their dry density. Two empirical relationships between hydraulic conductivity (k_w, m/s) and dry density (ρ_d, g/cm^3) were obtained for samples permeated with deionised water at room temperature, valid each for a different dry density range (Villar 2002):

$$\text{For } \rho_d > 1.47 \text{ g/cm}^3\text{: } \log k_w = -2.96\ \rho_d - 8.58 \quad [1]$$

$$\text{For } \rho_d < 1.47 \text{ g/cm}^3\text{: } \log k_w = -6.00\ \rho_d - 4.09 \quad [2]$$

The swelling pressure (P_s, MPa) of compacted samples is also exponentially related to the bentonite dry density, according to the empirical expression in Eq. 3 (Villar 2002):

$$\ln P_s = 6.77\ \rho_d - 9.07 \quad [3]$$

Relationships between suction and water content obtained for different bentonite dry densities under isochoric conditions can be found in e.g. Villar et al. (2019). For a sample compacted at dry density 1.6 g/cm^3 with hygroscopic water content the initial suction value would be ~120 MPa.

The pellets were prepared for the EB project (ENRESA 2005) using a 100-t batch of bentonite extracted in 2001 from the Cortijo de Archidona deposit. To manufacture the pellets the bentonite was dried and milled in a multi-step process to produce a fine grade powder with a water content of between 3.0 and 4.5%. Later, a commercial plant with an in-line highly automated briquetting process produced coarse (7-15 mm) and fine (0.05-2 mm) grained materials with dry densities of 2.11 and 2.13 g/cm^3, respectively (Kennedy et al. 2004). The different grain sizes were kept separated in the laboratory and mixed in the right proportion just before every test, trying to keep a Fuller's curve similar to that used for the EB project, with a maximum diameter of 12.7 mm and a minimum diameter of 0.425 mm, in order to reduce segregation. The mineralogical analyses performed in samples of test MGR25 (see below) suggest that the content of smectite of this batch could be lower than in the FEBEX batch, whereas the quartz, calcite and dolomite contents would be higher. The cationic exchange capacity was checked to be lower (e.g. Villar and Gómez-Espina 2012a). A detailed hydro-mechanical characterisation of this mixture was performed by Hoffmann (2005).

2.2 MX-80 BENTONITE

The test performed in the setup described in 3.2 was performed with a combination of an MX-80 bentonite block and a mixture of Wyoming-type bentonite pellets and powder in a mass ratio 70/30 (Figure 1). The block was obtained by powder compaction. The initial water content of the bentonite powder was 8.9% and of the pellets 6.2%. The powder had a grain size between 0.14 and 0.75 mm. The pellets had a regular, approximately spherical shape with a diameter of 7 mm and a dry density of 2.0 g/cm^3. They were supplied by AITEMIN in 2013 in the framework of the in situ test NSC, performed at the Bure URL in France. They were manufactured from the material with brand name WH2, but no detailed mineralogical characterisation of the pellets was provided by the suppliers nor performed at CIEMAT. Similar (but larger, ϕ=32 mm) pellets were used in the large-scale tests FSS (Bosgiraud & Foin 2016) and REM (Conil et al. 2015) and in the laboratory tests reported in Bernachy-Barbe et al. 2020). Bosgiraud & Foin 2016 characterised also the 7-mm diameter pellets, and found for them a dry density of 2.00 g/cm^3, a water content of 4.9% and a particle density of 2.78 g/cm^3 for the material from which they were produced.

The MX-80 bentonite is a brand name used by the American Colloid Company for sodium bentonite from Wyoming (USA), milled to millimetre-sized grains. The content of montmorillonite is between 65 and 90% (~70% for the batch used), with quartz, plagioclase and K-feldspars (contents between 4 and 15%), and minor quantities of cristobalite, tridymite, calcite, gypsum, pyrite, illite. Na^+ is the main exchangeable cation (50-74 meq/100 g), with also Ca^{2+} (10-30 meq/100 g) and Mg^{2+} (3-8 meq/100g). The main soluble ions are sodium and sulphate.

Figure 1 Appearance of MX-80 bentonite powder (left) and MX-80 pellets (right)

In the batch used to compact the block (Gómez-Espina & Villar 2016), the smectite content was 92%, the feldspars content 5% and the quartz content 1%, with traces of calcite, gypsum, dolomite, halite and pyrite. The smectitic phase was actually a montmorillonite-illite interstratified with 6-7% of illite layers. The cation exchange capacity was 77 meq/100g, the exchangeable sodium was 48 meq/100 g, the exchangeable calcium 33 meq/100 g and the exchangeable magnesium 8 meq/100 g.

The swelling pressure of small samples (3.8 or 5.0 cm in diameter, 1.2 cm in height) of MX-80 bentonite powder compacted with its hygroscopic water content was determined at CIEMAT at room temperature using deionised water as saturation fluid. The swelling pressure (P_s, MPa) could be related to final dry density (ρ_d, g/cm^3) through the following equation:

$$\ln P_s = 5.44\ \rho_d - 6.94 \qquad [4]$$

The hydraulic conductivity (k_w, m/s) of samples of powdered MX-80 bentonite (grain size <1 mm), compacted at different dry densities (ρ_d, g/cm^3) and kept in stainless steel cells which hindered the swelling of the material upon saturation, was measured in a constant head permeameter (Villar 2005). Deionised water was used as permeant. The following exponential relation between dry density (ρ_d, g/cm^3) and hydraulic conductivity (k, m/s) was found:

$$\log k_w = -2.94\ \rho_d - 8.17 \qquad [5]$$

3 METHODOLOGY

3.1 TESTS WITH FEBEX BENTONITE

Isochoric infiltration tests were performed in two-part samples (binary samples), half of them consisting of a bentonite compacted block and the other half of a pellet mixture. Two types of cells were used: a large-scale oedometer (MGR) and a transparent cell (CW). In most tests the lower half of the cell was filled with bentonite pellets with an average dry density close to 1.30 g/cm^3 and the upper part by a bentonite block of dry density 1.60 g/cm^3 (in two tests, CW2 and MGR27, the placement was in reverse). In all cases hydration with deionised water took place through the bottom. These kinds of tests were complementary: whereas MGR tests provided quantitative data, the information provided by the CW test was mostly visual and qualitative.

The materials used in all the tests were the FEBEX bentonite for blocks and the EB pellets (see section Material). The block part of the sample was compacted from the granulate material with its hygroscopic water content, ~14%, resulting in an initial suction of ~116 MPa. The different grain sizes of the pellets were kept separated in the laboratory and mixed in the right proportion just before every test. The lab run out of pellets larger than 9.5 mm, and the granulometric distribution of tests MGR23 to MGR27, and CW1 and CW2 was modified to keep the Fuller's curve (Table 1). Also, in tests MGR23 to MGR27 the pellets were softly dried to a water content closer to the fabrication one (3.5%), because the water content of the pellets increased during storage (to values as high as 10.6%). This resulted in a significant different initial suction between the pellets that were dried and those that were not, 380 *vs*. 114 MPa (measured with a capacitive sensor).

Sieve sizes (mm)	Percentage retained Test MGR21, MGR22 (%)	Percentage retained rest of tests (%)
9.50	17	0
4.75	31	37
2.00	26	31
1.18	11	13
0.59	10	12
0.43	5	6

Table 1. Granulometric curve of the pellets of bentonite used in the tests

3.1.1 LARGE-SCALE OEDOMETER

The large-scale oedometer (MGR test) consists of a cylindrical body with base and an upper piston that may move in the cylinder (Figure 2). The body has an inner diameter of 10.0 cm and the length of the sample inside was 10.0 cm. The top and bottom of the sample were in contact with filter papers and ceramic porous discs connected to outlets. The cell was placed in a rigid frame that guaranteed the constant volume of the sample by hindering the displacement of the piston. An external LVDT measured the potential axial displacements, whereas a 10-t load cell in the upper part of the frame measured the force developed by the specimen.

The bentonite block was directly compacted inside the cell and the pellets were poured on it and carefully shaken as necessary to get the target density (Figure 3). Then the cell was closed, overturned and mounted in the oedometric frame. The water intake took place thorough the bottom surface, either under a low injection pressure (a 1.5 m water column, 15 kPa, simulating reduced water intake conditions, e.g. Opalinus clay in Mont Terri) or under a constant low flow (0.05 cm^3/h), simulating a continuous contribution of water, e.g. Grimsel granite). In the first case the water intake was measured with an automatic volume change apparatus and in the second case with a pressure/volume controller. During hydration the top outlet remained open to atmosphere and the pressure exerted by the material, the sample deformation and the water intake were measured and automatically recorded. The tests were performed at laboratory temperature.

A summary of the tests performed and of their characteristics is given in Table 2.

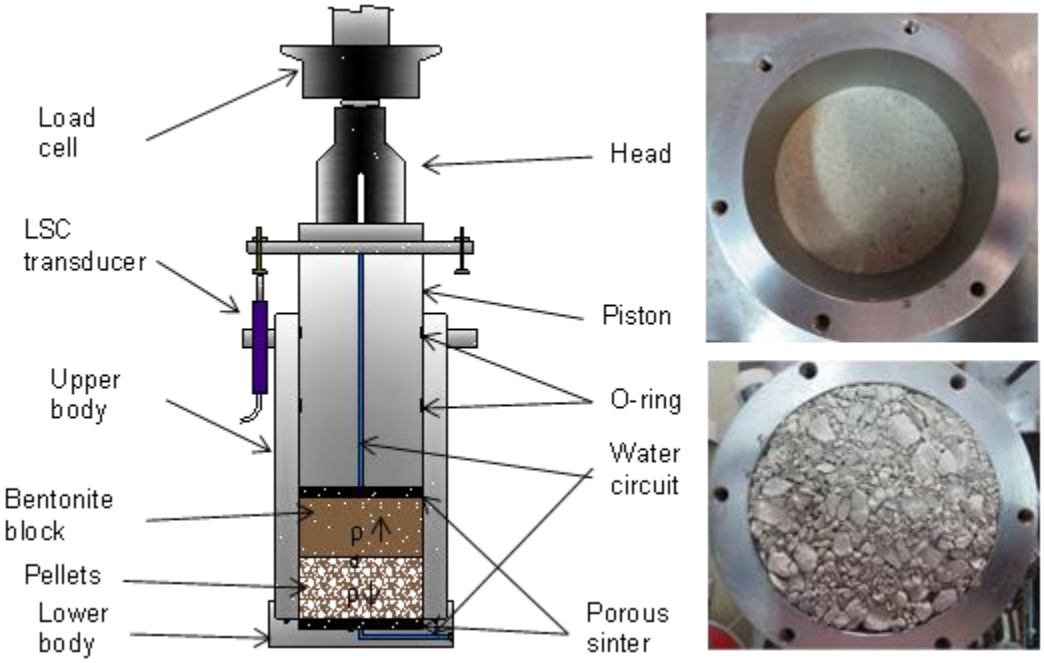

Figure 2. Schematic representation of the MGR cell (left) and images of the block (upper right) and pellets (lower right)

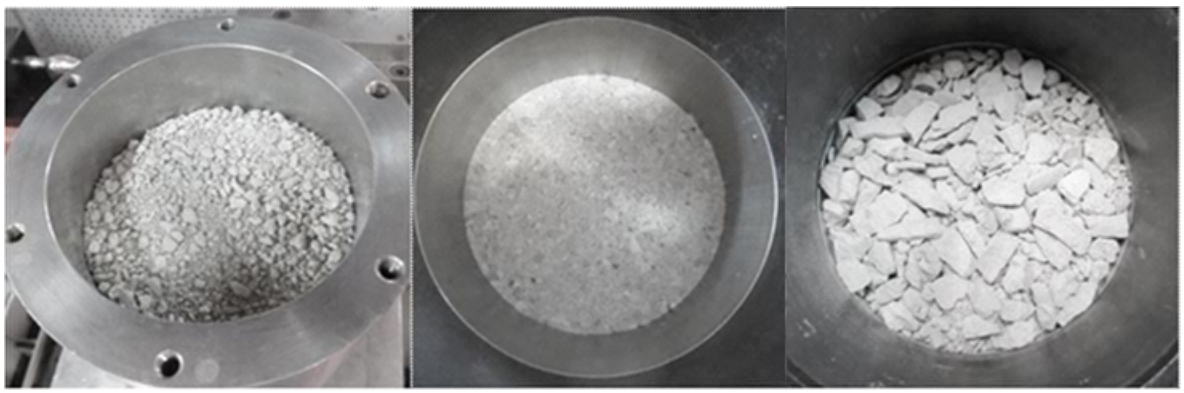

Figure 3. Appearance of the material used for the assembly of the test: Bentonite before compaction (left), compacted block (centre) and pellets filling the other half (right)

Test	Hydration	Duration (days)	Dates	*T* (°C)
MGR21	Constant pressure: 15 kPa (Pellets)	34	Aug – Sept 2017	23.1±0.6
MGR22	Constant flow: 0.05 cm^3/h (Pellets)	266	Oct 2017 – Jul 2018	22.5±1.3
MGR23	Constant pressure: 15 kPa (Pellets)	210	Aug 2018 – Mar 2019	22.6±1.5
MGR24	Constant pressure: 15 kPa (Pellets)	14	Mar – Apr 2019	22.5±0.6
MGR25	Constant pressure: 15 kPa (Pellets)	76	May – July 2019	22.7±1.1
MGR26	Constant flow: 0.05 cm^3/h (Pellets)	132	Sep 2019 – Jan 2020	23.6±1.2
MGR27	Constant pressure: 15 kPa (Block)	278	Feb – Nov 2020	23.0±1.2
MGR28	Constant pressure: 15 kPa (Block)	>535	Nov 2020 -	-

Table 2 Characteristics of the MGR tests

3.1.2 TRANSPARENT CELL

The transparent cell or window cell (CW) is a custom-built square cell consisting of two transparent methacrylate faces reinforced with steel frames (Figure 4). The inner dimensions of the central steel frame are 121x118x20 mm. A square block of the same dimensions was compacted in a bespoke mould and half sectioned. One of the halves was placed in the cell and the rest of the cell was homogeneously filled with the pellets while the cell was horizontally laid (Figure 5). During assembly the fine fractions moved towards the bottom. This side of the cell, which was at the bottom during assembly, was called B-face. As a result, the two faces, A and B, of the cell presented different appearance (Figure 6).

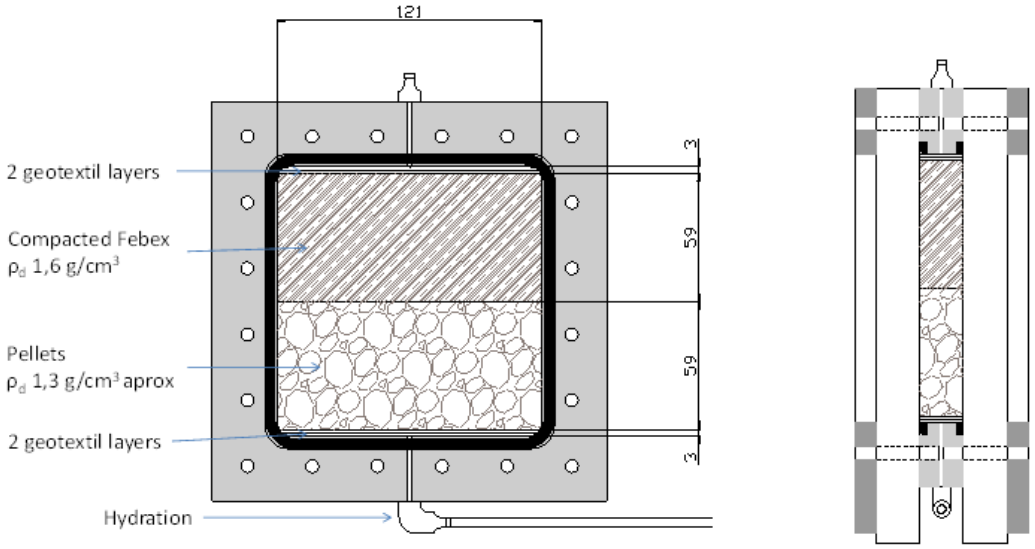

Figure 4. Schematic front and lateral views of the transparent cell (CW1 with pellets at the bottom, as shown in the Figure, and CW2 with pellets on top)

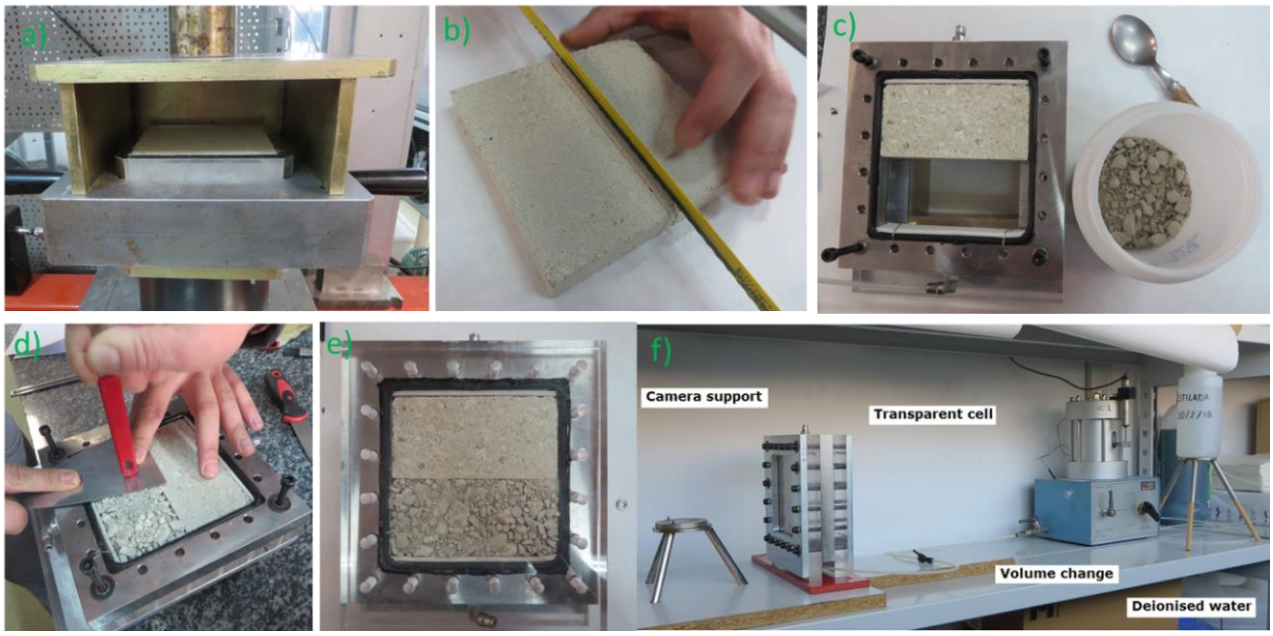

Figure 5. Procedure for transparent cell assemblage: a) compaction of a square bentonite block of dry density 1.6 g/cm^3; b) half sectioning of the block; c) block filling half of the cell and pellets to be poured in the other half with a spoon; d) filling of the other half of the cell with pellets (see Figure 6 for appearance of up and down faces); e) face A with methacrylate cover on before screwing it on the steel frame; f) whole experimental setup

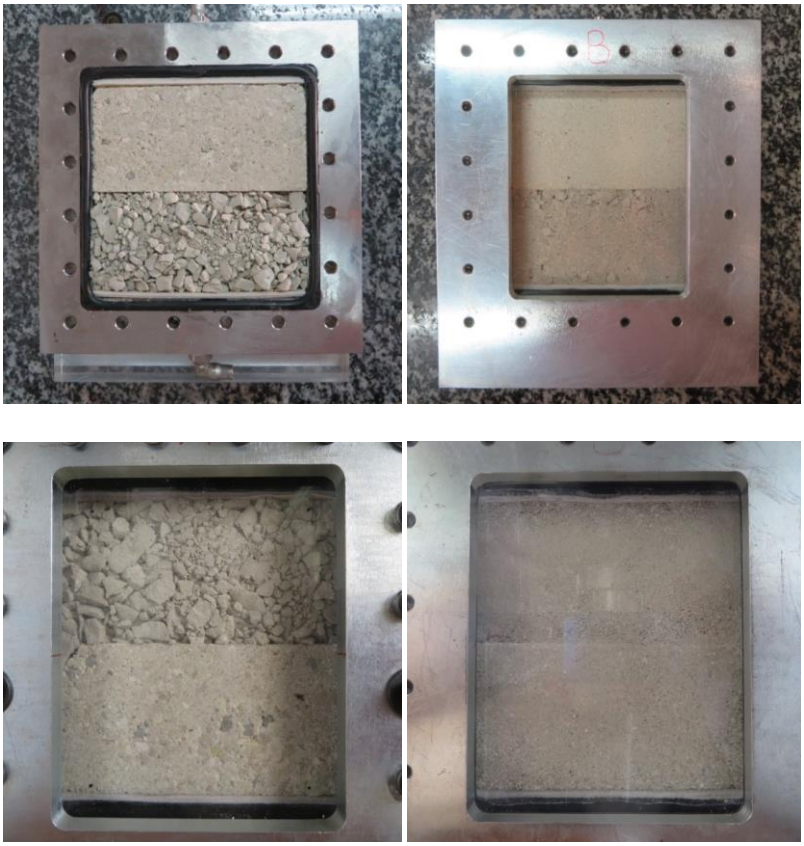

Figure 6. Initial appearance of face A (left) and B (right) of test CW1 (up) and CW2 (down)

In cell CW2, 4 small methacrylate beads were introduced as markers for the observation of possible movements during hydration (Figure 7).

Figure 7. Methacrylate beads, indicated in red circles (left) and their location within the cell

Two geotextile layers were placed at the upper and bottom sides of the cell. Hydration took place through the bottom with a 30 cm (3 kPa) water column, and the water intake was measured with an automatic volume change apparatus. The CW1 test had the pellets placed at the bottom, and inversely, in the CW2 test, the block was the first part hydrated. Photographs of both sides were periodically taken.

The characteristics of the tests are summarised in Table 3.

Test	Hydration	Duration (days)	Dates	*T* (°C)
CW1	Constant pressure: 3 kPa (Pellets)	379	Feb 2018 – Mar 2019	22.6±1.4
CW2	Constant pressure: 3 kPa (Block)	420	May 2019 –Jul 2020	23.5±1.2

Table 3. Characteristics of the CW tests

3.1.3 POSTMORTEM TESTS: PHYSICAL STATE AND MICROSTRUCTURE

At the end of the tests the bentonite samples were extracted from the cell (by pushing with a piston in the case of cell MGR), measured, weighed, and cut in regular horizontal sections. Each section was subsampled to determine water content, dry density and pore size distribution. Also, the specific surface area and the smectite basal spacing were determined in some samples. The cylindrical blocks from MGR tests were sliced in 6 horizontal levels (3 for pellets and 3 for block). The CW samples were cut into 15 parts (5 rows and 3 columns). The subsamples were numbered from top to bottom, i.e. sample #1 was the one farther away from the hydration surface.

The gravimetric water content (w) is defined as the ratio between the mass of water and the mass of dry solid expressed as a percentage. The mass of water was determined as the difference between the mass of the sample and its mass after oven drying at 110°C for 48 hours. Dry density (ρd) is defined as the ratio between the mass of the dry sample and the volume occupied by it prior to drying. The volume of the specimens was determined by immersing them in a recipient containing mercury and by weighing the mercury displaced, considering a density of mercury of 13.6 g/cm^3.

The pore size distribution of subsamples was determined by mercury intrusion porosimetry (MIP). The samples were put in the ice condenser of a Telstar LioQuest equipment at -30°C for 3 hours. Subsequently, they were lyophilised for 22 hours at a temperature of -50°C under a vacuum of 0.2 mbar, so that to sublimate the water in the pores. Thereafter, they were heated at 25-30°C for 3 hours. These samples were kept in a desiccator until the MIP analysis. The porosimeter used was a Micromeritics AutoPore Series IV 9500, which allowed the exploration of pore diameters between 0.007 and 600 µm. Prior to mercury injection the sample was outgassed by applying a vacuum of 50 µm-Hg. Afterwards the mercury injection pressure was increased from 2.7 kPa to 220 MPa in 109 steps. To determine the extrusion branch of the curve, the pressure was released in 56 steps down to a pressure of 68.6 kPa. A contact angle of mercury of 139° both on advancing and of receding on the clay surface was considered.

The specific surface area of the bentonite samples from all the tests (except MGR21 and MGR22) was determined using the BET method (Brunauer et al. 1938) to analyse the adsorption isotherms of nitrogen gas in the solid at the temperature of liquid nitrogen (77 K, -196°C). This parameter represents the external surface area (a_s), i.e. the surface of the intra-aggregate and inter-aggregate voids but not that of the interlayer space. The sorption isotherms were determined in an ASAP 2020 of Micromeritics. The unaltered samples were lyophilised prior to degassing and then finely ground. Samples of between 0.6 and 2.1 g were degassed at 90°C for the time necessary to reach a vacuum of 50 µm Hg, which was kept for 10 min. Afterwards the samples were kept at 90°C under vacuum for 8 h, to eliminate moisture and impurities retained in the pores. The isotherms obtained had 58 points, 35 in the range of relative pressures between 0.01 and 0.99 (adsorption) and 23 points in the range between 0.99 and 0.14 (desorption). The BET method was applied in the range of P/P_0 0.06-0.2 to compute the specific surface area.

The (001) reflection or basal reflection gives the distance along the crystallographic *c*-axis between clay lamellae, and for a given clay mineral, it depends on the exchangeable cations present in the interlayer and their degree of hydration. The samples of some of the tests were preserved in paraffined foil and the X-ray profile of a plane surface of them was registered at laboratory temperature after removing the foil and without any further treatment. An anode of Cu (CuKα) radiation was used with a Bruker D8 Advance diffractometer at 40 mA and 40 kV operating conditions. XRD experimental profiles were obtained with a 1-mm entrance slit, 0.05°2θ step size and a counting time of 3 s per step. Data were collected between 2 and 30°2θ. The divergence slit and diffracted beam slit of the goniometer were fixed at 1 mm. The Pearson VII profile function was fitted to the observed intensities in order to obtain better reflection parameters and to deconvolute overlapped reflections. For the samples of tests MGR27 and CW2, an anthicatode of Cu (CuKα) radiation was used with a Philips model X'Pert-MPD diffractometer (Bragg Brentano configuration) at 40 mA, 45 kV operating condition. X-ray diffraction (XRD) experimental profiles were obtained with a fixed divergence slit size 0.6 mm, receiving slit size 5 mm and and a scanning rate of 0.025°2θ/s. Data were collected between 2 and 10°2θ. The goniometer settings were: automatic divergence slit and diffracted beam slit 2 mm. The position of the diffraction reflections was adjusted by using the quartz in the samples as an internal standard. The complete mathematical description of the scan pattern was obtained by combination of a polynomial

function that describes the background and a profile function that fits the experimental reflections. The pseudo-Voigt profile function was used to fit the diffraction reflections as well as to deconvolute overlapped reflections.

3.1.4 GAS TESTING

Additionally, in tests CW cylindrical subsamples were obtained by drilling across the block/pellet interface to measure the gas breakthrough pressure as an indicator of the sealing quality of the interface. This subsample was vertically crossed by the interface (Figure 8). The core diameter was fit to 3.8 cm by using a cutting ring and knife. Filter paper and porous stones were placed on top and bottom of the sample and it was laterally wrapped in double latex membranes. Vacuum grease was applied between membranes in order to prevent the loss of gas. The wrapped sample was placed in a triaxial cell which was filled with de-aired water and pressurized to ensure perfect adherence of the membranes to the surface of the sample and avoid gas transport along it. The cell inlet at the upper part of the sample was connected to a nitrogen gas cylinder applying the gas injection. The outlet of the cell connected to the bottom of the sample was open to atmosphere, with a series of different range gas mass flowmeters measuring the gas outflow. More experimental details about the equipment and the equations used to compute permeability are given in Villar et al. (2018, 2021b). Gas was applied through face A (that of coarser granulometry, Figure 6). The particular test procedure was adapted to the characteristics of the samples. In test CW1 the injection pressure was increased until outflow occurred and in test CW2 the confining pressure was increased until flow stopped.

The pore size distribution of subsamples obtained after gas testing was also determined.

Figure 8. Appearance of the cylindrical sample obtained for gas testing in test CW1

3.2 TESTS WITH MX-80 BENTONITE

3.2.1 EXPERIMENTAL SETUP

The test using binary mixtures of MX-80 pellets and block were performed in a setup mounted specifically for BEACON once the project had started. The experimental setup consists of an instrumented cell, hydration system and control and data acquisition systems (Figure 9). A detailed description of the experimental setup and sensors' characteristics is given in Villar et al. (2022), and a summary of them is provided below.

A stainless steel cell was used to contain the bentonite. The internal dimensions were 15 cm of diameter and 14.5 cm of height. Figure 10 shows a blueprint of the cell, in which the location of RH/T sensors, pressure sensors and pore pressure sensor is indicated. The sample was hydrated through a porous stone at the bottom. The cell is instrumented with capacitive-type sensors placed inside the clay at three different levels (13, 78 and 128 mm from the bottom porous stone). The transmitters used are VAISALA HMT337, which include a humidity sensor (HUMICAP®) that changes its dielectrical characteristics with extremely small variations in humidity (capacitive-type RH sensor). They also include a temperature sensing element (Pt 100). The accuracy of the humidity sensor is ±1% over the range 0-90 percent RH and ±2% over the range 90-100 percent RH. The sensors are protected by cylindrical stainless steel filters (HM47280SP, length 41.5 mm). Radial pressures at the lateral bentonite cylinder interface are measured at the same distances from the bottom plate as those for the RH/T transmitters (i.e. 13, 78 and 128 mm). The pressure sensors used are XPM10 with a range of 0-100 bar (error 0.5 bar). The pore pressure is measured on top of the cell with a PMP 4070 Druck Amplified Output Pressure Transducer. Its operating absolute pressure range is 700 mbar up to 7 bar with an accuracy of ±0.08% FS.

The hydration system consists of a GDS volume/pressure controller connected to a control PC. Hydration took place with deionized water injected at a constant pressure of 0.014 MPa through a porous plate placed at the bottom of the cell.

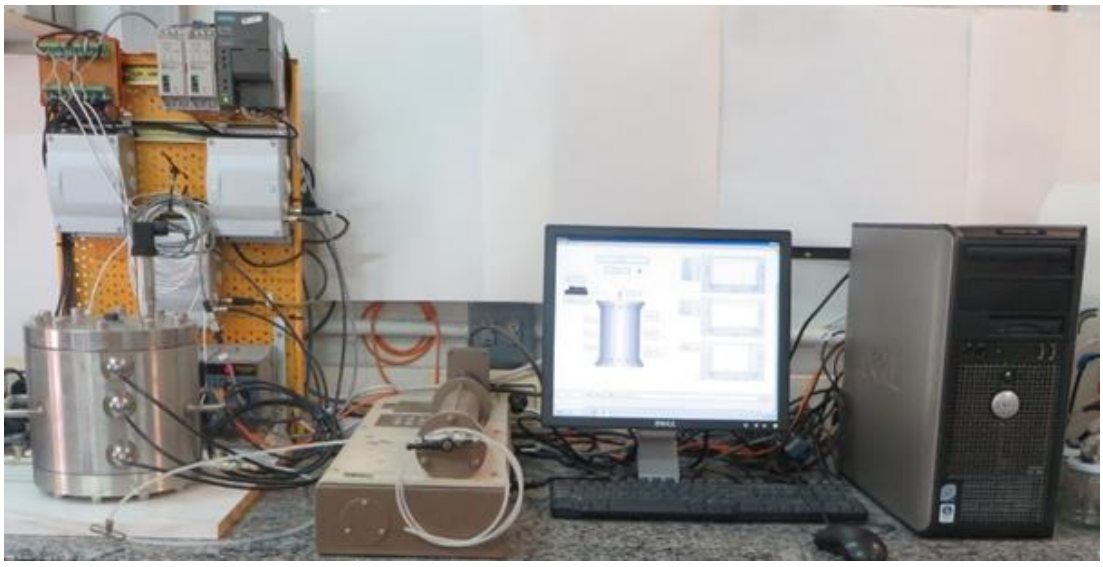

Figure 9. General setup for tests with MX-80 binary mixtures

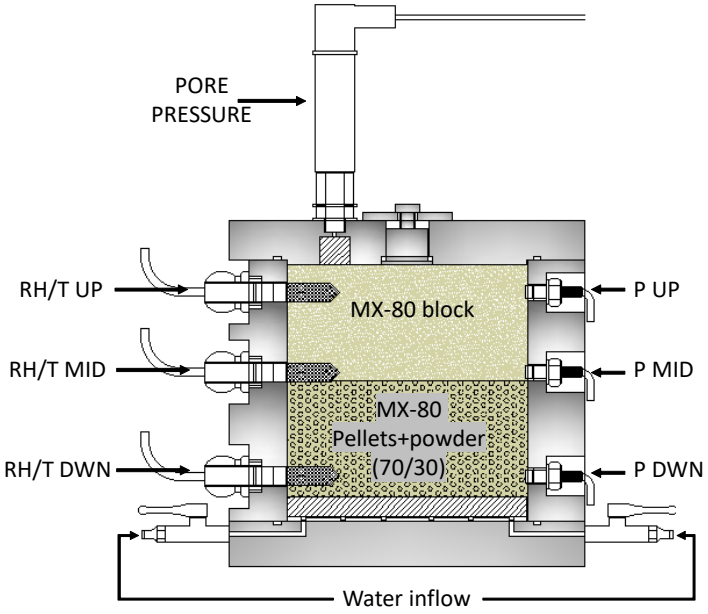

Figure 10. Longitudinal cross-section of the cell with the sensors installed according to the configuration for test CT31

3.2.2 EXPERIMENTAL PROCEDURE

The test was performed with the bentonite compacted block in the upper part and the pellets/powder mixture at the bottom part of the cell (Figure 10).

The block was compacted at a dry density of 1.5 g/cm^3 inside of the cell body placed upside down using a uniaxial pressure of 11.4 MPa. Then the other half of the cell was filled with the mixture of pellets and MX-80 powder (Figure 1). This mixture was arranged in 8 layers in such a way that the powder filled the gaps between the pellets. Each layer consisted of a first level with 1/3 of powder (~26 g), a second level with the pellets (~179 g), and a third level with the remaining 2/3 of powder (~52 g). During the process, light blows were given to readjust the particles so that the mass necessary to reach the target dry density of 1.50 g/cm^3 could fit inside. Once a layer was completed, a light pressure was applied to the mixture surface using a circular plate of the same diameter as the cell, so that to get an even layer surface. A total of 1433 g of pellets (1349 g dry mass) and 629 g of powder (578 g dry mass) were used for the mixture part. The bottom RH/T sensor was inserted as the cell was being filled.

The initial characteristics of the material inside the cell, including water content (w), dry density (ρ_d), degree of saturation (S_r) and height (h) can be seen in Table 4.

Materials	w (%)	h (cm)	ρ_d (g/cm^3)	S_r (%)	Volume (cm^3)	Dry mass (g)
Pellets/Powder mixture	7.0	7.20	1.50	23	1281.3	1,927.2
Block	8.9	7.25	1.49	29	1286.7	1,934.0
Average / (Total)	8.0	14.45	1.50	26	2568.0	3,861.1
After drilling	-	-	-	-	2568.0	3,845.6

Table 4. Initial characteristics of the materials of test CT31

After filling the cell, the sensors were installed. To insert the RH/T sensors, the bentonite was drilled with a bit of the same diameter as the sensors' (12 mm). The material expelled during drilling was recovered and weighed. Afterwards, the sensors were quickly inserted. The pore pressure sensor was fixed to the upper lid of the cell. The pressure sensors were screwed to the cell body in contact with the external surface of the bentonite cylinder. Hydration started six days after the cell was assembled. During this time the RH inside the block slightly decreased, whereas that of the mixture (bottom) slightly increased. This effect was triggered by the initial difference in water content of both materials (8.9 *vs*. 7.0%). The RH values measured just before hydration were between 41% close to the bottom to 43% on top.

When the test was finished and the cell was dismantled, the postmortem analyses described in section 3.1.3 were carried out.

4 RESULTS

In the following subsections the results are presented grouped by type of test or determination, but detailed records of each individual test, including Tables with numerical results, can be found in the Annex.

4.1 LARGE-SCALE OEDOMETER (FEBEX)

4.1.1 HYDRATION PROCESS: ONLINE RESULTS

Water intake, axial pressure and vertical deformation were continuously measured during hydration. Vertical deformation was minimal, since the movement of the piston was blocked by the oedometer framework. In fact the changes in overall dry density occurred as a result of the small vertical deformation allowed were in all cases below 0.005 g/cm^3. The tests were stopped and dismantled after different periods of time to get the temporal evolution of the postmortem information. Tests MGR22 and MGR23 continued until a pressure plateau was reached.

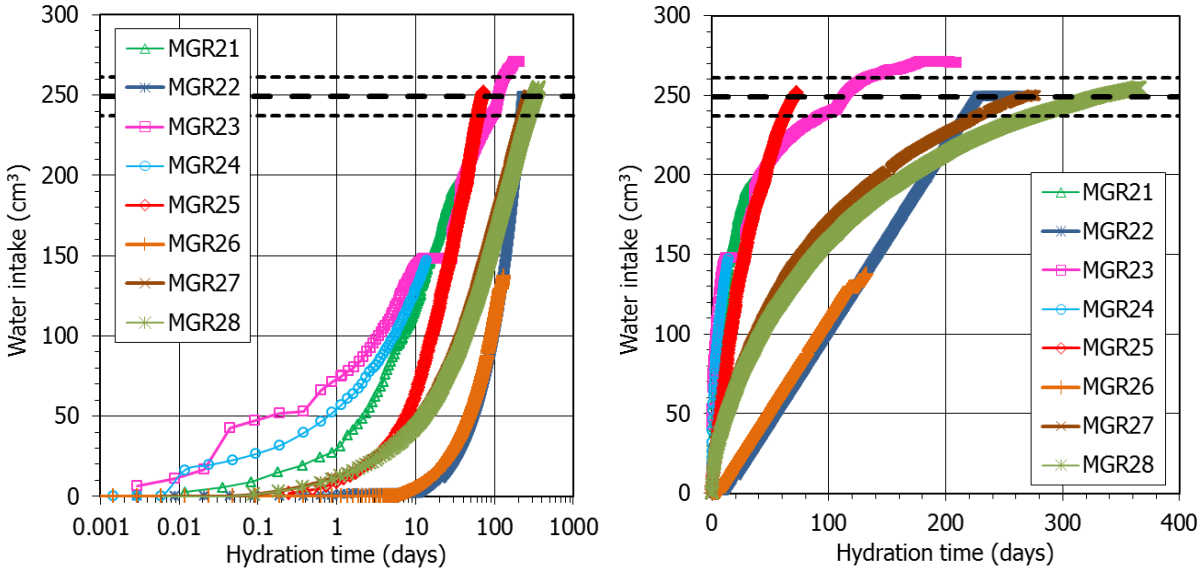

Figure 11. Water intake evolution in the large-scale oedometer tests (constant flow was prescribed in tests MGR22 and MGR26). The thick horizontal lines indicate the water intake necessary to reach full saturation (average and standard deviation). In tests MGR22 and MGR26 the water intake includes partly the intake of the bottom porous stone (6-14 cm^3)

Figure 11 shows the evolution of water intake for the seven MGR tests along with the water weight necessary to reach full saturation (250±12 g), which was not the same in all the tests because of the slight differences among them in initial dry density and water content. Some of the tests reached full saturation. There was a significantly different behaviour between the tests performed under constant injection pressure (MGR21, MGR23, MGR24 and MGR25) and the tests performed under constant water inflow rate (MGR22 and MGR26). In the constant-pressure tests the water intake was very quick and more than half of the water volume necessary for full saturation was taken in about 20 days, which was probably caused by the high permeability of the

pellets part. In contrast, the water intake was much slower in the two tests in which constant flow was prescribed, and it took more than 100 days to reach degrees of saturation close to 50%. The water intake rate in tests MGR27 and MGR28, in which hydration took place through the block part of the column (which was placed at the bottom), was initially intermediate between that of tests performed under constant pressure and those performed under constant inflow. However, they showed the slowest water intake rate in the long run, attesting the lower permeability of the higher density block. Some of the differences among the tests, particular concerning the initial water intake, were likely caused by experimental artefacts. In test MGR23 there was a short period (~14 days) during which no water was supplied to the cell because air entered the hydration line. As shown in Figure 12, this did not affect the swelling pressure evolution.

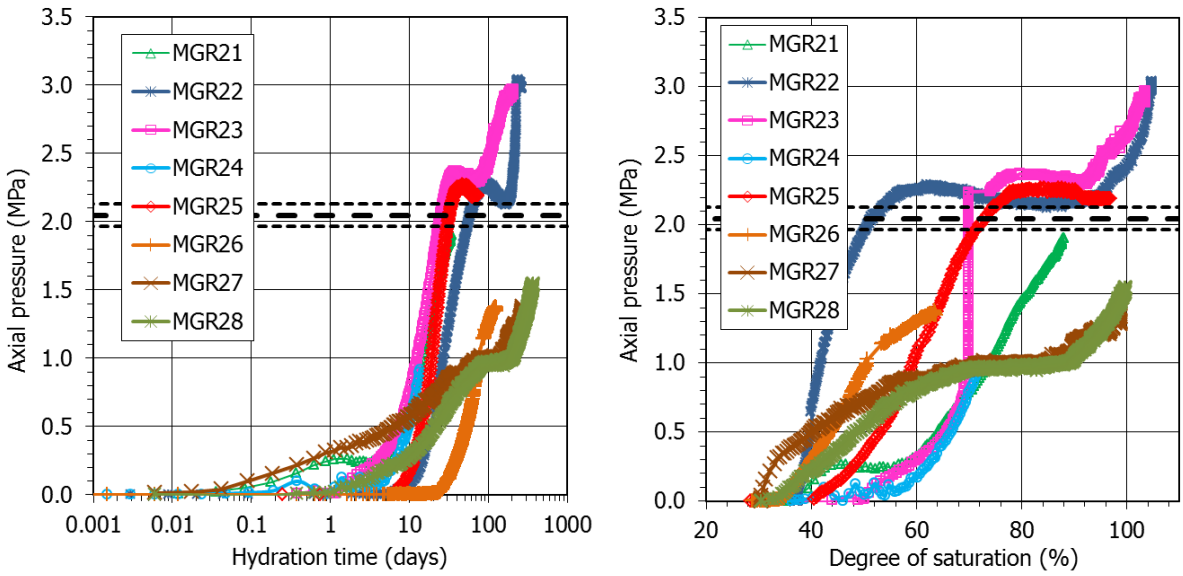

Figure 12. Axial pressure evolution over time (left) and as a function of the degree of saturation (right) in the large-scale oedometer tests (constant flow was prescribed in tests MGR22 and MGR26). The thick horizontal lines indicate the expected swelling pressure according to Eq. 2 (average and standard deviation)

Figure 12 shows the axial pressure development over time and as a function of the overall degree of saturation. The degree of saturation shown in the Figure is an overall value for the two-component samples but, at any given time, the actual degrees of saturation at different points along the sample height were very different, as the postmortem determinations presented in section 4.1.2 showed. In terms of temporal evolution, the axial pressure build up was generally steep at the beginning. In the longer tests, after the initial peak there was a soft decrease in axial pressure that eventually recovered and continued increasing after final stabilisation. The initial pressure peak occurred for degrees of saturation close to 80% in tests MGR23 and MGR25. In test MGR23 the period of time during which the axial pressure significantly increased with no change in the degree of saturation corresponds to the ~14 days period during which inadvertently no water was supplied to the cell. The fact that pressure continued to build up would indicate that water redistribution inside the bentonite can cause pressure increase. In contrast, in test MGR22, performed under controlled flow conditions, the peak in axial pressure was reached for a degree

of saturation of only ~60%. This would mean that slow saturation was more efficient, in the sense that it allowed a better water redistribution inside the microstructure.

After the sharp initial increase (the peak was reached after 30-40 days), in the longest test (MGR23) there was an intermediate stage of slight pressure decrease, and when the average degree of saturation was ~90% the axial pressure steadily increased again until full saturation was reached, with a stable pressure value of 3 MPa. Interestingly, in the two tests performed with saturation through the block (MGR27 and MGR28), the sharp increase in axial pressure build-up took also place after the degree of saturation had reached ~90%. Test MGR22 went also on until full saturation was reached. Since in this test the inflow was very low and controlled, the pressure development kinetics was very different to the other tests. Axial pressure started to develop slightly later than in the other tests (after 10 days), and when the degree of saturation was much lower than in the other tests (37%). The first peak was reached after 80 days and the intermediate stage lasted until 200 days had elapsed. During this time the degree of saturation increased from 58 to 96%. In the final stage, the water injection pressure started to increase because the P/V controller was not able to keep a constant low injection flow into a quasi-saturated sample without increasing the injection pressure (Figure 13). As a result, there was a new steep increase in axial pressure until the final value of 3 MPa. When the water injection pressure had increased to 1.5 MPa, water injection was stopped and the pressure was allowed to dissipate for 38 days. This explains the odd final shape of the curves for test MGR22. During this period of water injection pressure decline, the axial pressure did not change.

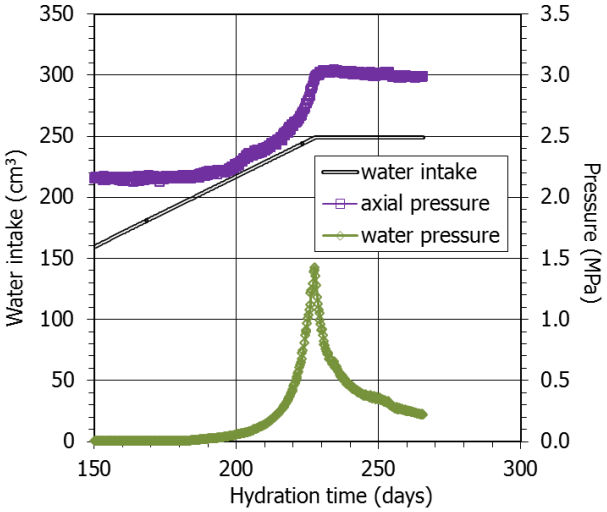

Figure 13. Final stage of test MGR22

4.1.2 FINAL PHYSICAL STATE

The tests were dismantled after different running times. Once the test was finished, the sample was extracted, measured, weighed and photographed before proceeding to its separation into two halves (the part corresponding to the pellets, and the block part). The final appearance of the samples once extracted from the cell is shown in Figure 14 for the tests performed under constant pressure hydration through the pellets and in Figure 15 for the others. The sample from the shorter test (MGR24) shows a quite saturated bottom in which the pellets cannot be told apart,

but the upper part of the pellets half still showed open voids. The two halves of this sample (pellets and block) could easily be detached. In the other cases the two halves were sealed and had to be separated with a knife (Figure 16). Already after 76 days the pellets half looked homogeneous. In contrast, in the tests performed under constant inflow rate, after 132 days (test MGR26) some pellets could still be told apart. In test MGR27 (saturated through the block), although the block looked saturated, the pellets upper part still presented voids from the initial fabric.

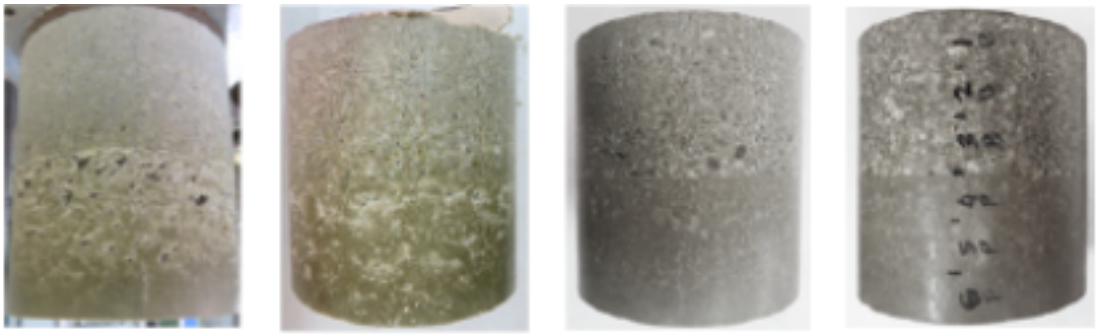

MGR24: 14 days MGR21: 34 days MGR25: 76 days MGR23: 210 days

Figure 14. Appearance of the MGR samples at the end of the tests performed under constant water injection pressure

MGR26: 132 days MGR22: 266 days MGR27: 278 days

Figure 15. Appearance of the MGR samples at the end of the tests performed under constant water inflow rate (MGR22, MGR26) and with saturation through the block (MGR27)

Figure 16. Separation of hydrated zones of block and pellets for sampling

Each of the halves indicated above was divided into 3 subsections numbered from 1 (upper part) to 6 (bottom part, closest to hydration), including a B for the sections belonging to the block part (1 to 3, except in MGR27), and a P for those belonging to the pellets part (4 to 6, except in MGR27). These six subsections were subsampled for the different determinations indicated in 3.1.3 (Figure 17). Table 5 shows a summary of the final characteristics of the samples, along with the initial values. The original height of the halves changed during the tests: the height of the bottom, pellets half decreased whereas the height of the upper block half increased, indicating the increase in the overall dry density of the pellets and decrease in the dry density of the block. These changes are illustrated in Figure 18 and were confirmed by the postmortem determination of dry density in the six horizontal sections. The water content of the bottom part (pellets) increased very quickly, but over time tended to decrease. In contrast, the dry density of the pellets half increased in a more continuous way. The behaviour of test MGR26 performed under constant flow (lasting 132 days) did not follow the overall trend, since the increase in water content was moderate and similar for both halves, attesting the more homogeneous water redistribution allowed by slow hydration. The two longest tests, which were performed under constant water inflow (MGR22) or with the block at the bottom (MGR27) should be separately considered. When hydration took place through the block, the final water content and dry density of both halves were more homogeneous.

Figure 17. Example of sample breakdown for different post-mortem determinations

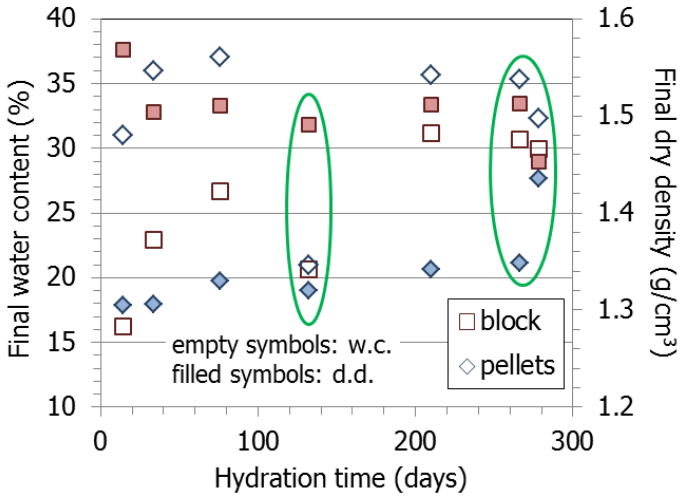

Figure 18. Final average water content and dry density of the block and pellet halves of the samples (the values circled correspond to tests performed under constant inflow rate (MGR22, MGR26) or with the block at the bottom (MGR27)

	Initial				Final			
	w (%)	h (cm)	ρ_d (g/cm^3)	S_r (%)	w (%)	ρ_d (g/cm^3)	h (cm)	S_r (%)
Test: MGR21, 34 days								
Pellets	9.5	4.97	1.26	23	35.9	1.31	4.80	91
Block	13.3	5.01	1.60	52	22.9	1.50	5.33	78
Total[a]	11.6	9.98	1.43	35	29.0	1.43	10.00	88
Test: MGR22, 266 days								
Pellets	9.9	5.04	1.28	24	35.3	1.35	4.79	95
Block	13.6	4.94	1.61	55	30.7	1.51	5.27	106
Total[a]	11.9	9.98	1.45	37	32.7	1.44	10.01	101
Test: MGR23, 210 days								
Pellets	3.5	5.00	1.30	9	35.7	1.34	4.84	95
Block	14.2	4.98	1.60	56	31.1	1.51	5.29	107
Total[a]	9.4	9.98	1.45	29	33.2	1.45	10.01	103
Test: MGR24, 14 days								
Pellets	5.7	5.02	1.28	14	31.0	1.3	4.93	78
Block	13.7	4.97	1.62	55	16.2	1.57	5.13	61
Total[a]	10.1	9.99	1.45	32	23.0	1.45	10.00	72
Test: MGR25, 76 days								
Pellets	3.2	4.99	1.30	8	37.0	1.33	4.88	97
Block	14.1	5.00	1.59	54	26.7	1.51	5.24	92
Total[a]	9.2	9.99	1.44	29	31.4	1.44	10.02	97
Test: MGR26, 132 days								
Pellets	3.5	5.01	1.30	9	21.0	1.32	4.92	54
Block	13.9	4.99	1.60	55	20.6	1.49	5.35	69
Total[a]	9.2	10.00	1.45	29	20.8	1.44	10.07	64
Test: MGR27, 278 days								
Pellets	3.0	5.00	1.31	8	32.3	1.43	4.55	99
Block	15.3	5.00	1.59	59	30.0	1.45	5.47	94
Total[a]	9.80	10.0	1.45	30	31.7	1.5	10.02	99

[a] the initial values are the averages of block and pellets, the final values correspond to online measurements (except in test MGR22)

Table 5. Initial and final characteristics of MGR tests

The water content, dry density and degree of saturation values measured in subsamples are plotted in Figure 19 to Figure 21 as a function of the distance to the hydration surface. The initial values are indicated by thick horizontal lines. The differences in the initial water content of the pellets were caused because in tests MGR23 to MGR27, prior to mounting, the pellets were dried to the values they had after they were manufactured. During the tests the water content and degree of saturation decreased from the hydration surface (sample bottom) upwards whereas the dry density increased. These gradients attenuated over time, hence they were smoother as the test duration was longer. The pellets/block interface did not seem to have any effect on the continuous gradients. The final dry density and water content values were similar in tests MGR22 and MGR23, despite the different hydration conditions (constant flow or pressure). Although the bentonite was finally fully saturated, the dry density and water content along the samples did not completely equalise. In contrast, test MGR26, which was far from full saturation, showed a quite homogeneous water content distribution, whereas the difference between the dry density of pellets and block was still significant.

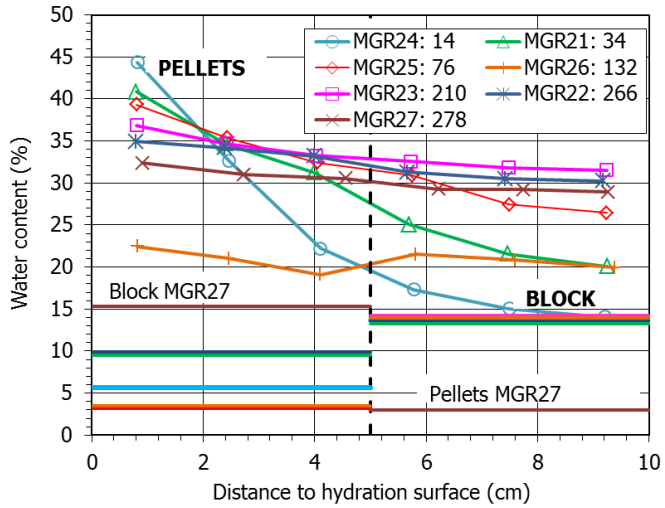

Figure 19. Final water content along the samples of MGR tests. The duration of the tests is given in days in the legend. The thick horizontal lines mark the initial value

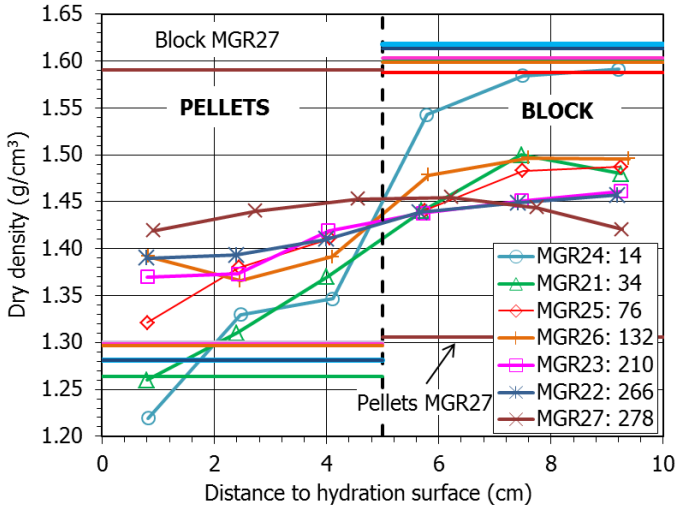

Figure 20. Final dry density along the samples of MGR tests. The duration of the tests is given in days. The thick horizontal lines mark the initial value

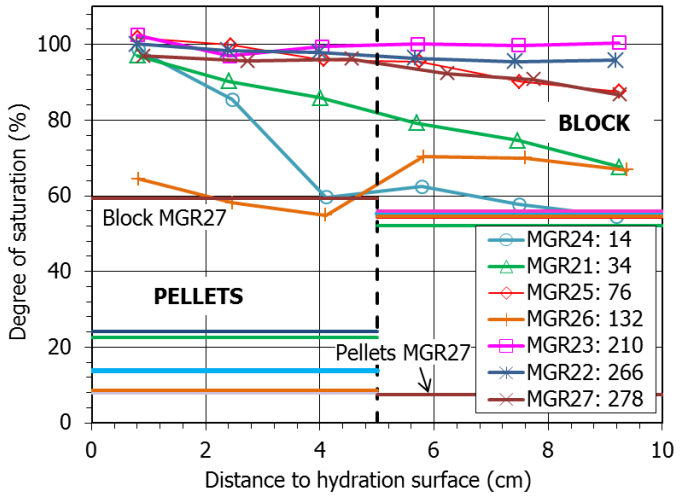

Figure 21. Final degree of saturation along the samples of MGR tests. The duration of the tests is given in days in the legend. The thick horizontal lines mark the initial value

4.1.3 MICROSTRUCTURAL CHANGES

4.1.3.1 PORE SIZE DISTRIBUTION (MIP)

The pore size distribution of the samples was determined by mercury intrusion porosimetry (MIP). In some subsamples duplicates were tested. In the sections below, the intrusion curves obtained in some of the samples are shown. In all of them the usual two pore families of compacted FEBEX bentonite corresponding approximately to pores larger and smaller than 200 nm could be told apart. This limit is not the same as that between macropores and mesopores, which according to the classification of Sing et al. (1985) would be at 50 nm. There is also discussion on the criteria that can be followed to select this delimiting value (Yuan et al. 2020). The 'valley' criterion was chosen in this work, consisting of using the lowest point of the valley between the two peaks of a bimodal distribution. In several THM models, this pore size represents the limit separating inter-aggregate from intra-aggregate pores, the latter not affected by density changes.

The mercury intrusion method allows access to be gained only to part of the macroporosity (pores of diameter smaller than ~550 μm) and to part of the mesopores (those of diameters larger than 7 nm), since mercury does not intrude the microporosity (pores of a size of less than 2 nm, according to the same classification mentioned above). Actually, the percentage of pores intruded by mercury in the samples analysed in this work was between 30 and 76%. Considering that most of the non-intruded porosity corresponds to the pores of a size smaller than the limit of the apparatus (7 nm), an estimation of the percentage of pores actually intruded can be made by comparing the actual void ratio of the samples (*e*, computed from their dry density and density of solid particles) and the apparent void ratio calculated from mercury intrusion (*e**). There is uncertainty in this approach, since it is possible that pores larger than 7 nm were not intruded because of the bottleneck effect: the pores connected to the external surface by narrow openings will not be intruded until sufficient pressure is applied to intrude the entryways. All of the volume of such pores will be allocated to the threshold radius class of the most restricted part of the entryway, which will result in an overestimation of the smaller pore sizes volume. Likewise, although in compacted clay materials pores larger than those that can be quantified by MIP are not expected, pores of this size could be present in some of the driest pellets samples.

Figure 22 shows the intrusion curves for FEBEX samples of the same characteristics as the initial conditions used in the cells (block and pellets). For the block part, the curve corresponding to a sample compacted at dry density 1.60 g/cm^3 with a water content of 14% was used as representative of the initial state. For the GBM, mixtures of different-size pellets having approximately a Fuller's curve grain size distribution, with a resulting dry density of 1.3 g/cm^3 and water contents of 10 and 3% were used. The initial GBM curves showed a predominant pore size around 300 μm (smaller for the higher water content mixture). The Figure also shows the pore size distribution corresponding to single pellets of two different water contents, with no powder addition. The distribution for pore sizes below ~10 μm is similar for the pellets and for the GBM, but for larger pores there is a huge difference, since the individual pellets do not have large pores. Despite the low density of the pellets mixtures, the percentage of non-intruded porosity in them

was very high (~70%). In this case not all the non-intruded porosity can be ascribed to pores smaller than 7 nm, because in the dry, low-density pellets mixtures large pores are also to be expected. Hence, an estimation of the volume of pores larger than 550 µm was made following this approach (Villar et al. 2021a):

At the beginning of a MIP test the calibrated sample holder is filled with mercury under a low injection pressure. Considering the sample mass and the volumes of the sample holder and of mercury intruded, the dry density of the sample is computed by the equipment software. This initial mercury injection is considered by the equipment as the zero value for the rest of the MIP test, which actually starts when injection pressure is increased above this value. Thus, all the large porosity filled during this initial step is disregarded. The comparison between the dry density determined by the equipment at this step and the actual dry density of the sample allows computing the volume of pores larger than 550 µm: when the sample contains a significant volume of large pores, the dry density determined by the porosimeter is considerably higher than the actual dry density of the sample, whereas if there are not large pores the two values tend to be similar. Hence, in the dry pellets samples this difference was quite large, whereas in the saturated and high-density samples the differences found were not significant. This correction was done to the initial GBM and to those samples whose visual inspection clearly showed that contained large pores, namely samples MGR24-4, MGR24-5, MGR21-4 (Figure 14) and all the pellets samples from tests MGR26 (Figure 15) and CW2. The subsamples were numbered from top to bottom, i.e. sample #1 was the one farther away from the hydration surface.

Taking all the above into account, the void ratio corresponding to pores larger and smaller than 200 nm (e_M and e_m, macro and micro, respectively) was recalculated, assuming that the non-intruded porosity corresponded to pores smaller than the equipment injection capacity and, in some pellets samples, also to pores larger than 550 µm.

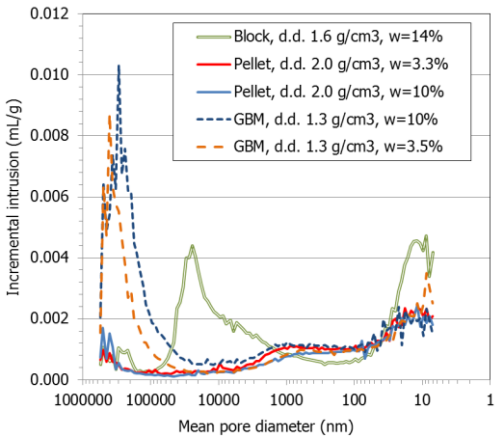

Figure 22. Pore size distribution expressed as incremental mercury intrusion of initial materials used in the MGR and CW tests (the legend includes the dry density and water content of the materials as used for the MIP tests)

The curves obtained for all the tests are presented in the Annex. As an example, Figure 23 and Figure 24 show the incremental curves of mercury intrusion for the subsamples of the tests lasting 14 (MGR24) and 210 days (MGR23). In the shorter test the pore size distribution of the

subsamples taken from the block half was similar to that of the initial block. Indeed, no relevant changes in the dry density and water content of the block samples took place during the oedometer test (only noticeable for the sample closest to the interface, 3b), because it was too short. This similarity proves the reliability of the technique. In contrast, the pore size distribution of the pellet half significantly changed. The size of pores larger than 200 nm and their volume decreased with respect to the initial pellets mixture. A similar pattern was found in test MGR21 (34 days). Overall, for the pellets subsamples of all the tests, the volume of pores larger than 200 nm significantly decreased, and the mean size of these macropores decreased from the initial ~300 µm to values mostly between 10 and 100 µm. This can also be observed in Figure 24 for the subsamples of the pellets half of the longer test (MGR23). In contrast, the mean size of the pores smaller than 200 nm increased with respect to the original values for all the pellets subsamples, as well as for the block subsamples (Figure 25). Furthermore, in the block subsamples the volume and size of the macropores also increased, except in the shorter, less saturated tests. This overall increase in the pore volume of all the size ranges for the block subsamples is related to the decrease in the global dry density of the block parts during the tests (Figure 20).

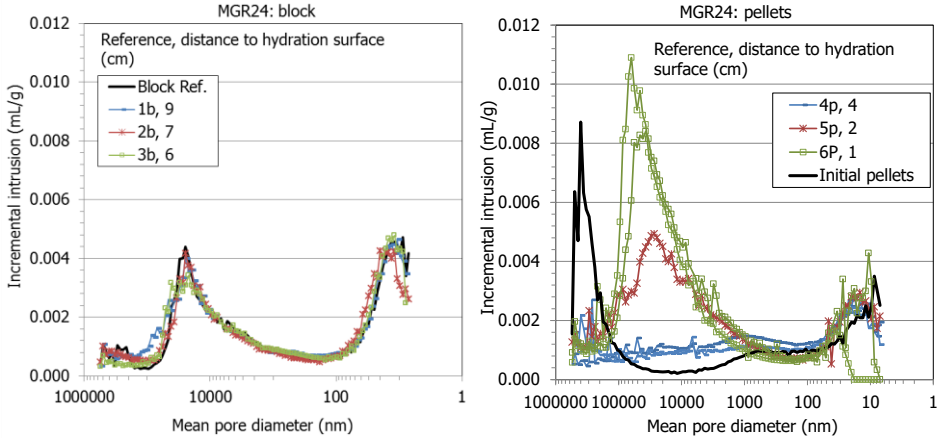

Figure 23. Pore size distribution expressed as incremental mercury intrusion of samples from test MGR24 (lasting 14 days), corresponding to the block (left) and pellets (right) halves. The curves for the initial materials (blocks and pellets) are included

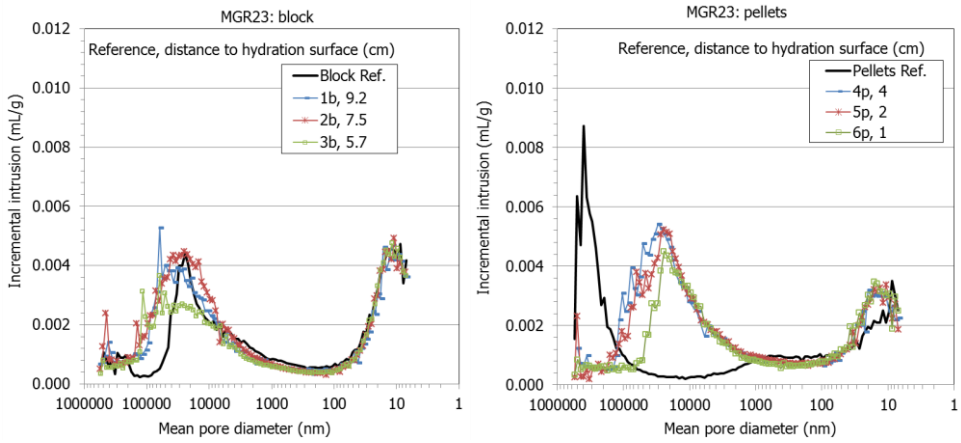

Figure 24. Pore size distribution expressed as incremental mercury intrusion of samples from test MGR23 (lasting 210 days), corresponding to the block (left) and pellets (right) halves. The curves for the initial materials (blocks and pellets) are included

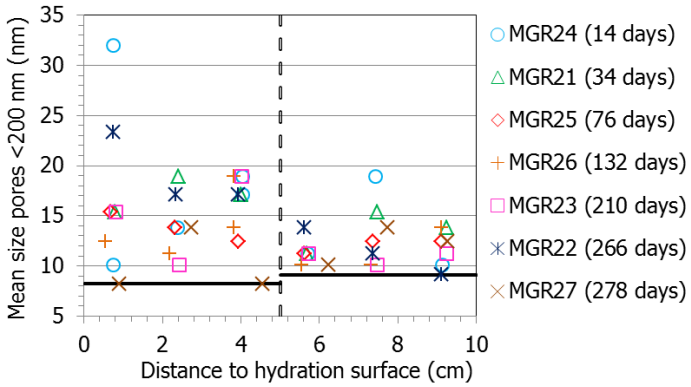

Figure 25. Mean size of pores smaller than 200 nm as determined by MIP (except in test MGR27, the pellets samples were at 0-5 cm from the hydration surface, and the block samples were at 5-10 cm from the hydration surface)

The void ratio corresponding to pores larger and smaller than 200 nm was recalculated as explained at the beginning of section 4.1.3. The ratio between the void ratio corresponding to pores smaller (e_m) and larger (e_M) than 200 nm increased in all samples with respect to the reference values, which reflects the increase in the volume of micropores as a result of hydration (Figure 26). This increase was much more significant for the pellets subsamples, except in the driest ones. In the block samples the largest proportion of void ratio corresponded to the pores of diameter smaller than 200 nm, and in fact for each test the largest e_m/e_M values tended to be in the block samples. The highest homogeneity in terms of e_m/e_M was reached in test MGR27, saturated through the block, which also had the most homogeneous dry density. The percentage of void ratio intruded, the void ratio corresponding to each pore size interval and the respective modes for the samples of all the tests are presented in Tables in the Annex.

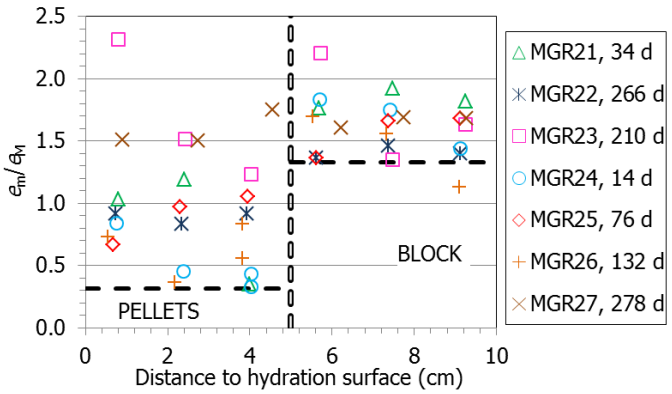

Figure 26. Ratio between void ratio corresponding to pores smaller and larger than 200 nm (e_m and e_M) obtained by MIP in subsamples from the MGR tests (the thick horizontal lines indicate the initial conditions for all the tests except MGR27, in which the position of pellets and block was inverted)

4.1.3.2 SORPTION ISOTHERMS

The BET specific surface area values measured in the samples of the tests were higher than the reference value in the half closest to hydration (pellets in all tests, except MGR27), and lower in the half farthest from this one (block in all tests, except MGR27). A general decreasing trend

towards the less hydrated areas was noticed (Figure 27). Similar trends were found for the t-plot micropore volume (Figure 28).

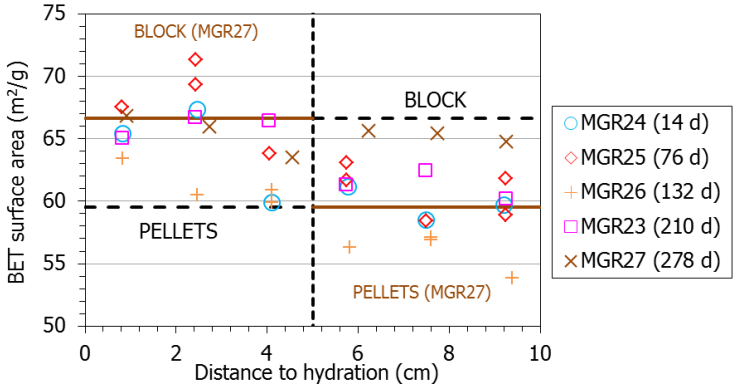

Figure 27. BET specific surface area as a function of the distance to the hydration surface. Horizontal lines indicate the reference values (MGR27 hydrated through the block)

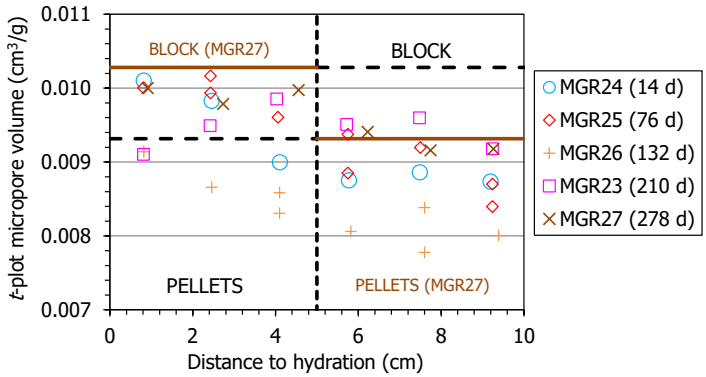

Figure 28. t-plot micropore volume as a function of the distance to the hydration surface. Horizontal lines indicate the reference values (MGR27 hydrated through the block)

Although the BET surface area depends on non-intrinsic factors such as the degree of grinding of the sample, previous researches have shown that it is closely related to water content (e.g. Villar 2017, for the FEBEX bentonite). Figure 29 shows the values measured in the different subsamples against their water contents, the increasing trend is clear. Also, for a given water content the values tended to be higher for the pellets than for the block samples. In contrast, as the previous figures showed, there is no correlation with the duration of the tests.

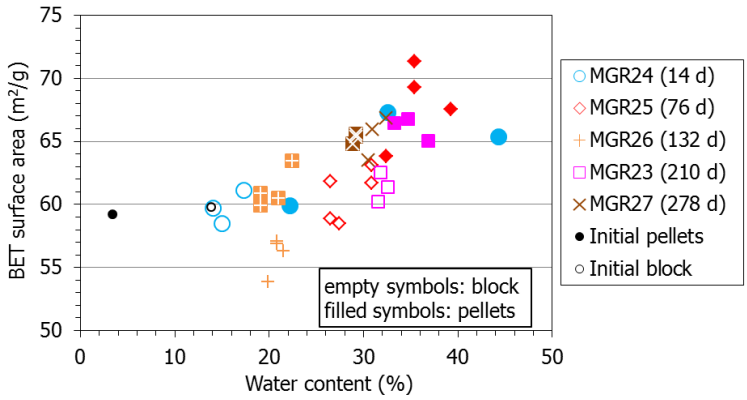

Figure 29. BET specific surface area as a function of water content of the samples. The duration of the tests is indicated in days

4.1.3.3 BASAL SPACING

The basal reflection of the subsamples after some MGR tests was determined by XRD. Fragments of the samples were X-rayed the same day in which the cells were dismantled, trying to keep the final water content unchanged by avoiding any accidental drying. The results obtained showed that the (001) reflection was a double one that could be decomposed into two diffraction reflections by profile fitting of the XRD patterns. In the case of the block samples the main diffraction reflection corresponded to the full development of the 2-layer hydrate (~1.5-1.7 nm) and the secondary one to the 3-layer hydrate (~1.8-1.9 nm), whereas in the pellets samples the main diffraction reflection corresponded to the full development of the 3-layer hydrate and the secondary reflection was higher (2.0-2.1 nm). However, the samples from test MGR24, the shortest one, showed a single diffraction reflection for the basal reflection at much lower values.

Figure 30 shows the values corresponding to the main reflections as a function of the distance to the hydration surface and as a function of the water content. The initial basal reflection for the pellets samples would be ~1.3 nm, and for the compacted block ~1.5 nm. For a given test, no matter its duration, the final values were higher in the pellets part. For the pellets samples with water content higher than 32% the values were all above 1.8 nm, practically corresponding to the 3 water layer hydration state of the smectite. In contrast, block samples of similar water content had lower basal spacings (lower than 1.7 nm).

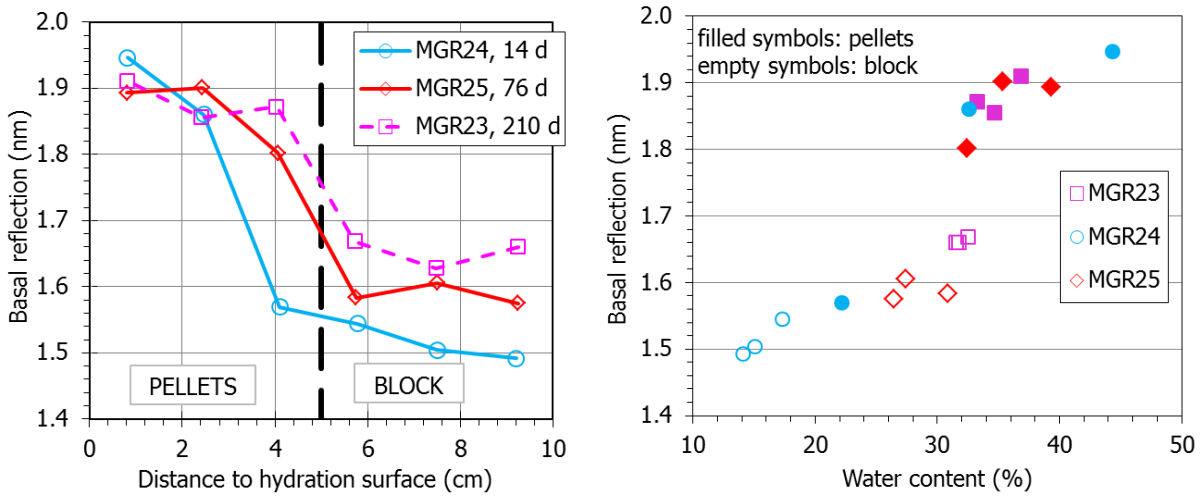

Figure 30. Main diffraction reflection of the basal reflection of subsamples of MGR tests. The duration of the tests is indicated in days

4.2 TRANSPARENT CELL (FEBEX)

4.2.1 HYDRATION PROCESS

Figure 31 shows the evolution of water intake as measured online for the two CW tests. The actual final water intake as determined by the difference between the final and initial weights of the bentonite is also included in the Figure. It is clear that the online water intake measurement was faulty and considerably overestimated the actual water intake. Nevertheless, the trend of the

curves is consistent and can give some indication about the kinetics of the hydration process. There was a significantly different behaviour between them. Although both were hydrated through the bottom under a very low hydration pressure, the bottom part of the cell was filled with pellets in CW1 and with a compacted block in CW2. In test CW1 there was a sharper initial entry of water until approximately day 92, while in test CW2 the entry of water occurred more gradually from the beginning. The final shape of the curves indicates that water intake was very close to stabilization, particularly for test CW1. The water intake measurement in test CW2 failed at day 316, but the total duration of the test was 420 days.

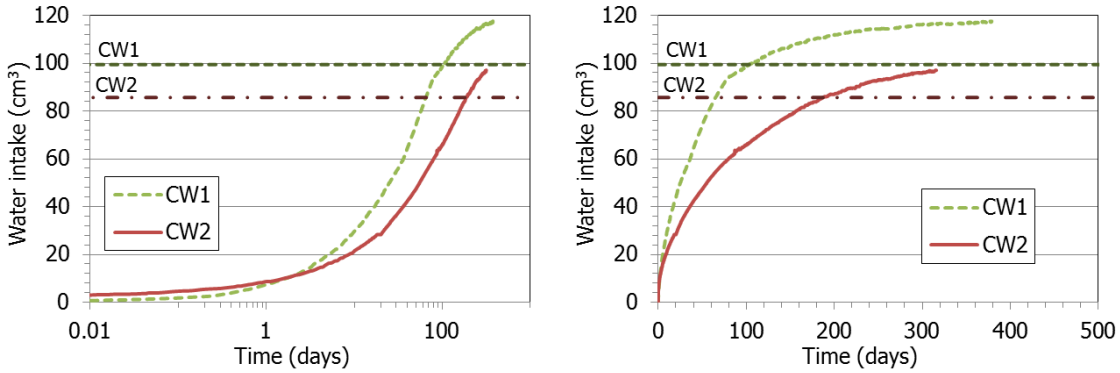

Figure 31. Evolution of water intake for tests CW1 and CW2. Test CW2 lasted 420 days, but water intake measurement failed in day 316. The dotted horizontal lines indicate the actual final water intake determined by weight difference

Cells CW1 and CW2 were periodically photographed on both sides (A and B faces) during hydration. Figure 32 shows a comparison of the appearance of face A of the two tests at the same testing times (Figures for face B can be found in the Annex). Variations in the coloration of the grains, changes in texture and shape, and displacement of the block-pellets interface were observed. As the pellets were hydrated, the grains increased in size, without displacement, and the whole of them lose sharpness. The appearance of the saturated pellets was gel-like. The evolution of hydration was slower in face B, where fine particles predominated. The reason could be the absence of large voids where water could quickly and easily penetrate. A downwards movement of the pellets/block interface in cell CW1 was observed, whereas this interface moved upwards in cell CW2.

The face-A images for the three first months of hydration in CW1 were analysed and the evolution of some distinct pellets and of the block/pellets interface were followed. In Figure 33 the interface between blocks and pellets in CW1 is shown in more detail along with the indication of the position of the interface and of the contour of some pellets at different stages. As the pellets were hydrated, the grains increased in size, without displacement, and they lose sharpness. The downwards movement of the pellets/block interface was also observed, which indicates the compression (or collapse) of the pellets part. The same images were also treated with the GIMP Image Manipulation Program by applying an edge detecter filter (Figure 34). The area of the pellets increased with no preferential direction, which indicates their swelling. Over time, the pellets/bentonite interface displaced downwards (as a result of the higher swelling capacity of the block) and became less distinct.

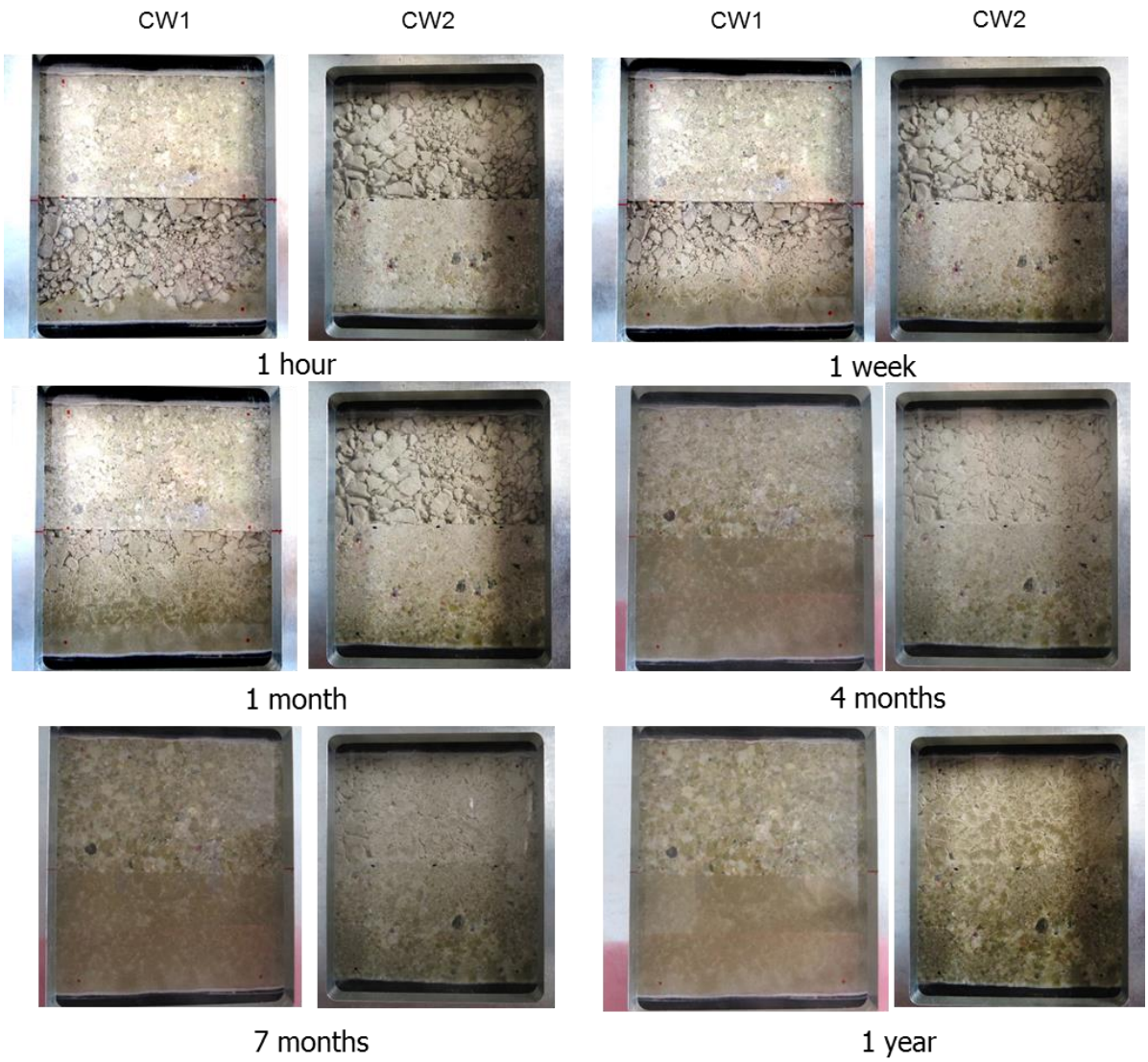

Figure 32. Comparison, in face A, of the evolution of the hydration in both cells (CW1: first and third column, and CW2: second and fourth column) for six different moments

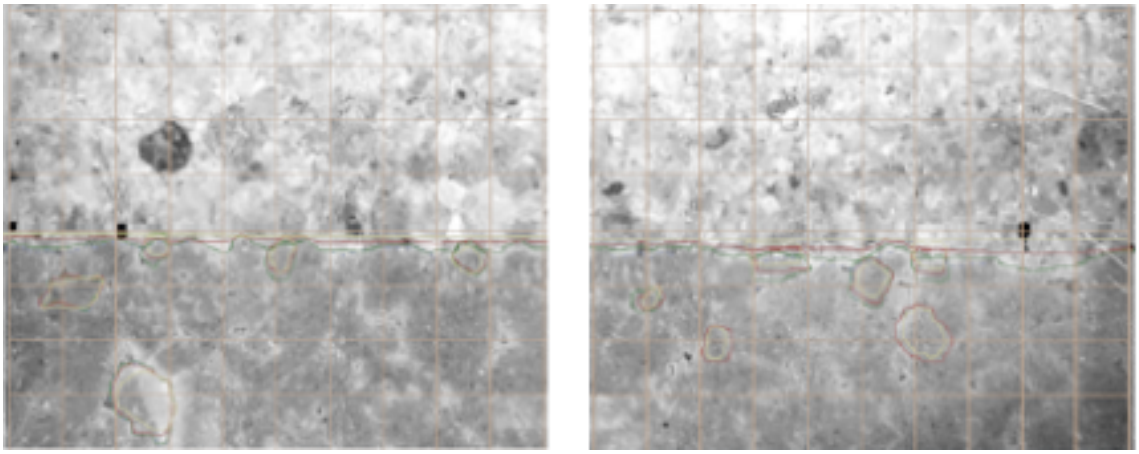

Figure 33. Detail of texture evolution of the interface since the beginning of the CW1 test (yellow), after a month (red), after two months (green) and after three months of hydration (blue). A 5x5 mm mesh has been represented

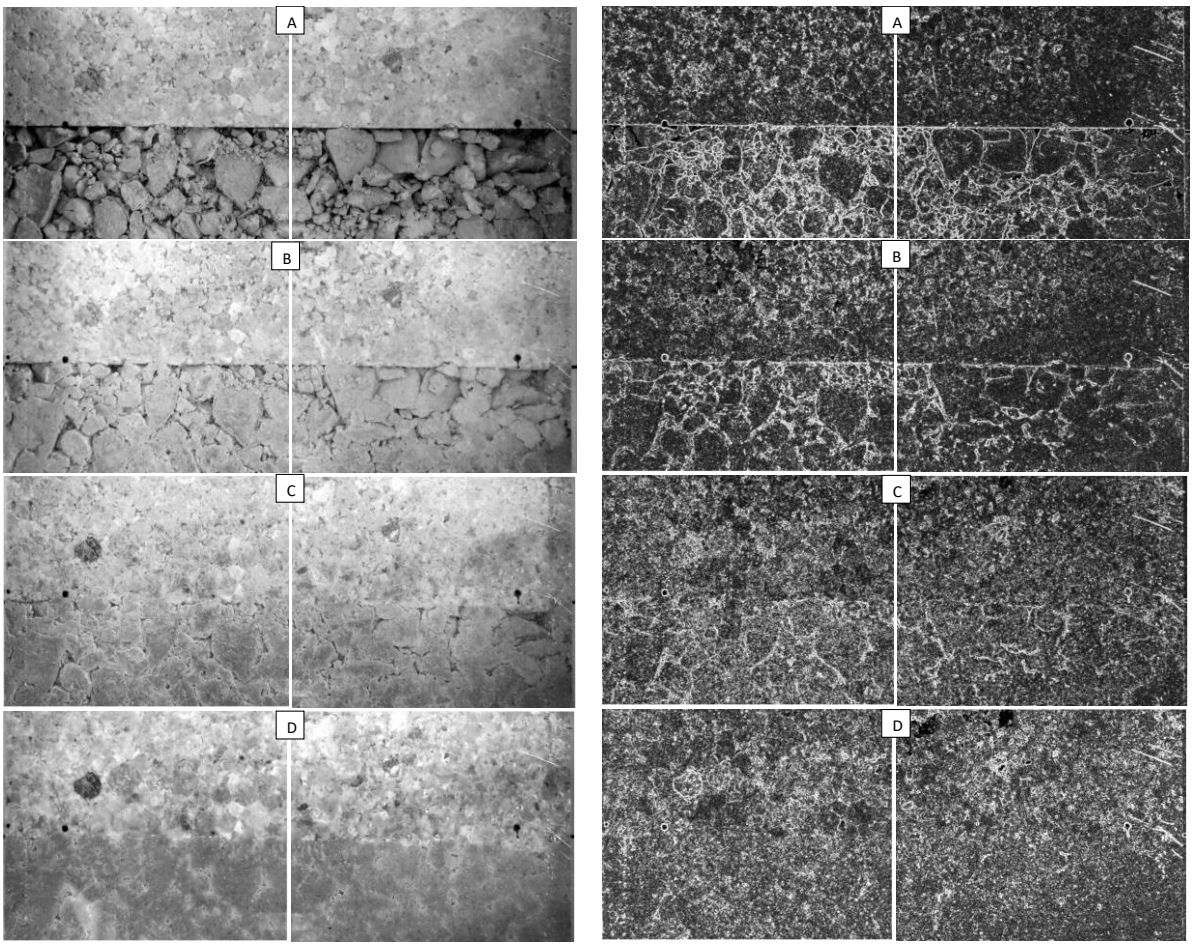

Figure 34. Appearance of the block/pellets interface in CW1 test at different stages of hydration in raw images (left) and images treated applying an edge detecter filter (right). (A: begnining, B: 1 month, C: 2 months, D: 3 months)

4.2.2 FINAL PHYSICAL STATE

Cell CW1, saturated through the pellets, was dismantled after 379 days and cell CW2, saturated through the block, after 420 days of hydration. A detailed characterisation of the final state of the bentonite was carried out in subsamples taken according to the schema shown in Figure 35. It was not possible to distinctly separate the block and pellet parts. Table 6 summarises the initial and final characteristics of the tests. For the global values, the initial and final dimensions and weight of the pellets/block assemblage were considered. Because bentonite swelling caused the compression of the geotextiles placed on top and bottom of the cell (Figure 5), the total height of the sample increased and hence there was an overall decrease in dry density. Cell CW1 had reached full saturation, but not cell CW2, despite its longer duration. The values shown in the Table for the block and pellets parts are the average of the determinations in subsamples. These may be affected by trimming and slight drying during manipulation.

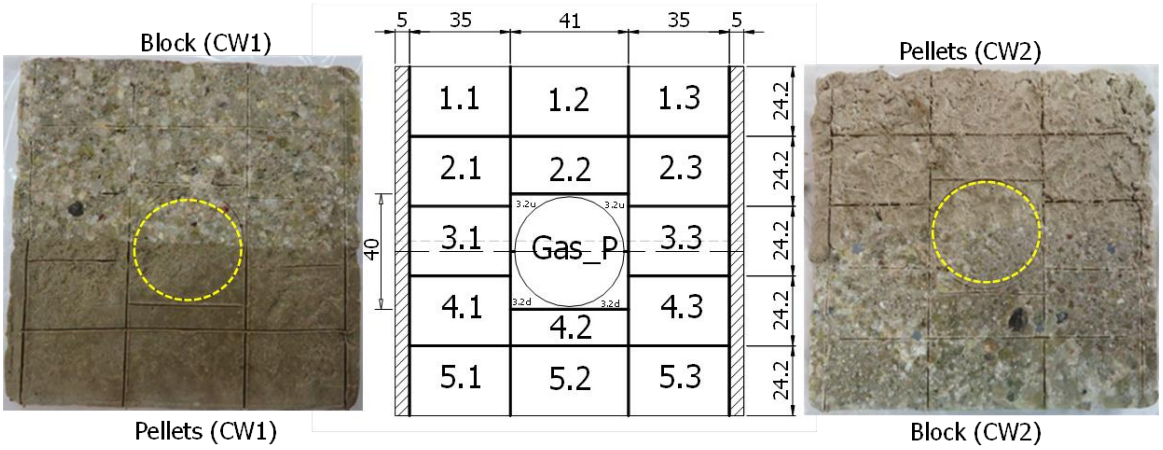

Figure 35. Final subsampling of tests CW and location of samples for gas permeability (circle)

	Initial				Final			
	h (cm)	w (%)	ρ_d (g/cm^3)	S_r (%)	h (cm)	w (%)	ρ_d (g/cm^3)	S_r (%)
Test: CW1								
Pellets[a]	5.75	10.1	1.30	25	5.69	40.5	1.28	99
Block[a]	6.03	14.0	1.59	54	6.37	32.8	1.47	105
Total[b]	11.79	11.9	1.45	37	12.06	35.9	1.38	102
Test: CW2								
Pellets[a]	5.60	10.1	1.30	25	5.58	32.4	1.31	82
Block[a]	5.98	12.4	1.61	50	6.64	32.1	1.45	101
Total[b]	11.58	11.2	1.46	36	12.22	32.1	1.39	92

[a] final dry density and degree of saturation affected by subsampling and trimming, [b] final values affected by compression of geotextile during test

Table 6. Initial and final characteristics of test CW1 and CW2

Figure 36 to Figure 38 show the final water content, dry density and degree of saturation determined in the subsamples of the two tests, along with the initial values. Hydration resulted in an overall water content increase both in the pellets and the block parts, considerably higher for the pellets part of test CW1. As a result of the water content increase, the bentonite swelled and the dry density of the assemblage decreased because of the slight deformation allowed by the geotextile compression (the overall dry density of cell CW decreased from 1.45 to 1.38 g/cm^3 and that of cell CW2 from 1.46 to 1.39 g/cm^3). In both tests the swelling was higher in the block part, whose dry density significantly decreased. Despite the fact that the sample CW1 was fully saturated at the end of the test (Table 6), there were still clear water content and dry density gradients, with higher water contents and lower dry densities in the pellets part, which was earlier saturated. In contrast, cell CW2, which was not completely saturated (S_r=92%), showed homogeneous water content, but still considerably higher dry densities and degrees of saturation in the block part. In fact, the average degree of saturation of the pellets part was only of 82%. The interface between pellets and block did not seem to play any role in the general trend of these variables.

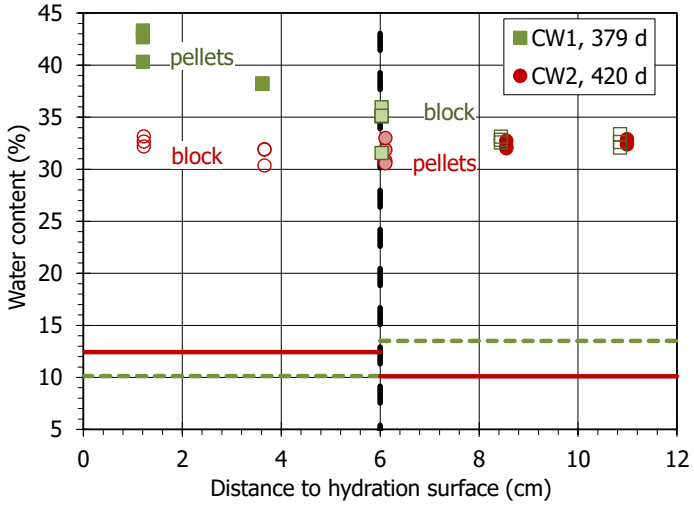

Figure 36. Final water content along the samples of CW tests. The duration of the tests is given in days. The thick horizontal lines mark the initial values

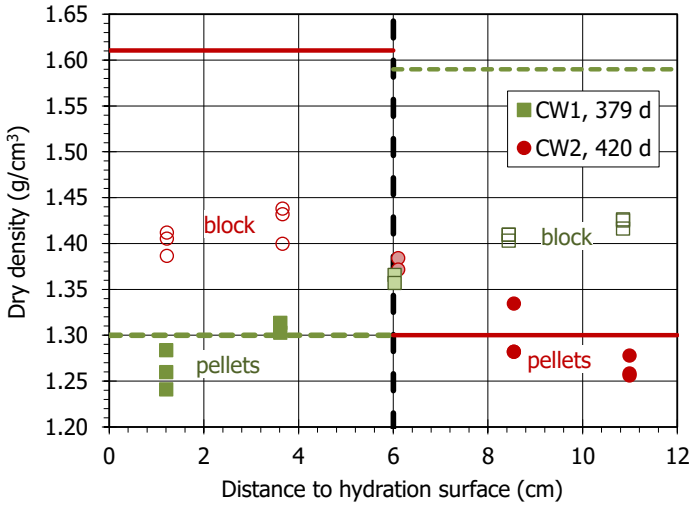

Figure 37. Dry density along the samples of CW tests. The duration of the tests is given in days. The thick horizontal lines mark the initial values

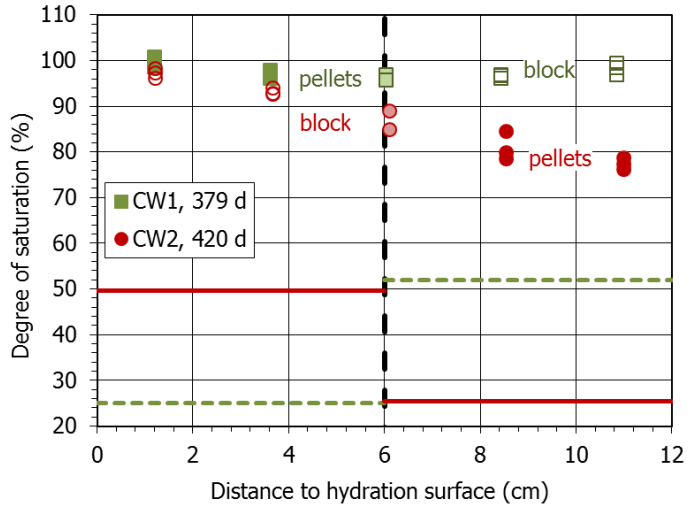

Figure 38. Degree of saturation along the samples of CW tests. The duration of the tests is given in days. The thick horizontal lines mark the initial values

A small border effect was observed at the bottom of the cell: the water content of the subsamples close to the border (5.1 and 5.3 in Figure 35) was slightly higher than that of the middle subsample (5.2), whereas the dry density was lower, especially in cell CW1. The cell border effect persisted, although weakened, until the upper part (e.g. samples 1.1 and 1.3 had slightly higher water content and lower dry density than sample 1.2).

The border effect can be better noticed in the 2-D plots for water content and dry density, which were obtained with the contour mapping software Surfer® using the Kriging gridding method (Figure 39 and Figure 40). The same colour code was used to draw the contour plots for each parameter. The concentric isolines around a particular sampling point are probably plotting artefacts caused by the small range of values. The final distribution of water content was very different in both samples. In the case of CW1, the highest water content occurred close to the hydration zone (pellets), whereas in CW2 the distribution was quite homogeneous all over the sample. In contrast, in both cases the dry density showed maxima in the area of the block, decreasing towards the opposite end. The loss of dry density in the CW2 block was greater than in the CW1 block, since it was precisely in that area where it began to hydrate, and therefore expanded.

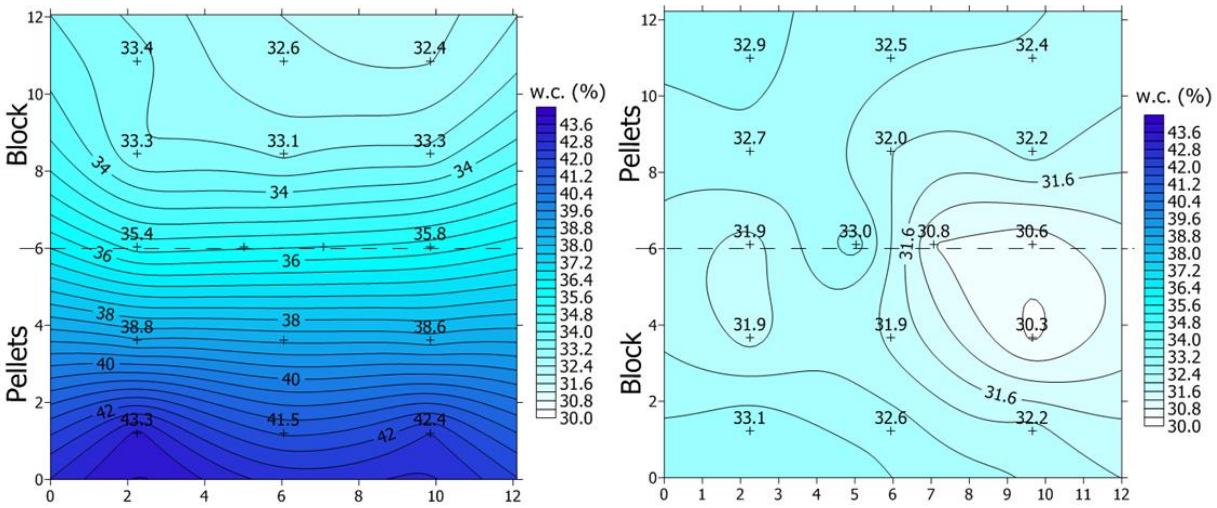

Figure 39. Contour plot for final water content in CW1 (left) and CW2 (right). Distances in cm

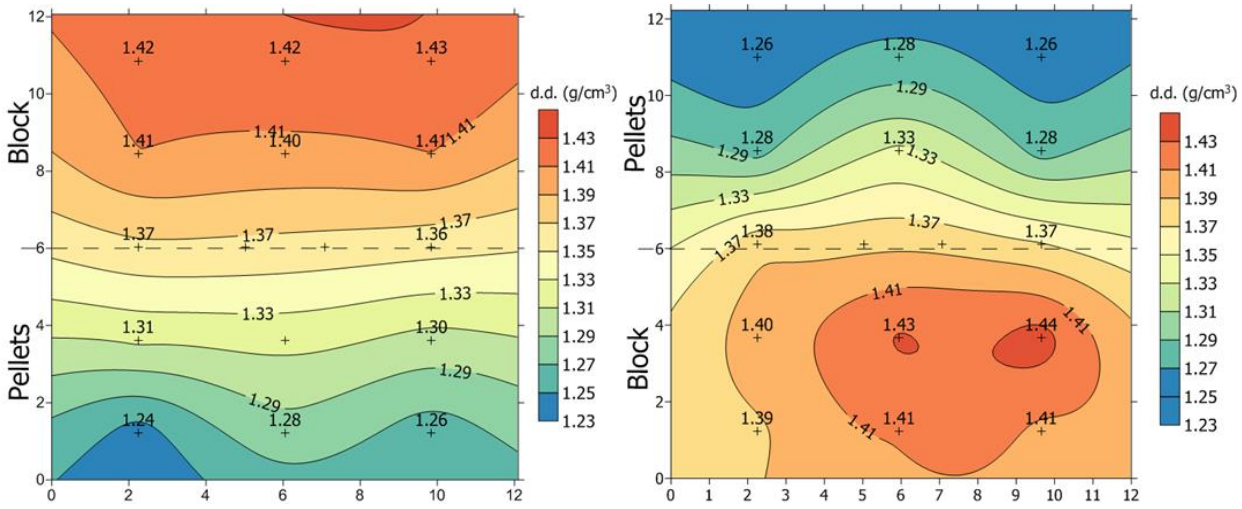

Figure 40. Contour plot for final dry density in CW1 (left) and CW2 (right). Distances in cm

4.2.3 MICROSTRUCTURAL CHANGES

Figure 41 shows the incremental curves of mercury intrusion as a function of the mean pore diameter of the diameter size intervals corresponding to each pressure increase step. In both tests the macroporosity of the pellets shifted to smaller pore sizes, more as the water content was higher. In particular, for the pellets part in test CW1 the mean size of the macropores considerably decreased, from ~300 µm to values between 6 and 40 µm. However, in some cases, pores larger than ~70 µm remained, particularly in CW2, where the pellets part was not completely saturated. The pore size distribution of the block parts did not change much as a result of hydration, particularly in test CW1. In the block part of test CW2 the size and volume of the macropores increased. All the samples had mean pore diameters for the pores smaller than 200 nm in a narrow range between 6 and 26 nm, and in test CW1 tended to decrease away from the hydration surface. In general the mean size of this pore family was higher than that for the initial block.

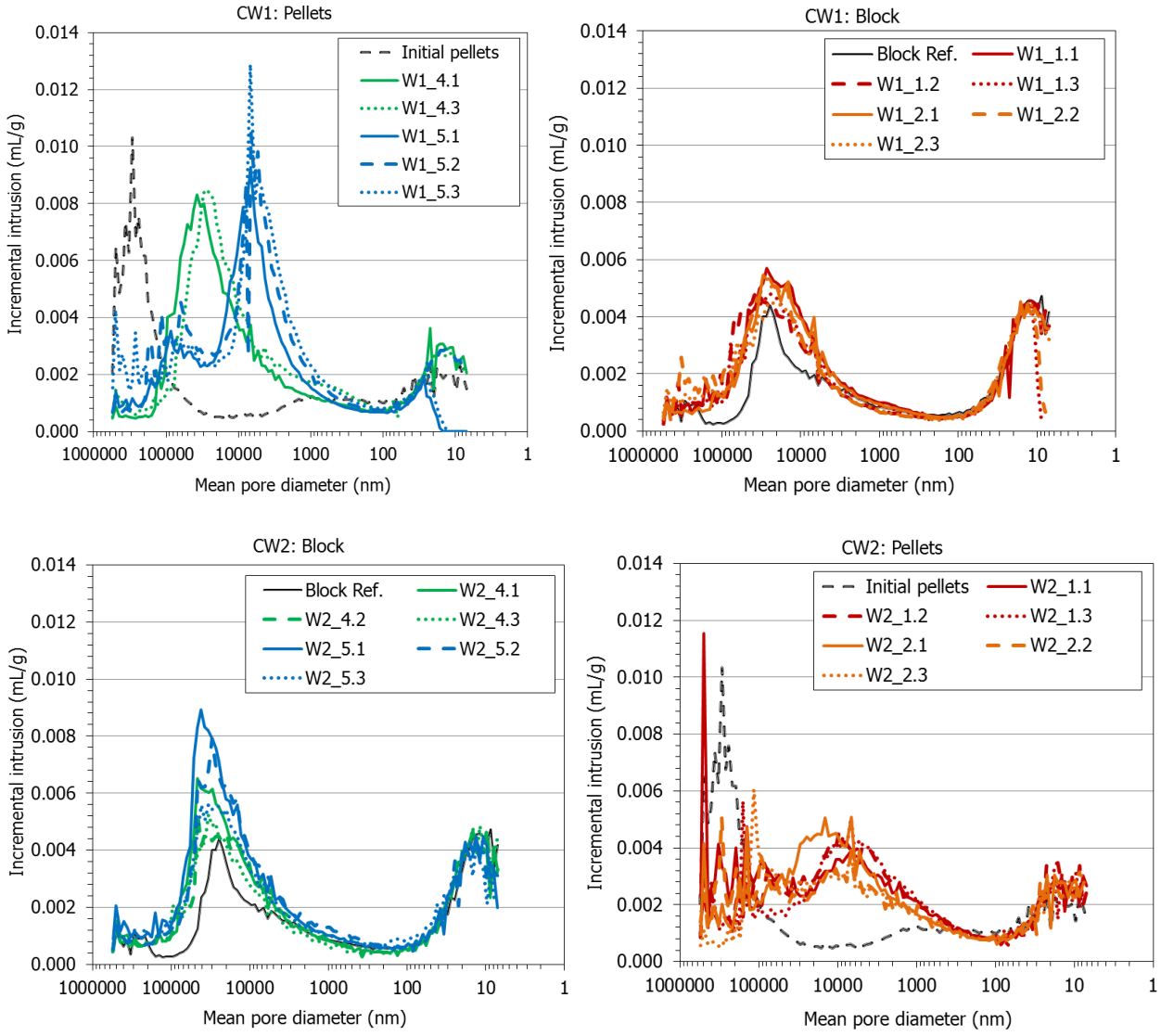

Figure 41. Incremental mercury intrusion in CW1 and CW2 (the curves corresponding to the initial conditions are also included)

The percentage of void ratio intruded, the void ratio corresponding to each pore size interval and the respective modes are shown in Tables in the Annex. As discussed above, and in view of the result in Figure 41, two major pore families could be identified, the separation between them being set to 200 nm. The void ratio corresponding to each pore size obtained by MIP for the different samples is shown in Figure 42 as a function of the distance to the hydration surface. In the block samples the largest proportion of void ratio corresponded to the pores of diameter smaller than 200 nm. As a result of saturation this percentage increased with respect to the reference block. The void ratio corresponding to pores <200 nm was similar in all the samples of CW1 whereas it decreased towards the hydration surface in CW2. Since, due to the compression of the geotextiles, the overall void ratio of the samples increased, the percentage of void ratio corresponding to pores larger than 200 nm also increased in all the block samples with respect to the reference values, but decreased in the saturated pellets of cell CW1.

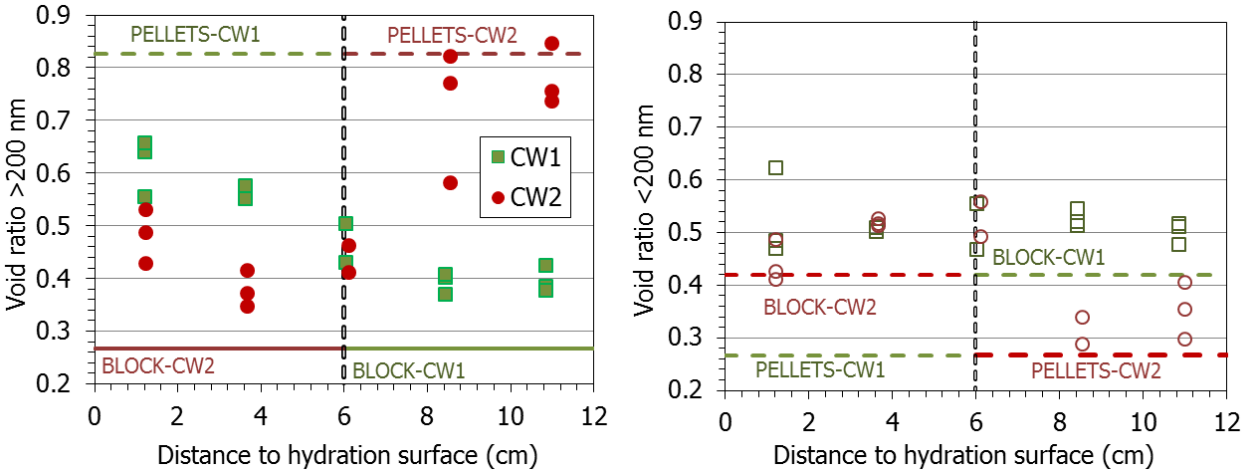

Figure 42. Void ratio corresponding to different pore sizes obtained by MIP in samples from tests CW (the thick horizontal lines indicate the distribution for the reference block and pellets)

The ratio e_m/e_M obtained by MIP for the different subsamples is shown in Figure 43 as a function of the distance to the hydration surface. For the pellets part in test CW1 the void ratio corresponding to pores larger than 200 nm considerably decreased, particularly away from the hydration surface (Figure 42). As a result, the e_m/e_M ratio increased in the same direction. In the pellets part of test CW2, the volume of large pores decreased only in some samples (except close to the pellets/block interface, where it significantly decreased), but the volume of pores smaller than 200 nm tended to increase, resulting in an increase of the e_m/e_M ratio in this area. In the block samples of both tests the largest proportion of void ratio corresponded to the pores of diameter smaller than 200 nm ($e_m/e_M>1$), but e_M increased with respect to the initial values, reflecting the overall decrease in dry density allowed by the compression of the geotextiles as a result of bentonite swelling (Table 6). Hence the e_m/e_M ratio was lower in the block parts, particularly for the samples closest to the hydration surface of test CW2.

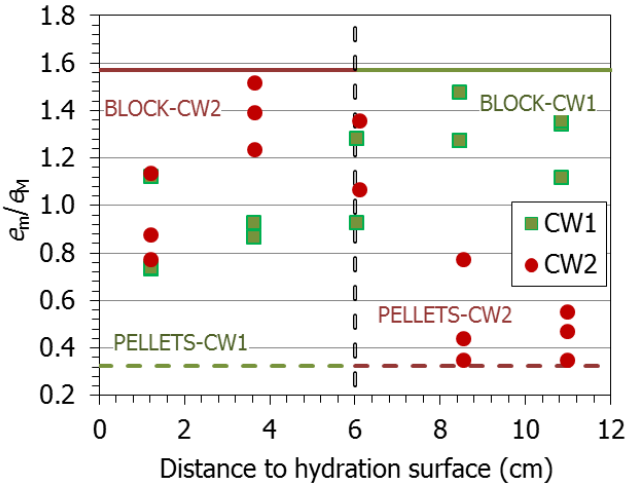

Figure 43. Void ratio corresponding to different pore sizes obtained by MIP in samples from tests CW (the thick horizontal lines indicate the distribution for the reference block and pellets)

The mode sizes of each pore family are plotted in Figure 44. All the samples had mean pore diameters for the pores smaller than 200 nm in a narrow range between 7 and 26 nm. Overall the size of this pore family was higher than for the initial block and lower than for the pellets, but in test CW1 tended to decrease away from the hydration surface. In contrast, the size of the macropores for the pellets part of CW1 was lower than the initial one.

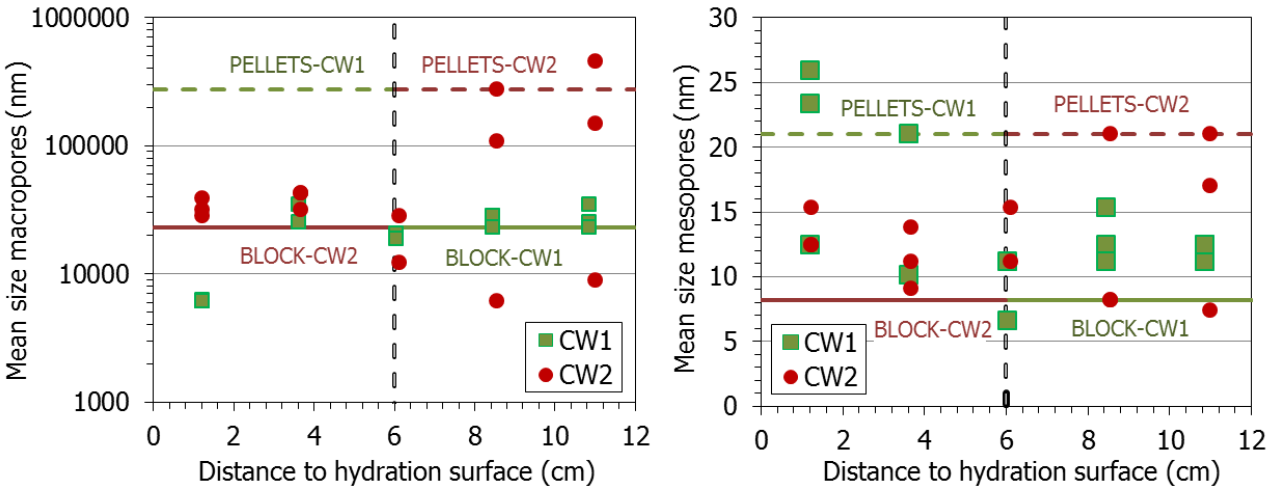

Figure 44. Void ratio corresponding to pores larger and smaller than 200 nm (left and right, respectively) as a function of the distance to the hydration surface

The BET specific surface area and the *t*-plot micropore volume calculated from the sorption isotherms are shown in Figure 45. A reduction in the BET surface in the area of the block, and an increase for the pellets, compared to those for the reference bentonite were observed. In the case of CW1, the increase in the BET specific surface area of the pellets was higher than in test CW2, where the pellets had lower water content. In fact, the usual increase of specific surface area with water content is evinced in Figure 46.

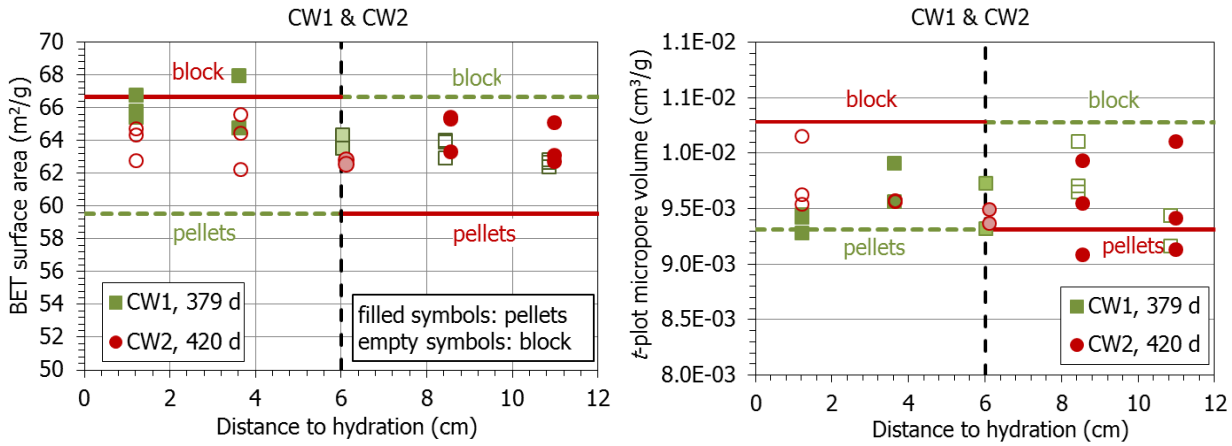

Figure 45. BET specific surface area and t-plot micropore volume of samples from tests CW and in the reference bentonite (thick horizontal lines)

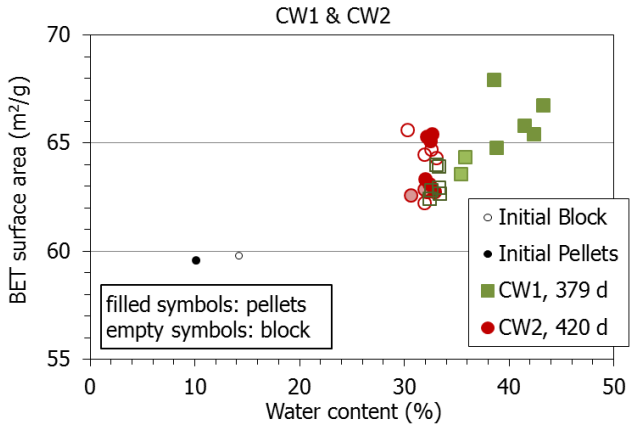

Figure 46. BET specific surface area of samples from tests CW as a function of their water content

The basal reflection was measured by XRD and the values obtained are plotted in Figure 47. The pellets samples of test CW1 had the highest basal spacings, ~1.9 nm, corresponding to the full development of the 3-layer hydrate. These samples had water contents higher than 38%. In contrast, the block subsamples of test CW2 had much lower basal spacings, increasing only slightly above the initial 1.5 nm value for the block with hygroscopic water content. These values were even lower than those measured in the block subsamples of test CW1. The relation of basal spacing to water content (Figure 47, right) shows that water contents lower than 32% corresponded to basal spacings lower than 1.55 nm, and above this water content the basal spacing increased sharply with it. It should be mentioned that the secondary reflection in the subsamples of test CW2 had values higher than 1.8 nm (and in some of them even higher than 1.9 nm), which indicates the transition from the 2- to the 3-layer hydration state. Also, the samples from test CW2 were X-rayed 15 days after they were obtained, which could have allowed certain water redistribution in the microstructure.

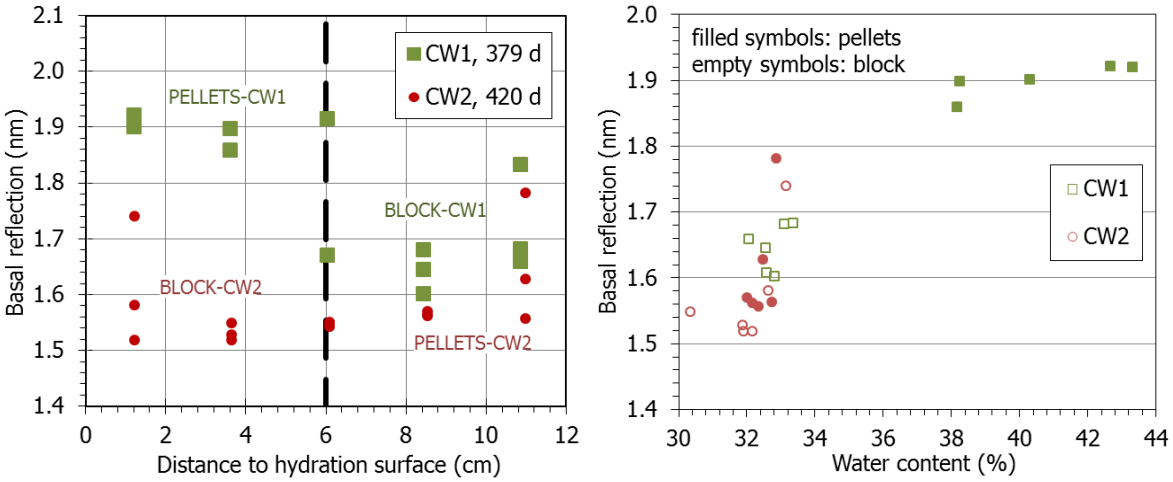

Figure 47. Main diffraction reflection of the basal reflection of subsamples of CW tests. The duration of the tests is indicated in days

4.2.4 HEALING OF BLOCK/PELLETS INTERFACE: GAS TESTING

At the end of the tests in transparent cell, a cylindrical subsample was obtained by drilling across the pellets/block interface to measure the gas breakthrough pressure as an indicator of the healing of the interface. These subsamples were vertically crossed by the interface (Figure 8, Figure 35) and had a nominal diameter of 3.8 cm. The initial and final characteristics of the samples as well as those of the tests are shown in Table 7.

Characteristics	CW1		CW2	
	Initial	Final	Initial	Final
ρ_d (g/cm^3)	1.33	1.43	1.36	1.40
h (cm)	2.16	2.13	2.15	2.15
ϕ (cm)	3.78	3.68	3.79	3.73
w (%)	34.8	32.2	30.3	29.3
S_r (%)	92	99	83	85
Confining *P* (MPa)	3.0		1.1-2.3	
Injection *P* (MPa)	0.2-2.9		0.2-0.3	
Duration (days)	32		4	

Table 7. Initial and final characteristics of the samples used for gas testing and characteristics of the tests

In test CW1-gas a confining pressure of 3 MPa was applied, corresponding to the swelling pressure of the bentonite with a dry density of 1.45 g/cm^3 (the global value for test CW1) according to Equation 3. This value was selected to keep approximately the same stress state as the bentonite likely had at the end of the test, when almost full saturation was reached, and prevent the interface from mechanically splitting. The injection pressure was increased by 0.1 MPa every two hours, from 0.2 to 2.95 MPa. The pressure and flow evolution during the gas testing are shown in Figure 48. There was no flow until the injection pressure reached 2.00 MPa. For injection pressures from 2.00 to 2.20 MPa there were barely measurable flow pulses. There was again no

flow from 2.20 to 2.85 MPa of injection pressure. For gas injection pressure of 2.90 MPa unsteady flow pulses close to the turndown value of the flowmeters were detected. At the end of the test the sample had consolidated as a result of the confining and gas pressure applied and its water content had slightly decreased, which would indicate that some water movement took place during the test.

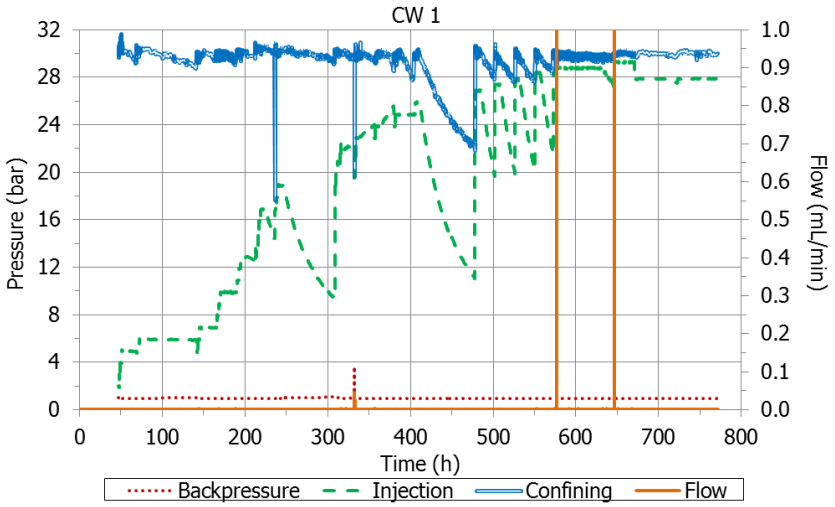

Figure 48. Confining pressure, gas pressure in the upstream cylinder, downstream pressure and outflow in test CW1

It can be considered that the gas breakthrough pressure was ~2.2 MPa, although no steady, correctly measurable flow was measured at any moment. This breakthrough pressure would be in the order of the values expected for FEBEX samples compacted to dry densities between 1.35 and 1.45 g/cm^3, which would be between 1.5 and 3.5 MPa (Gutiérrez-Rodrigo 2018, Gutiérrez-Rodrigo et al. 2021).

Because the sample from test CW2 was not saturated, the confining pressure applied during gas testing was initially lower, 1.1 MPa. In this case the outflow was high from the first step of injection pressure (0.2 MPa), and the confining pressure had to be increased to reduce it. Outflow continued until the confining pressure was 2.3 MPa, for which no flow occurred. Then the injection pressure was increased to 0.3 MPa, flow resumed and the test was dismantled. The permeability values obtained for each pressure step are shown in Figure 49. They are expressed as $k_{rg} \cdot k_{ig}$, where k_{rg} is the relative gas permeability and k_{ig} is the intrinsic permeability measured with gas flow. The duration of the steps had some influence on the values obtained, because the sample consolidated as a result of the confining pressure application, which resulted in a decrease of gas permeability. This would explain the significantly lower value obtained in the last step, which was obtained after the sample had been submitted to a confining pressure of 2.3 MPa for one day. Indeed the sample dry density increased during the test, even though the total duration of the test was of only 4 days. These permeability values are lower than those expected for the FEBEX bentonite compacted with similar accessible void ratio (0.165). In particular, the value obtained for a confining pressure of 0.1 MPa was $8 \cdot 10^{-17}$ m^2. According to the correlation presented in Villar et al. (2013), for a sample of FEBEX bentonite compacted at the same accessible void ratio, with no interface in it and tested under the same confining pressure, the intrinsic

permeability should be ~$2 \cdot 10^{-15}$ m^2, i.e. considerably higher. This would indicate that the pellets/block interface was not a preferential gas pathway and flow took place through the bentonite whole porosity. Hence, the interface was perfectly healed and sealed, even though full saturation had not been reached in this area.

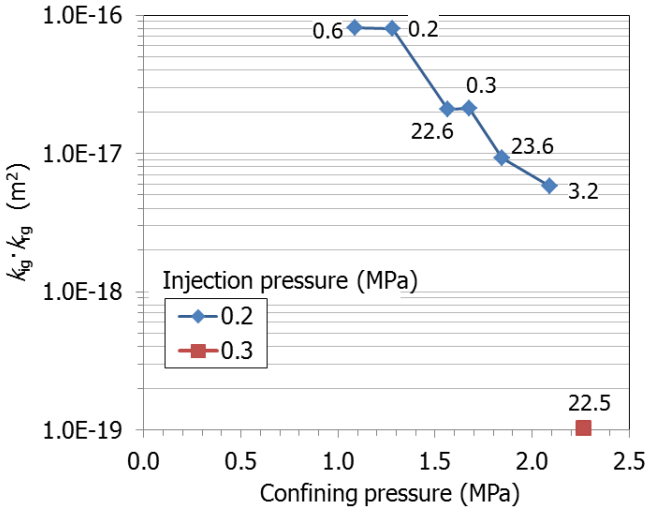

Figure 49. Gas permeability measured in a sample from test CW2 including the interface between block and pellets. The duration of some of the steps is indicated in hours

Figure 50 shows the pore size distribution of subsamples taken from the bentonite cores after the gas permeability tests along with the pore size distribution of samples taken at the same distance from the hydration surface as that of the samples used for gas testing (i.e. samples 3.1 and 3.3 in Figure 35). These curves were also shown in Figure 41. In all cases the subsamples used for MIP testing included the interface. In the sample from test CW1, the consolidation occurred during gas testing drastically reduced the volume of macropores. In contrast, in the sample from test CW2, which had been submitted to lower confining pressures and for shorter time during gas testing, the decrease in macroporosity was not so notable.

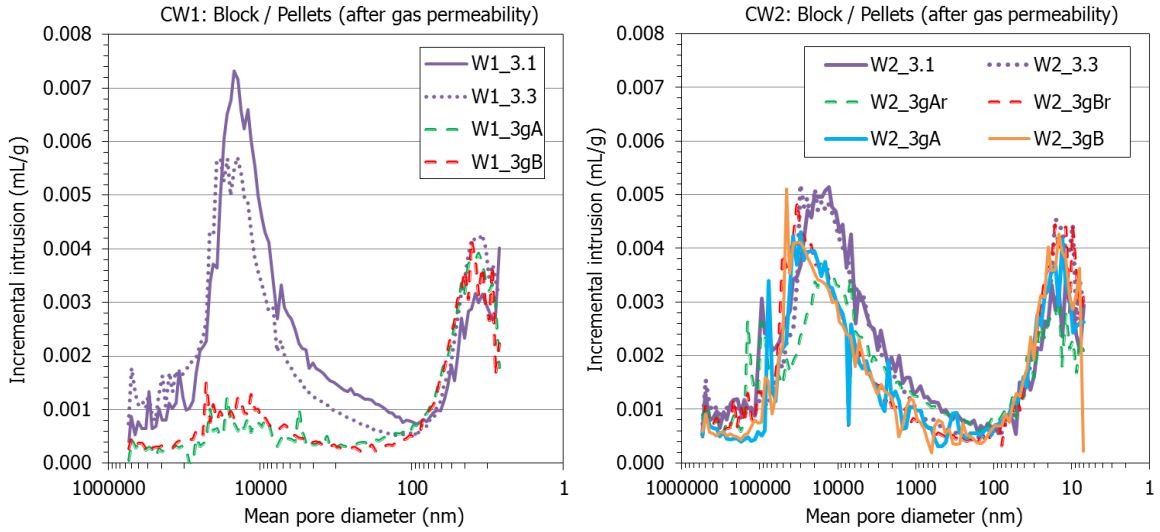

Figure 50. Pore size distribution obtained by MIP of samples of tests CW1 and CW2 before and after gas testing

4.3 INSTRUMENTED CELL (MX-80)

4.3.1 HYDRATION PROCESS

A binary sample composed of a mixture of high-density pellets and powder and a compacted block of MX-80 bentonite was hydrated in the instrumented cell described in 3.2, where the testing protocol was also described.

Deionised water was injected at a pressure of 14 kPa using a GDS volume/pressure controller (Figure 51). The water intake was faster at the beginning because of the volume of water necessary to saturate the porous stone and the high porosity of the pellets mixture. In the first two hours the water intake was so quick that the pressure could not reach the target value. It is considered that most of this water filled the hydration ducts inside the bottom lid and the lower porous stone. This value was in fact checked at the end of the test, when the cell was dismantled (see section 4.3.2), and has been subtracted from the initial water intake as shown in Figure 51. Considering this correction, and after approximately 600 days, the water intake stabilised at a value of ~893 cm^3. During this time gas bubbles were observed in the hydration line and had to be periodically vented.

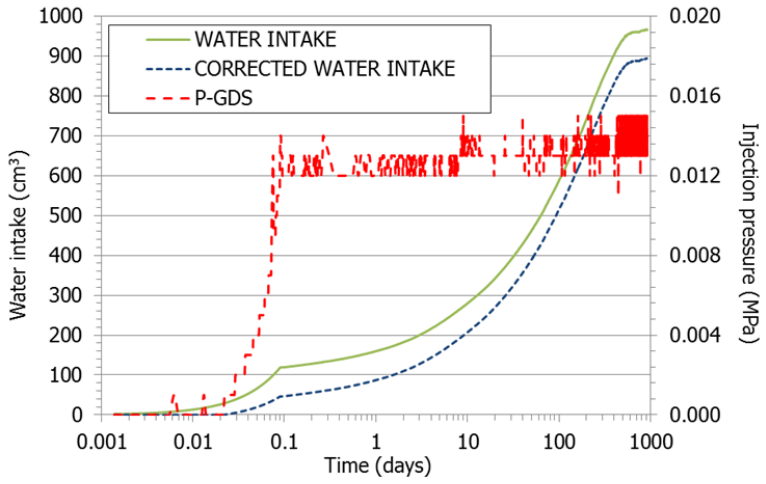

Figure 51. Water intake and injection pressure in test CT31

The RH/T sensor at the bottom was quickly flooded because of the high permeability of the low-density mixture (Figure 52). In an attempt to solve the premature loss of information from one of the sensors, it was removed from the cell and dried. Then the sensor was inserted again and its correct performance was checked. Nevertheless, the relative humidity at 13 mm from the hydration surface was 100% almost from the beginning of hydration. The sensors' recordings during the whole test duration are shown in Figure 53. After 2 years of hydration, consistent with the stabilisation of water intake, the RH at all positions inside the bentonite was around 100%.

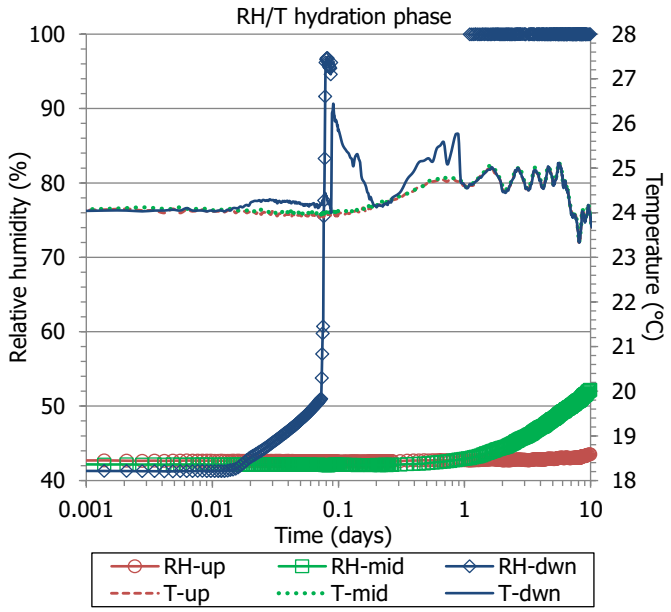

Figure 52. Relative humidity and temperature evolution at the beginning of hydration in test CT31

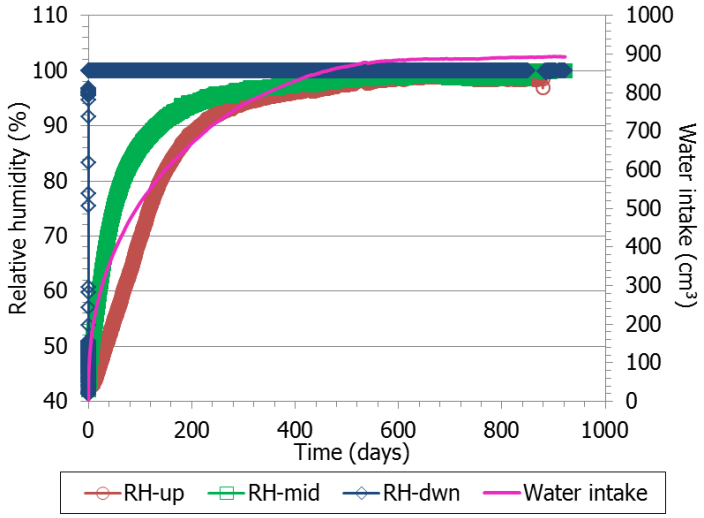

Figure 53. Relative humidity, temperature and water intake evolution during hydration in test CT31

The pressure sensors operated correctly since hydration started (Figure 54). The bottom sensor recorded a quick and steady pressure increase. The middle sensor recorded initially a soft decrease, probably reflecting the collapse of the pellets part on saturation. Afterwards the middle sensor recorded a considerable increase in a relatively short period of time (from 0 to 4.3 MPa in 60 days) followed by a soft decrease and a new constant increase. It took longer for the upper sensor to start recording any pressure (~200 days), but then it continuously increased. After ~700 days of hydration the three radial pressure sensors recorded steady values, with the middle sensor recording the highest one (6.4 MPa) and the bottom sensor the lowest one (4.6 MPa). This reflects the dry density gradient in the bentonite, where the lower part, which was first saturated, could swell more (see section 4.3.2).

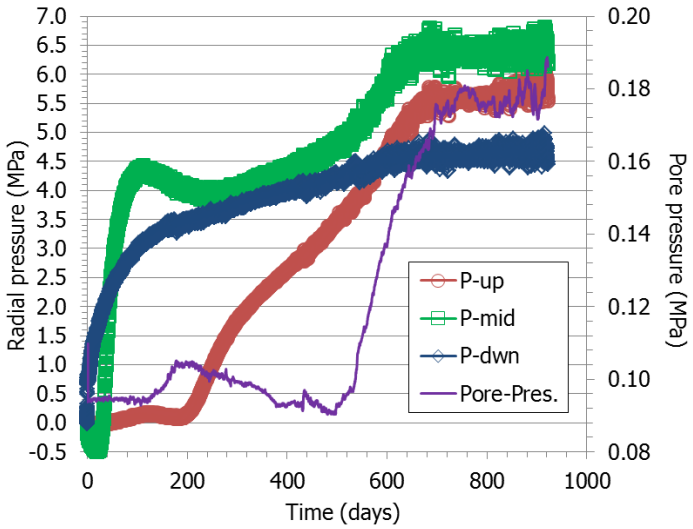

Figure 54. Lateral pressure and pore pressure evolution during the hydration phase of test CT31

As well, the pore pressure sensor on top of the cell did not record any change until 500 days had elapsed, and afterwards it steeply increased, reaching an equilibrium value of ~180 kPa.

A summary of the sensors' readings is given in the Annex.

4.3.2 DISMANTLING, SUBSAMPLING AND FINAL PHYSICAL STATE

The cell was dismantled after 922 of hydration. After stopping water injection, the sensors were removed and the bentonite was extracted from the cell pushing with a piston in a uniaxial press. No significant pressure had to be applied for the sample to come out. The bentonite block had a homogeneous appearance, it was dark and no pellets or other distinctive elements could be told apart (Figure 55). In fact, the separation between pellets and blocks was not clear, but it seemed to be at ~7 cm from the bottom surface. The porous stone through which hydration took place had numerous black spots irregularly distributed over the surface, possibly corresponding to areas of fungal growth. The final weight of the bentonite was 5020.31 g. According to the theoretical initial and dry weights of the sample (Table 4), this would correspond to a water content of 30.5% and a degree of saturation of 99%.

Figure 55. Final appearance of the bentonite block

The block was consistent and easy to handle and it could be easily sectioned using a saw. Saw cuts were made to obtain seven slices or horizontal sections (Figure 56), covering the compacted block area (sections 1B-3B), the pellets area (sections 5P-7P), and the contact area between both (section 4BP). Within each section, a series of samples were taken to analyse the state of the bentonite in the inner, outer and intermediate areas of the bentonite column.

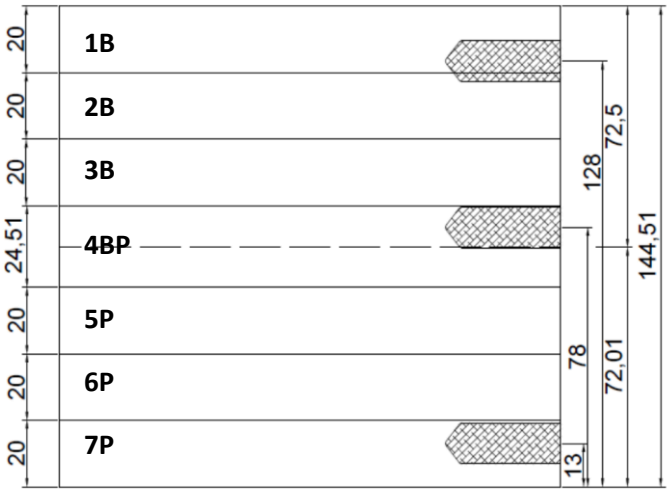

Figure 56. Subsampling of the bentonite block in horizontal slices (1B to 7P) and indication of the position of the RH/T sensors on the right (dimensions in millimetres, values according to initial measurements)

Figure 57 shows the water content and dry density values obtained along the bentonite block and Figure 58 the degree of saturation computed from them. The water content was higher in the 3 cm closest to the hydration surface, increasing towards it, but was homogeneous in the rest of the block, with values between 29 and 30%. The water content determined in the external ring of the block, i.e. in the bentonite in contact with the cell wall, was higher than the internal one both at the bottom and on top of the block. Conversely, the dry density on these areas was lower. In contrast, away from the bentonite column ends, the water content and dry density distributions at a given horizontal level were homogeneous. The degree of saturation tended to decrease from the hydration surface to the top of the block, but the values kept in a narrow range between 95 and 98%. The numerical values for these parameters in each subsample are given in the Annex.

According to these measurements the average water content of the block would be 30.0%, which is slightly lower than the value obtained from the final weight (30.5%). This is reasonable, since even careful handling of wet samples cannot avoid certain drying during manipulation. The final dry density obtained from the final block dimensions is the same as the average obtained from the different measurements.

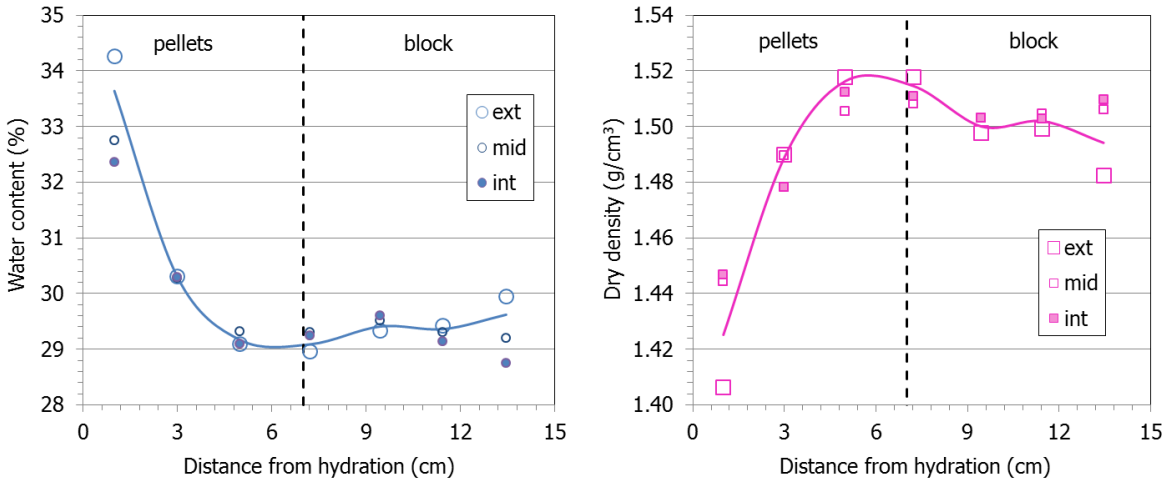

Figure 57. Water content and dry density measured across the sample (ext: average of 4 measurements at 6.1 cm from the axis, mid: average of 4 measurements at 3.4 cm from the axis, int: measurement at the axis)

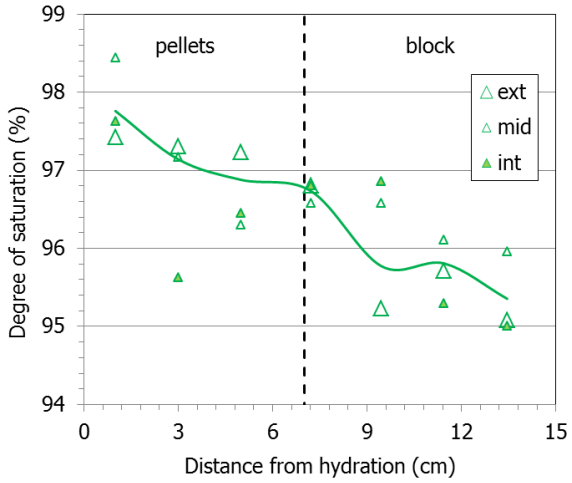

Figure 58. Degree of saturation measured across the sample (ext: average of 4 measurements at 6.1 cm from the axis, mid: average of 4 measurements at 3.4 cm from the axis, int: measurement at the axis)

4.3.3 MICROESTRUCTURAL CHANGES

The pore size distribution of some of the subsamples was determined by mercury intrusion porosimetry (MIP) following the methodology described in 3.1.3. Figure 59 shows the intrusion curves for MX-80 samples of the same characteristics (reference curves) as the initial conditions used in the cells (block and pellets/powder mixture). For the block part, the curve corresponding to a sample compacted at dry density 1.5 g/cm^3 with a water content of 9% was used as representative of the initial state. For the GBM, a mixture of pellets/powder with a ratio 70/30 was prepared in the sample holder and slightly pressed. Although the density reached was much lower than the actual dry density of the mixture in the test (0.75 vs. 1.5 g/cm^3) the curve obtained probably displays the main features of the GBM pore size distribution. The Figure also shows the pore size distribution corresponding to single pellets with no powder addition. Obviously, the porosity of the high-density pellets was much lower, with barely no porosity corresponding to pores of size larger than 100 nm. The distribution for pore sizes below ~10 µm was similar for the

pellets and for the GBM, but for larger pores there was a huge difference, since the individual pellets do not have large pores. The curve obtained for the GBM showed a predominant pore size around 150 µm (likely smaller for the actual GBM initial dry density).

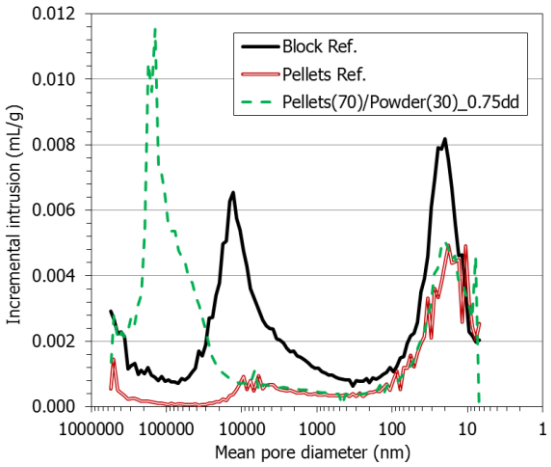

Figure 59. Pore size distribution expressed as incremental mercury intrusion of initial materials used in test CT31

Figure 60 shows the incremental curves of mercury intrusion for the subsamples of test CT31 as a function of the mean pore diameter of the diameter size intervals corresponding to each pressure increase step. The figure also includes the curves corresponding to the reference initial materials. Two major pore families could be identified, the separation between them being set at 200 nm, approximately separating macro and mesopores. As a result of hydration the macroporosity of the block samples shifted to larger pore sizes but lower volumes, whereas the void ratio corresponding to pores smaller than 200 nm increased. The volume of macropores in the pellets decreased with respect to the initial material and away from the hydration surface. For all the samples the mesopore mode size kept in values of 19±2 nm. Overall, no significant differences between the block and the pellets parts could be observed, except that in the pellets part the void ratio corresponding to macropores was larger than in the block part, likely owing to the lower dry density of the pellets (Figure 57).

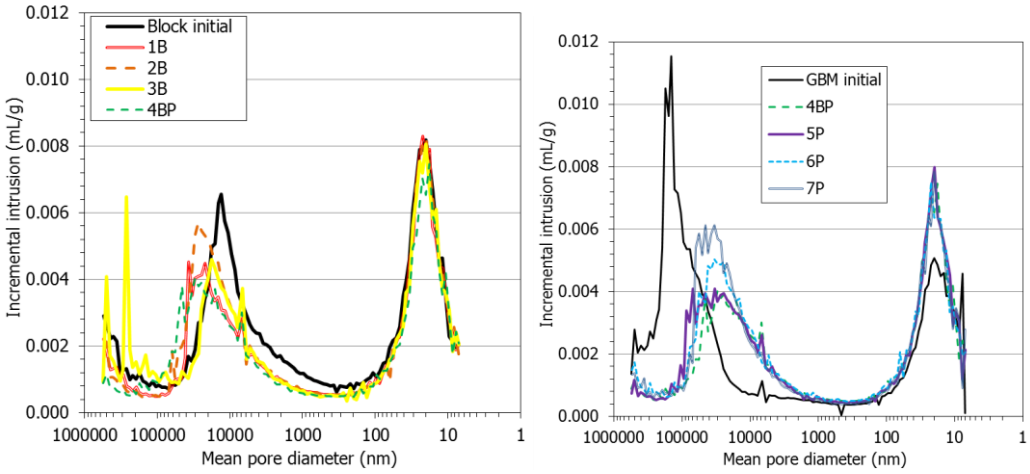

Figure 60. Incremental mercury intrusion in subsamples from test CT31 and of the initial materials (see Figure 56 for the location of samples)

The BET specific surface area of the samples was between 32 and 35 m^2/g, but these small variations were not related to the kind of sample or to their water content. As well, the basal reflection values were all in a narrow range between 1.58 and 1.52 nm, corresponding to the two-layer hydration state. Overall they were higher for the pellets samples, but in both parts, pellets and block, they were higher towards the hydration surface. The basal spacings were in fact directly related to the water content.

The detailed results of the MIP, sorption isotherms and basal spacing measurements are shown in the Annex.

5 DISCUSSION

The tests presented allowed to follow the hydro-mechanical evolution of a two-component buffer material upon hydration under isochoric conditions at ambient temperature. The dimensions of the testing cells were between 10 and 15 cm in height. In the case of the tests with FEBEX bentonite, the two components (bentonite pellets –GBM– and bentonite block) had different initial water contents and dry densities. In the only test with MX-80 bentonite, CT31, the initial dry density of the two components was the same and the water contents were not too different. Except in tests MGR27 and CW2, hydration took place through the pellets part, which in the case of the FEBEX tests, had a higher intrinsic permeability than the block because of its lower dry density, higher macroporosity and lower water content (Villar and Lloret 2001, Romero 2013). During the MGR tests the axial pressure was measured on the sample surface opposite to hydration, whereas in test CT31 the radial pressure was measured at different levels. The discussion below is mainly based on the results obtained with the FEBEX bentonite and mostly taken from Villar et al. (2021a).

The pressure development was not mainly related to the quantity of water taken (i.e. to the overall degree of saturation), but to the water intake rate. Thus, when hydration took place under very low water inflow rate (MGR22, MGR26), the axial pressure for a given overall degree of saturation was much higher than for the tests in which hydration took place more quickly (Figure 12, right). Similarly, in test MGR27, in which hydration under constant injection pressure was slower because it took place through the higher-density block part, the pressure reached for a given overall degree of saturation was initially (namely until the overall degree of saturation reached ~60%) higher than for the tests in which saturation took place through the pellets. This suggests that it was the redistribution of water in the microstructure the mechanism that triggered most of the swelling. This is supported by the fact that in test MGR23 the axial pressure considerably increased during the 14-day period during which inadvertently no water was supplied to the cell, showing that water redistribution inside the bentonite can cause pressure increase. In the EB in situ test performed at the Mont Terri URL, where a large-scale two-component barrier (FEBEX GBM and blocks) was tested for 10.5 years, most of the sensors installed in the bentonite recorded relative humidity values of 100% only one year after the beginning of the test, whereas it took four years for the total pressure sensors to record stable values that kept approximately constant until the end of the test (García-Siñeriz et al. 2015).

In the test performed with MX-80 (CT31), the comparison of Figure 53 and Figure 54 shows that, except for the sensor closest to the hydration surface, which became quickly flooded, the middle and top pressure sensors recorded the largest pressure increases when the overall degree of saturation was higher than 90% (after ~400 days of hydration). In particular the middle sensor, located in the block part at 8 cm from the hydration surface, recorded an increase in pressure from 4 to 7 MPa for a relative humidity increase of only 4 % (from 96 to 100%). This can be better observed in Figure 61.

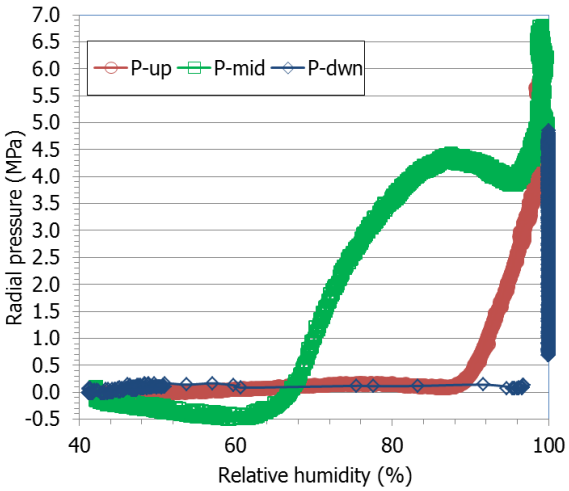

Figure 61. Radial pressure measured at different heights in test CT31 against the relative humidity in the same locations (MX-80 bentonite, see Figure 10 for location of sensors)

The different strength of the materials involved also played a role on the axial pressure development kinetics at the first stages of saturation. When the water intake was very slow, the block part was able to swell relatively quickly (see the dry density and water content distribution at the end of test MGR26 in Figure 19 and Figure 20), and because the pellet part was comparatively dry (drier than at the end of any other test) and consequently rigid, the stress was more effectively transmitted towards the top and hence recorded by the load cell. In contrast, when hydration was quicker, the pellet part soon collapsed and was easily compressed by the downwards swelling of the block, resulting in a lower axial load measured on top. In fact, a downwards movement of the pellets/block interface in cell CW1 was observed, indicating the compression (or collapse) of the pellets part. In contrast, this interface moved upwards in cell CW2, saturated through the block.

The final axial pressure measured in the MGR tests is plotted against the final degree of saturation in Figure 62. Overall the pressure consistently increased with the average degree of saturation, but in test MGR26, saturated under low water inflow, a pressure higher than expected according to the trend marked by the other tests was reached, consistent with the description of the initial stages of saturation given in the previous paragraph. Once full saturation was reached, the swelling pressure was the same irrespective of the way of saturation, and thus tests MGR22 and MGR23 showed the same final pressure (3 MPa). This value is higher than the swelling pressure expected for a FEBEX bentonite sample compacted to the average dry density value of the MGR tests (1.45 g/cm^3). The theoretical value would be 2.0±0.5 MPa, according to the empirical correlation between dry density and swelling pressure obtained in small standard oedometers (Eq. 3). Previous researches suggested that there is a scale effect on the swelling pressure measured in the laboratory, which tends to be higher as the testing cell is larger (Imbert & Villar 2006).

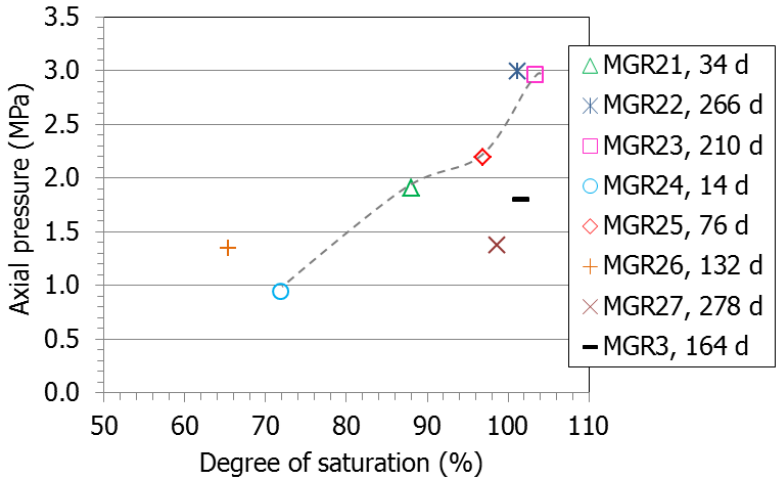

Figure 62. Final axial pressures measured as a function of the final degree of saturation of MGR tests (average ρ_d=1.45 g/cm^3)

Even though full saturation had not been reached in test MGR27 (final S_r=99%), the final pressure measured in this test was much lower than could be expected according to the general trend for tests in which saturation took place through the pellets shown in Figure 62. Hydration tests performed in large-scale cells where radial and axial pressures were measured at different heights along the sample length showed that during saturation, the transient pressure values were related to the local dry density (Dueck et al. 2016, Baryla et al. 2019, Bian et al. 2019, Bernachy-Barbe et al. 2020, Harrington et al. 2020). This was also the case in test CT31 with MX-80 bentonite (section 4.3), where the final equilibrium pressures measured at three different levels were exponentially related to the final dry densities measured in the area where the sensor was located (Figure 63).

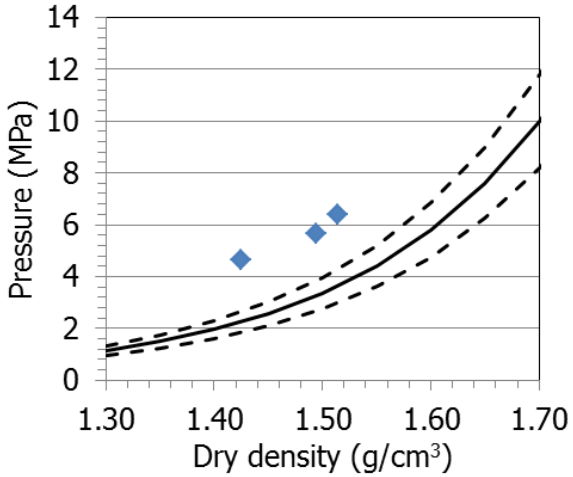

Figure 63. Axial swelling pressure of MX-80 compacted to different dry densities (Eq. 4) and equilibrium radial pressures measured in test CT31 as a function of the final dry density measured at the sensors' locations

In the case of test MGR27, the pellets part, on top of the sample, had the final lowest dry density (Figure 20) and lower degree of saturation (Figure 21). It is likely that the axial load measured reflected mainly the local pressure at the upper part of the sample, which would be lower than the pressure that would have been measured at the bottom (in the block part) if there had been a

pressure sensor in the area. In other words, the axial pressure measured on top would not be fully representative of the average pressure developed by the sample, because it would also be affected by the local conditions on top of the sample (lower density and degree of saturation). Similarly, the axial top pressure measured in the rest of the tests would also be conditioned by the higher dry densities in this area, where the block was placed (Figure 20). Also in test CT31, which seems to be fully saturated, the axial pressure measured on top was higher than that measured at the bottom, where the pellets were placed (Figure 54). Hence, in addition to the scale effect commented in the previous paragraph, a further reason for the higher than expected pressures observed would be the influence of the higher density close to the measuring area on top.

As a further corroboration of that hypothesis, the final swelling pressure reached in a test performed in the same oedometer with a mixture of regular-shaped FEBEX bentonite pellets and powder in a 70/30 ratio has also been included in the Figure (test MGR3). The average dry density of this mixture was 1.45 g/cm^3 (as in the MGR tests presented here) and the initial water content 13.6% (Villar 1999). In this case the swelling pressure of the saturated sample had an intermediate value between the trend for tests having the pellets on top (MGR22 and MGR23) and the test with the block on top (MGR27). This would reflect the intermediate value of dry density on the top part of the sample, which was 1.43 g/cm^3 at the end of test MGR3, 1.46 g/cm^3 at the end of tests MGR22 and MGR23 and 1.42 g/cm^3 at the end of test MGR27, which in addition was less saturated.

The tests performed by Martikainen et al. 2018 (reported in Talandier, 2019) were very similar in design and dimensions to the tests presented here, with hydration under an injection pressure of 10 kPa taking place through the pellets (hence comparable to tests MGR21, MGR23 to MGR25 and CT31). Hydration took place through the top surface, where the pellets were placed. In these tests MX-80 bentonite was used and the radial pressure developed by the block and the pellets parts were measured in addition to the axial ones. The axial and radial pressure development in the areas farther away from hydration (i.e. around the block part) displayed the initial peak followed by a decrease and a smooth eventual increase observed in some MGR tests (Figure 12) and in the middle part of test CT31 (Figure 54). These measurements also showed significantly lower pressures in the pellets than in the block part. The modelling groups involved in a benchmark where these tests were analysed, concluded that this difference was due to the initial contrast of density between the top and bottom of the sample but also to the friction between the bentonite and the steel cell wall (Talandier, 2019).

Indeed none of the finished tests reached a final complete homogeneity in terms of dry density or water content: the water content decreased from the hydration surface upwards whereas the dry density increased (Figure 19 and Figure 20). These heterogeneities resulted from the initial swelling and ensuing density decrease of the bentonite that became first saturated (those parts closest to the bottom hydration surface), and the consequent compression of the bentonite located upwards. In contrast, a final homogeneous degree of saturation close to 100% was reached in the longer tests saturated through the pellets, i.e. MGR22, MGR23 and CW1 (Figure 64). Once overall full saturation was reached, no further water content or dry density changes are

to be expected, which would mean that part of the initial volume changes were irreversible. Also in the large-scale EB test mentioned above, no spatial trends were found for the degree of saturation, despite the fact that density and water content gradients remained (García-Siñeriz et al. 2015). In all cases the pellets/block interface did not seem to have any effect on the continuous gradients observed, i.e. there were no sudden changes across the interface. In test CT31, in which the initial dry density of the block and the pellets part were similar, the bentonite at less than 3 cm from the hydration surface (pellets) presented significantly higher water contents and dry densities, even though hydro-mechanical equilibrium had been reached. This would indicate that the source of final heterogeneity was not the initial state, but the hydration process itself.

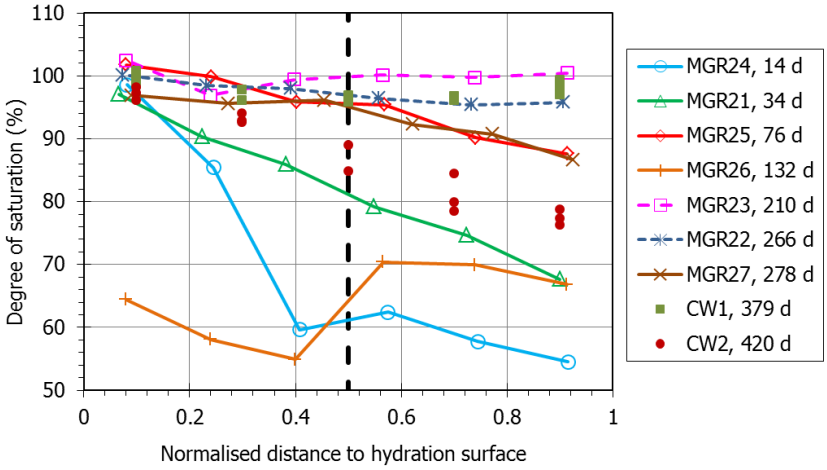

Figure 64. Final degree of saturation along the samples of MGR and CW tests (total length of 10 cm in tests MGR and 12 cm in CW). Hydration took place through the pellets except in tests MGR27 and CW2. The duration of the tests is indicated in days

The two tests in which hydration took place through the block (MGR27 and CW2) were far from full saturation, despite the fact that they were the longest ones performed in each kind of cell. It is remarkable that in all the tests the area closest to the hydration surface was fully saturated, except in test MGR26. This test, performed under constant flow and lasting 132 days, did not follow the overall trend, since the increase in water content was moderate and similar for both halves, attesting the more homogeneous water redistribution allowed by slow hydration. Vapour diffusion in the pore spaces would be the water transfer mechanism away from the hydration surface, as postulated by Kröhn (2005), who described the time-dependent water content distribution during the saturation of compacted bentonite under laboratory conditions by Fick's second law. Eventually, when full saturation was reached, the differences in the physical state of samples saturated under constant pressure or flow obliterated, resulting in the similar water content and dry density distribution patterns of tests MGR22 and MGR23.

Concerning the microstructural modifications during hydration, the GBM and the block parts behaved quite differently and in fact most parameters inferred by MIP (volume and size of each pore range, ratio between them), were different for the two components of the samples. Unlike the physical variables discussed in the previous paragraphs, in most tests there was not a smooth change between the microstructural parameters of pellets and block. The most notable change in

the pellets parts was the disappearance of the pores larger than 550 µm and the overall drastic decrease in size and volume of macropores. In contrast, the mean size of the pores smaller than 200 nm increased with respect to the original values for all the pellets subsamples (Figure 25). This was also the case for the block samples (not in the case of test CT31). Furthermore, in the block subsamples the volume and size of the macropores tended to increase, except in the shorter, less saturated tests. The increase of both e_m and e_M in the block subsamples of the MGR tests resulted from the overall decrease in dry density experienced by the block upon hydration. As a result, the e_m/e_M ratio increased only slightly in the shorter tests but remained in values similar or slightly below the initial one (1.57) in the longer tests (Figure 26). Figure 65 shows this ratio for the more saturated tests performed with FEBEX bentonite as a function of the water content of the subsamples. The results obtained in samples from the EB in situ experiment have also been included (these results have been reworked from those in Villar et al. 2014). Overall the e_m/e_M ratio tended to decrease with the water content increase, both in the laboratory and the in-situ samples. Maybe for this reason in the lab tests the block samples had higher ratios than the pellets samples (as was the case in the initial materials), since their water content was generally lower. In contrast, in the in situ test (lasting 10.5 years) the e_m/e_M ratio seems to be independent of the kind of sample, since the range of water contents of GBM and block samples analysed were similar. In all the pellets samples the e_m/e_M ratio increased significantly with respect to the initial value (0.31). Only the driest pellets samples (corresponding to the shorter tests, test MGR26 performed under constant flow, and test CW2 saturated through the block) had e_m/e_M ratios close to the initial one. These samples kept also pores larger than 550 µm that cannot be detected by MIP (because of the technique limitations) but were inferred as explained at the beginning of section 4.1.3.1. Pores larger than ~70 µm were actually observed by MIP in some pellets samples of test CW2 (Figure 41), where the pellets part was not completely saturated.

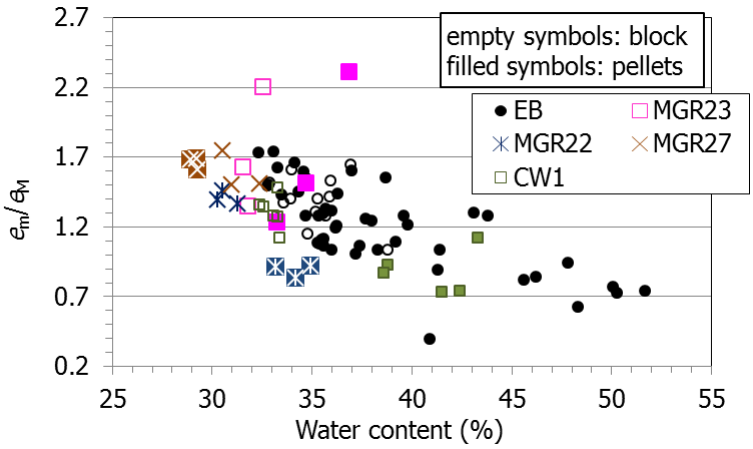

Figure 65. Ratio between void ratio corresponding to pores smaller and larger than 200 nm (em and eM) obtained by MIP in subsamples from the more saturated MGR and CW tests

The only FEBEX test with quite homogeneous values of e_m, e_M and mean pore sizes across the pellets/block interface was test MGR27, which was also the test reaching a highest homogeneity concerning dry density and water content. Also, the subsamples from test CT31 –which also had similar water contents and dry densities in the block and pellets parts– were also quite

homogeneous in terms of pore size distribution. This suggests that the microstructural changes were related to the changes in dry density and water content and thus to temporal evolution.

Hence, as a result of hydration the volume of micropores increased in all the bentonite with respect to the initial one, particularly in the case of the pellets. The increase in the volume of micropores was likely related to the increase in the smectite basal spacing as a result of the hydration of the interlayer cations (Figure 30 and Figure 47), which is the driving mechanism for crystalline swelling, predominant in compacted bentonite saturated under isochoric conditions (e.g. Pusch et al. 1990, Devineau et al. 2006). As it happened with the pore size distribution obtained by MIP, the basal spacings were distinct for pellets and block samples, even for those samples coming from tests that had reached "full" saturation. As well, the basal spacings determined in samples from the in situ EB experiment (using the same procedure and methodology as in this work, Villar et al. 2014) tended to be higher for pellets samples than for block samples for similar water contents (Figure 66). Apart from the much longer maturation of the samples from the in situ test, they were saturated with Pearson water, whereas the samples from the laboratory tests were saturated with deionised water. None of these factors seem to have affected the interlayer hydration behaviour. For water contents below ~38%, the basal spacing increased with the water content, but for higher values the basal spacing was quite constant, irrespective of the water content. Both in the laboratory and in the in-situ samples, the transition between the 2 and the 3-layer hydrate took place for a range of water contents between 32 and 38%. The MX-80 samples from test CT31 had water contents below 32% and basal reflections between 1.52 and 1.58 nm, corresponding to a predominant 2-layer hydrate.

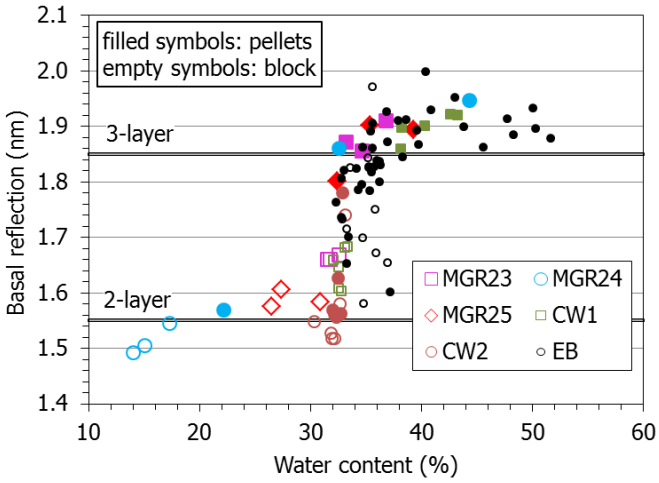

Figure 66. Main diffraction reflection of the basal reflection of subsamples of lab tests performed with FEBEX bentonite and of the EB in situ tests

6 SUMMARY AND CONCLUSIONS

The hydro-mechanical evolution of a two-component bentonite buffer material –low density pellets mixtures and higher density compacted blocks– was studied by means of a series of laboratory hydration tests performed under isochoric conditions. The tests were performed in a large-scale oedometer (10x10 cm) and in a transparent cell (12x12x2 cm) with FEBEX bentonite, and in an instrumented cell (15x15 cm) with MX-80 bentonite (test CT31). In the test with MX-80 bentonite the dry densities of the block and the pellets parts were similar. In the oedometer the axial pressure was measured on the sample surface opposite to hydration, whereas in the test with MX-80 bentonite, radial pressures and relative humidity were measured at different locations. In most tests hydration took place through the pellets part, but the effect of hydrating through the block was also checked. As well, tests were performed either under a low water injection pressure or under a low water inflow rate.

The analysis of the results obtained allowed to draw the following conclusions:

- Because of their low density and large macroporosity, hydration through the pellets was initially quick, even though the water injection pressure was very low.

- The way of hydration conditioned the water intake and the pressure development kinetics. Slow hydration (e.g. under a controlled low flow of through the block) delayed the start of pressure development, but allowed higher pressures to be reached for lower overall degrees of saturation. The reason could be the longer time available for water redistribution from the macropores to the microstructure (particularly the montmorillonite interlayer), which would be the responsible for swelling. The interplay between the different strengths of the two components may also be a relevant factor on the axial load measured at the first stages of saturation.

- Irrespective of the way of saturation (constant flow or pressure), the pressure development (both axial and radial, away from the hydration surface) was not continuous. After a first sharp increase (which was quicker under constant pressure), there was an intermediate period of pressure stabilisation. Only when the overall degree of saturation was very high, the pressure increased again until its final equilibrium value. This pressure development pattern had been previously observed also in samples of compacted bentonite and of pellets.

- The stress measuring devices reflect local stresses which are conditioned by the local dry density. Hence, when the block part was on top, the final pressure value of the saturated sample was higher than the value expected for smaller samples of bentonite compacted at the same average dry density. When the pellet part was on top, the contrary happened. Friction between the bentonite and the cell steel wall could also contribute to these differences. This research has put forward the necessity of using testing devices in which pressure can be measured at different locations to correctly assess the stress state of inhomogeneous samples. This was achieved in test CT31, where it was checked that the equilibrium pressure in the

middle part of the binary sample was higher than that at the bottom and on top, in relation with the dry density distribution.

- Bentonite water content and dry density gradients were observed at the end of the tests. For a given hydration rate they were dependent on the hydration time and, although they attenuated over time, they persisted even after full saturation was reached. Saturation under very low water inflow rate (either imposed or resulting from the low permeability of the block part when saturation took place through it) resulted in more uniform water contents and smoother gradients, also in terms of pore sizes. Even in a sample with homogeneous initial dry density in the pellets and the block parts, inhomogeneities persisted after full saturation, with higher water content and lower dry density in the proximity of the hydration surface.

- The microstructure of the bentonite in the two components was different even after full saturation. Despite the drastic reduction in the volume and size of macropores in the pellets parts, they continued to be higher than in the block part and consequently the e_m/e_M was lower in the pellets part. However, an overall trend to pore size homogenisation towards smaller sizes over time was observed. The basal spacing of the smectite, which is an indication of the number of water layers in the interlayer, was higher in pellets samples than in block samples.

- The water content and dry density gradients were not affected by the pellets/block interface. After full saturation the pellets/block interface was impervious to gas.

The behaviour of a two-component barrier can be affected by the particular dry density and water content of each barrier component as well as their size and geometry, and by the boundary conditions, such as the existence of gaps, temperature and water salinity and availability. This research has just analysed the effect of geometry and water availability, but there are not systematic published researches having analysed all the other aspects yet.

The evidence provided by these experimental results along with the outcomes of the large-scale EB test, in which a similar two-component barrier was tested for 10.5 years, suggests that, although the initial heterogeneity of the barrier system and the deformations induced in the first stages of saturation tend to attenuate over time, residual inhomogeneities will persist and remain even after full saturation. The kind and extent of these heterogeneities will depend on the initial and boundary conditions of the barrier.

7 REFERENCES

[1] Baryla, P., Bernachy-Barbe, F., Bosch, J.A., Campos, G., Carbonell, B., Daniels, K.A., Ferrari, A., Guillot, W., Gutiérrez-Álvarez, C., Harrington, J.F., Iglesias, R.J., Kataja, M., Mašín, D., Najser, J., Rinderknecht, F., Schäfer, T., Sun, H., Tanttu, J., Villar, M.V., Wieczorek, K. 2019. Bentonite mechanical evolution – experimental work for the support of model development and validation. DELIVERABLE (D4.1/2). Report. 132 pp.

[2] Bernachy-Barbe, F., Conil, N., Guillot, W., Talandier, J. 2020. Observed heterogeneities after hydration of MX-80 bentonite under pellet/powder form. Applied Clay Sience 189: 105542. https://doi.org/10.1016/j.clay.2020.105542

[3] Bosgiraud, J.M., Foin, R. 2016. Test report on FSS metric clayish material emplacement tests with clayish material definition and laboratory work on its performance. Project DOPAS Work Package 3 - Deliverable 3.7. European Commission Grant Agreement no. 323273, 35 pp. https://igdtp.eu/documents/

[4] Bian, X., Cui, Y.J., Zeng, L.L., Li, X.Z. 2019. Swelling behavior of compacted bentonite with the presence of rock fracture. Engineering Geology 254: 25-33. https://doi.org/10.1016/j.enggeo.2019.04.004

[5] Brunauer, S., Emmett, P.H., Teller, E. 1938. Adsorption of gases in multimolecular layers. Journal of the American Chemical Society 60: 309–319.

[6] Conil, N., Talandier, J., Noiret, A., Armand, G., Bosrigaud, J.M. 2015. Report on Bentonite Saturation Test (REM). DOPAS Work Package 4 Deliverable D4.2. European Commission Grant Agreement no. 323273, 97 pp. https://igdtp.eu/documents/

[7] Devineau, K., Bihannic, I., Michot, L., Villiéras, F., Masrouri, F., Cuisinier, O., Fragneto, G., Michau, N., 2006. In situ neutron diffraction analysis of the influence of geometric confinement of crystalline swelling of montmorillonite. Applied Clay Science 31 (1–2): 76–84. https://doi.org/10.1016/j.clay.2005.08.006

[8] Dixon, D., Chandler, N., Graham, J., Gray, M.N., 2002. Two large-scale sealing tests conducted at atomic energy of Canada's underground research laboratory: the buffer-container experiment and the isothermal test. Canadian Geotechnical Journal 39: 503–518. https://doi.org/10.1139/t02-012

[9] Dueck, A., Goudarzi, R., Börgesson, L. 2016. Buffer homogenisation. Status report 3. Technical Report SKB TR-16-04. Svensk Kärnbränslehantering, Stockholm, 104 pp.

[10] ENRESA 2005. Engineered barrier emplacement experiment in Opalinus Clay for the disposal of radioactive waste in underground repositories. Final Report. Publicación Técnica ENRESA 02/05. Madrid, 101 pp.

[11] ENRESA 2006. FEBEX Full-scale Engineered Barriers Experiment, Updated Final Report 1994–2004. Publicación Técnica ENRESA 05-0/2006, Madrid, 590 pp.

[12] Gómez-Espina, R. & Villar, M.V. 2016. Time evolution of MX-80 bentonite geochemistry under thermo-hydraulic gradients. Clay Minerals 51(2): 145-160. DOI: 10.1180/claymin.2016.051.2.03

[13] Grambow, B. 2016. Geological disposal of radioactive waste in clay. Elements 12: 239-245. DOI: 10.2113/gselements.12.4.239

[14] Gutiérrez-Rodrigo V, 2018. Transporte de gas en materiales de barrera. Tesis Doctoral. Universidad Complutense de Madrid. Colección Documentos CIEMAT. ISBN: 978-84-7834-802-2. Madrid, 303 pp.

[15] Gutiérrez-Rodrigo, V., Martín, P.L., Villar, M.V. 2021. Effect of interfaces on gas breaktrough pressure in compacted bentonite used as engineered barrier for radioactive waste disposal. Process Safety and Environmental Protection 149: 244-257. https://doi.org/10.1016/j.psep.2020.10.053.

[16] Harrington, J.F., Daniels, K.A., Wiseall, A.C., Sellin, P., 2020. Bentonite homogenisation within engineered cavities: the evolution of swelling pressure during bentonite hydration. International Journal of Rock Mechanics and Mining Sciences 136, 104535. doi:10.1016/j.ijrmms.2020.104535.

[17] Hoffmann, C. 2005. Caracterización hidromecánica de mezclas de pellets de bentonita. Estudio experimental y constitutivo. (PhD Thesis), Universitat Politècnica de Catalunya, Barcelona, 387 pp.

[18] Imbert, C., Villar, M.V. 2006. Hydro-mechanical response of a bentonite pellets/powder mixture upon infiltration. Applied Clay Science 32: 197-209. https://doi.org/10.1016/j.clay.2006.01.005

[19] Kennedy, K., Verfuss, F., Plötze, M. 2004. Engineered Barrier Emplacement (EB) Experiment in Opalinus Clay: Granular material backfill product documentation. EC contract FIKW-CT-2000-00017. Project Deliverable D3c. Mont Terri Technical Note 2004-17, 61 pp.

[20] Kröhn, K.P. 2005. New evidence for the dominance of vapour diffusion during the re-saturation of compacted bentonite. Engineering Geology 82: 127-132. https://doi.org/10.1016/j.enggeo.2005.09.015

[21] Martikainen, J., Pintado, X., Mamunul, H. 2018. Laboratory tests to evaluate bentonite homogenization. Internal memorandum POS-026579. Eurajoki, Finland: Posiva Oy.

[22] NAGRA 2019. Implementation of the Full-scale Emplacement Experiment at Mont Terri: Design, Construction and Preliminary Results. NAGRA Technical Report NTB 15-02. Wettingen, 147 pp.

[23] Pusch, R., Karnland, O., Hökmark, H. 1990. GMM -A general microstructural model for qualitative and quantitative studies on smectite clays. SKB Technical Report TR 90-43. Stockholm, 94 pp.

[24] Romero, E. 2013. A microstructural insight into compacted clayey soils and their hydraulic properties. Eng. Geol. 165: 3-19. http://dx.doi.org/10.1016/j.enggeo.2013.05.024

[25] Salo, J.P., Kukkola, T. 1989. Bentonite pellets, an alternative buffer material for spent fuel canister deposition holes. Workshop "Sealing of Radioactive Waste Repositories". Braunschweig.

[26] Sánchez M, Gens A, Guimarães L, Olivella, S, 2005. A double structure generalized plasticity model for expansive materials. International Journal for Numerical and Analytical Methods in Geomechanics 29: 751–787. DOI:10.1002/nag.434.

[27] Sellin, P., Leupin, O., 2013. The use of clays as an engineered barrier in radioactive-waste management – a review. Clays and Clay Minerals 61 (6): 477–498. https://doi.org/10.1346/CCMN.2013.0610601

[28] Sing, K.S.W., Everett, D.H., Haul, R.A.W., Moscou, L., Pierotti, R.A., Rouquérol, J., Siemieniewska, T. 1985. Reporting physisorption data for gas/solid systems with special reference to the determination of surface area and porosity. Pure and Applied Chemistry 57(4): 603-619. IUPAC.

[29] SKB. 2010. Buffer, Backfill and Closure Process Report for the Safety Assessment SR-Site. TR-10-47. Swedish Nuclear Fuel and Waste Management Co (SKB), Stockholm, 360 pp.

[30] Talandier, J. (Ed.) 2019. Synthesis of results from task 5.1. BEACON Deliverable D5.1.2. 334 pp.

[31] Van Geet, M., Volckaert, G., Roels, S. 2005. The use of microfocus X-ray computed tomography in characterising the hydration of a clay pellet/powder mixture. Applied Clay Science 29 (2): 73-87. https://doi.org/10.1016/j.clay.2004.12.007

[32] Villar, M.V. 1999. RESEAL Project. Topical Report on Laboratory Tests. Version 1. Informe Técnico CIEMAT/DIAE/54121/2/99. Madrid, 33 pp.

[33] Villar, M.V. 2002. Thermo-hydro-mechanical characterisation of a bentonite from Cabo de Gata. A study applied to the use of bentonite as sealing material in high level radioactive waste repositories. Publicación Técnica ENRESA 01/2002, Madrid, 258 pp.

[34] Villar, M.V. 2005. MX-80 bentonite. Thermo-hydro-mechanical characterisation performed at CIEMAT in the context of the Prototype Project. Informes Técnicos CIEMAT 1053. CIEMAT, Madrid, 39 pp.

[35] Villar MV, 2007. Water retention of two natural compacted bentonites. Clays and Clay Minerals 55(3): 311-322.

[36] Villar, M.V.(Ed). 2017. FEBEX-DP Postmortem THM/THC Analysis Report. NAB 16-017. 143 pp.

[37] Villar, M.V., Lloret, A. 2001. Variation of the intrinsic permeability of expansive clays upon saturation. In: Adachi, K., Fukue, M. (Eds.): Clay Science for Engineering. A.A. Balkema, Rotterdam, pp. 259–266.

[38] Villar MV, Gómez-Espina R, 2012a. Long-term Performance of Engineered Barrier Systems PEBS. Permeability tests in samples from the EB experiment at Mont Terri (Borehole EB-B1). Technical Note CIEMAT/DMA/2G210/06/12. Madrid, 15 pp.

[39] Villar MV, Gómez-Espina R, Gutiérrez-Nebot L, 2012b. Basal spacings of compacted bentonite. Applied Clay Science 65-66: 95-105.

[40] Villar, M.V., Gutiérrez-Rodrigo, V., Martín, P.L., Romero, F.J., Barcala, J.M. 2013. Gas transport in bentonite. Informes Técnicos CIEMAT 1301. Madrid, 63 pp. DOI: 10.13140/RG.2.2.14334.28489

[41] Villar, M.V., Campos, R., Gutiérrez-Nebot, L. 2014. EB experiment. Laboratory post-mortem analyses report. PEBS Project Deliverable D2.1-7. CIEMAT Technical Report CIEMAT/DMA/2G210/01/2014. Madrid, 34 pp.

[42] Villar MV, Carbonell B, Martín PL, Gutiérrez-Álvarez C, Barcala JM, 2018. Gas permeability of bentonite samples of the FEBEX Dismantling Project (FEBEX-DP). Informe Técnico CIEMAT 1431. Madrid, 89 pp.

[43] Villar, M.V., Campos, G., Gutiérrez-Nebot, L., Arroyo, X. 2019. Effect of prolonged drying at high temperature on the water retention capacity of bentonite (FEBEX-DP samples). Applied Clay Science 182: 105290. https://doi.org/10.1016/j.clay.2019.105290

[44] Villar, M.V., Iglesias, R.J., García-Siñeriz, J.L., Lloret, A., Huertas, F. 2020. Physical evolution of a bentonite buffer during 18 years of heating and hydration. Engineering Geology 264: 105408. https://doi.org/10.1016/j.enggeo.2019.105408

[45] Villar, M.V., Iglesias, R.J., Gutiérrez-Álvarez, C., Carbonell, B. 2021a. Pellets/block bentonite barriers: laboratory study of their evolution upon hydration. Engineering Geology 106272. https://doi.org/10.1016/j.enggeo.2021.106272

[46] Villar, M.V., Carbonell, B., Martín, P.L., Gutiérrez-Álvarez, C. 2021b. The role of interfaces in the bentonite barrier of a nuclear waste repository on gas transport. Engineering Geology 286: 106087. https://doi.org/10.1016/j.enggeo.2021.106087

[47] Villar, M.V. et al. 2022. Project Beacon. Saturation of a Block/Pellets Barrier of MX-80 Bentonite (Test CT31). Technical Report CIEMAT/DMA/2G220/1/22. Madrid, 45 pp.

[48] Volckaert, G., Bernier, F., Alonso, E., Gens, A., Samper, J., Villar, M.V., Martín, P.L., Cuevas, J., Campos, R., Thomas, H.R., Imbert, C., Zingarelli, V. 1996. Thermal-hydraulic-mechanical and geochemical behaviour of the clay barrier in radioactive waste repositories (model development and validation). Nuclear science and technology. EUR 16744. Commission of the European Communities, Luxembourg, 722 pp.

[49] Yuan, S., Liu, X., Romero, E., Delage, P., Buzzi, O. 2020. Discussion on the separation of macropores and micropores in a compacted expansive clay. Géotechnique Letters 10: 1–7. https://doi.org/10.1680/jgele.20.00056

ANNEX: DETAIL OF TESTS RESULTS

LARGE-SCALE OEDOMETER (MGR)

TEST MGR21

Table A- 1. Characteristics of test MGR21

Characteristics	Data
Material bottom	FEBEX pellets (EB)
Material top	FEBEX block
Hydration, water, pressure	Through bottom, deionised water, 15 kPa
Duration	34 days (Aug-Sep 2017)
Diameter	10 cm
Height	10 cm

Table A- 2. Initial and final characteristics of test MGR21

	Initial				Final			
	w (%)	h (cm)	ρ_d (g/cm^3)	S_r (%)	w (%)	ρ_d (g/cm^3)	h (cm)	S_r (%)
Average[a]	-	-	-	-	29.0	1.43	10.00	88
Pellets	9.5	4.97	1.26	23	35.9	1.31	4.80	91
Block	13.3	5.01	1.60	52	22.9	1.5	5.33	78
Average[b]	11.6	9.98	1.43	35	28.6	1.41	10.13	85

[a] from online measurements, [b] from measurement of dimensions and water content, the final values affected by decompression

Table A- 3. Axial pressure, vertical deformation, water intake, dry density (ρ_d), water content (w) and degree of saturation (S_r) recorded during hydration. MGR21

Time hydration (days)	Axial pressure (MPa)	Vertical deformation (mm)	Water intake (cm^3)	ρ_d (g/cm^3)	w (%)	S_r (%)
0	0.00	0.00	0	1.43	11.6	35
1	0.26	0.06	31	1.43	14.4	44
2	0.24	0.06	48	1.43	15.9	49
3	0.23	0.06	62	1.43	17.2	52
4	0.25	0.06	76	1.43	18.4	56
7	0.42	0.08	101	1.43	20.6	63
10	0.65	0.10	117	1.43	22.0	67
14	0.97	0.14	141	1.43	24.2	74
21	1.45	0.18	165	1.43	26.3	80
34	1.91	0.21	195	1.43	29.0	88

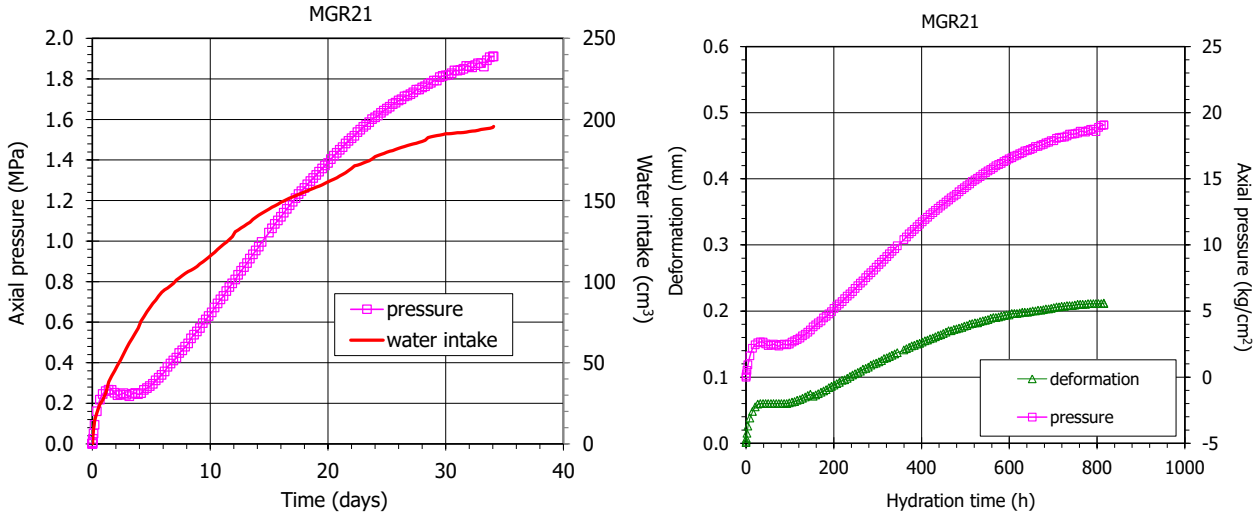

Figure A- 1 Evolution of axial pressure, axial strain and water intake in test MGR21

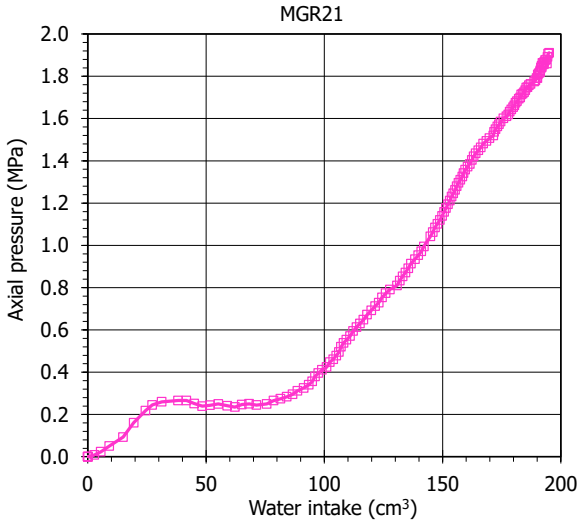

Figure A- 2 Evolution of axial pressure with water intake in test MGR21

Table A- 4. Final values along the column determined by mercury immersion and oven drying

Distance to hydration	w (%)	ρ_d (g/cm^3)	S_r (%)
9.25	20.7	1.48	66
7.47	22.1	1.50	73
5.69	25.7	1.44	77
4.00	30.9	1.37	87
2.40	35.5	1.31	88
0.80	41.1	1.26	97
Average[a]	28.5	1.39	82

[a] w and S_r weighted by dry density of each subsample

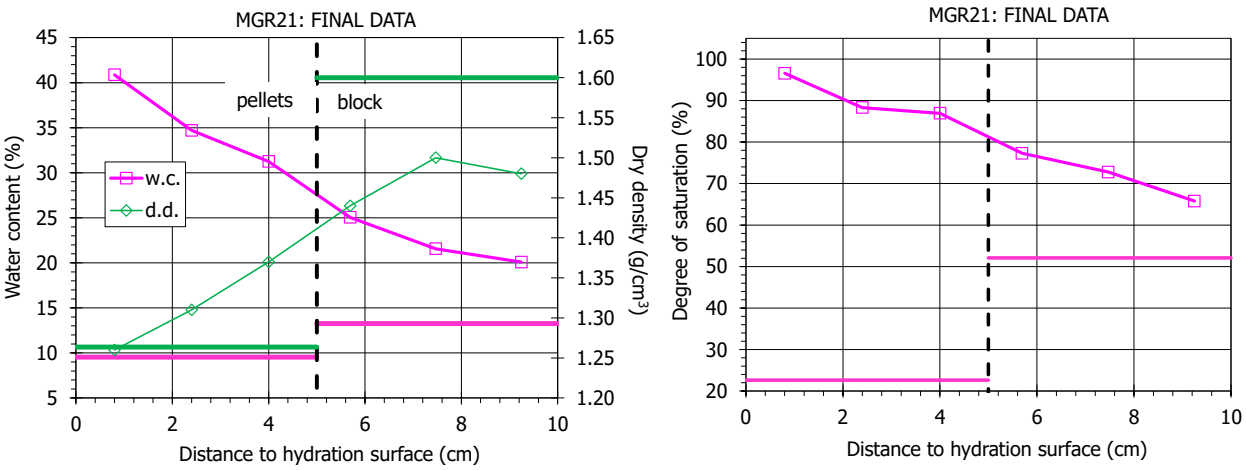

Figure A- 3. Final values measured along the column

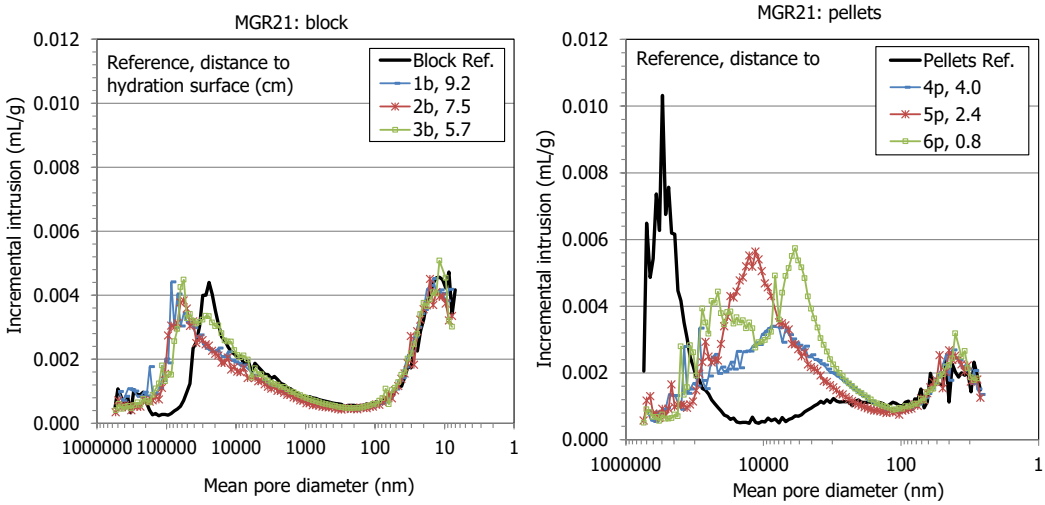

Figure A- 4. Pore size distribution of samples from block (left) and pellets (right)

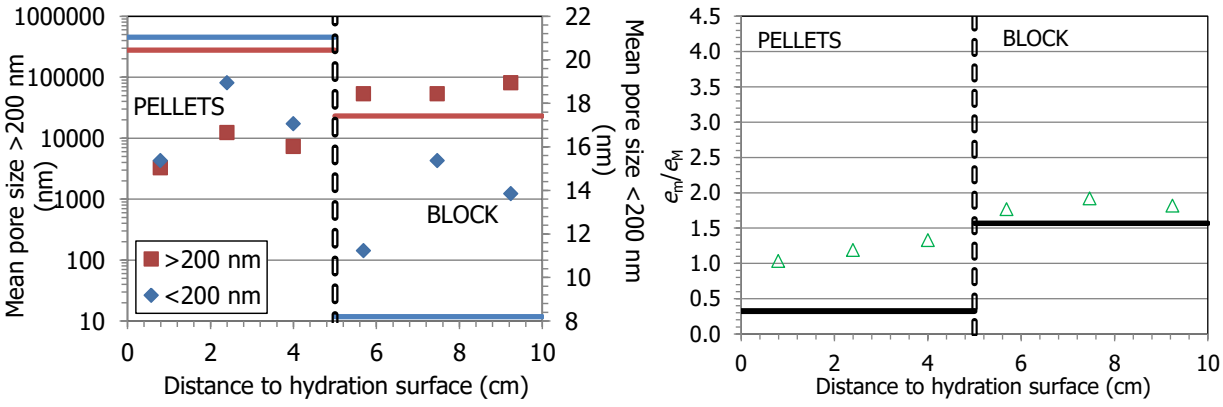

Figure A- 5. Test MGR21: Mean pore size for values above and below 200 nm (left); relation between void ratio corresponding to pores smaller (e_m) and larger (e_M) than 200 nm (right)

Table A- 5. Pore size distribution obtained with MIP of samples from MGR21 test (e: void ratio)

Reference	Distance to hydration (cm)	Intruded *e* (% of total)	*e* pores >200 nm (-)	Mode pores >200 (nm)	*e* pores <200 nm (-)	Mode pores <200 (nm)
1b	9.2	57	0.293	80849	0.532	14
2b	7.5	56	0.274	53451	0.526	15
3b	5.7	56	0.316	53433	0.559	11
4p	4.0	57	0.719	7322	0.252	17
5p-rep	2.4	58	0.485	12356	0.577	19
6p	0.8	61	0.562	3270	0.581	15
Pellets	-	47	0.826	277326	0.267	21
Block	-	68	0.302	20863	0.401	9

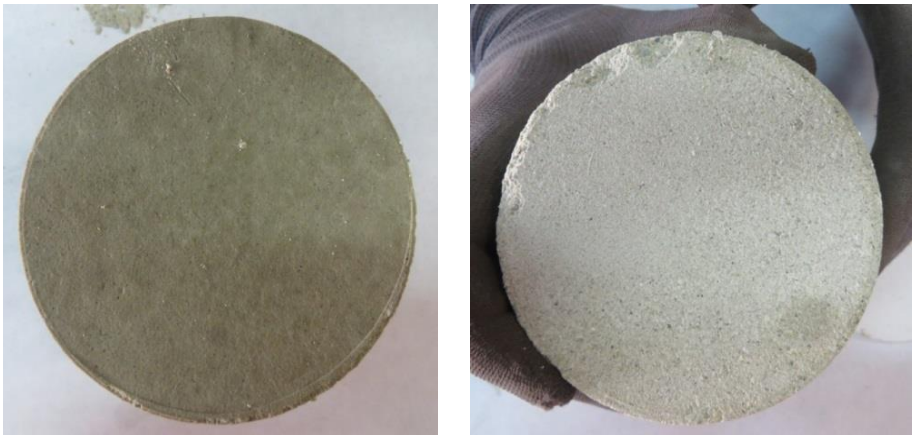

Figure A- 6. Bottom pellets (left) and upper block (right) appearance after the MGR21 test

Figure A- 7. Left: appearance of the column after extraction from the test cell MGR 21 (bottom: pellets, top: block); right: separation of the two parts for sampling

TEST MGR22

Table A- 6. Characteristics of test MGR22

Characteristics	Data
Material bottom	FEBEX pellets (EB)
Material top	FEBEX block
Hydration, water, pressure	Through bottom, deionised water, ramp of 0.048 cm^3/h
Duration	266 days (Oct 2017- Jul 2018)
Diameter	10 cm
Height	10 cm

Table A- 7. Initial and final characteristics of test MGR22

	Initial				Final			
	w (%)	h (cm)	ρ_d (g/cm^3)	S_r (%)	w (%)	ρ_d (g/cm^3)	h (cm)	S_r (%)
Average[a]	-	-	-	-	33.9	1.44	10.01	105
Pellets	9.9	5.04	1.28	24	35.3	1.35	4.79	95
Block	13.6	4.94	1.61	55	30.7	1.51	5.27	106
Average[b]	11.9	9.98	1.45	37	32.7	1.43	10.06	100

[a] from online measurements, [b] from measurement of dimensions and water content, the final values affected by decompression

Table A- 8. Axial pressure, vertical deformation, water intake, dry density (ρ_d), water content (w) and degree of saturation (S_r) recorded during hydration. MGR22

Time hydration (days)	Axial pressure (MPa)	Vertical deformation (mm)	Water intake (cm^3)	ρ_d (g/cm^3)	w (%)	S_r (%)
0	0.00	0.01	0	1.45	11.9	37
1	0.00	0.01	1	1.45	12.0	37
2	0.00	0.01	2	1.45	12.1	38
3	0.00	0.01	2	1.45	12.1	38
4	0.00	0.01	2	1.45	12.1	38
7	0.03	0.03	2	1.45	12.1	38
10	0.07	0.05	2	1.45	12.1	38
14	0.20	0.09	5	1.44	12.4	39
21	0.65	0.16	11	1.44	12.9	40
34	1.35	0.22	26	1.44	14.3	44
60	2.08	0.28	56	1.44	16.9	52
76	2.22	0.29	74	1.44	18.5	57
90	2.27	0.29	91	1.44	19.9	62
120	2.21	0.29	125	1.44	23.0	71
132	2.18	0.29	139	1.44	24.2	75
150	2.15	0.29	159	1.44	26.0	80
180	2.16	0.29	194	1.44	29.1	90
210	2.39	0.32	229	1.44	32.1	99
240	3.02	0.34	249	1.44	33.9	105
266	2.99	0.34	249	1.44	33.9	105

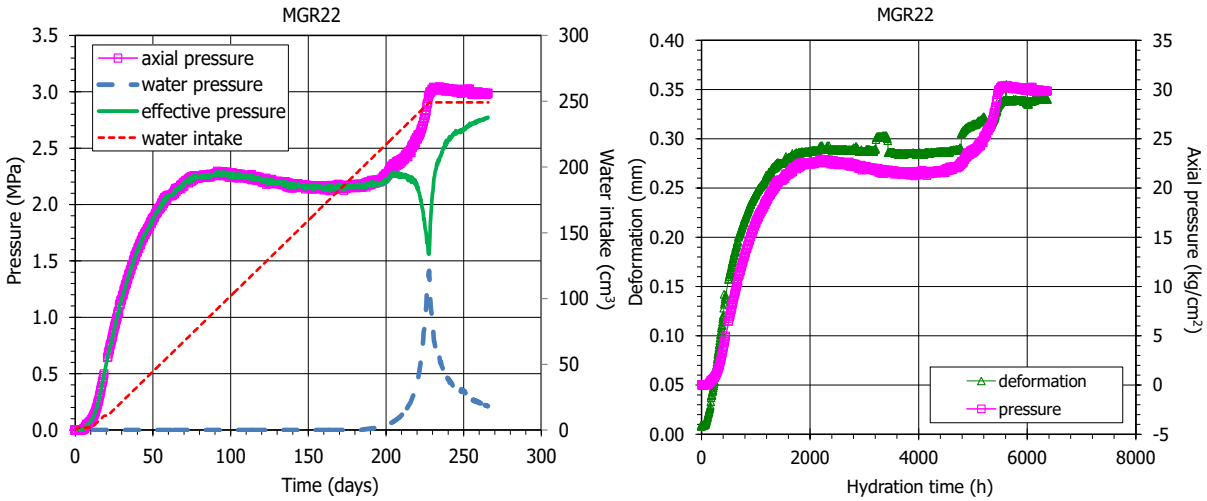

Figure A- 8. Evolution of axial and effective pressure, water intake and axial strain in test MGR22

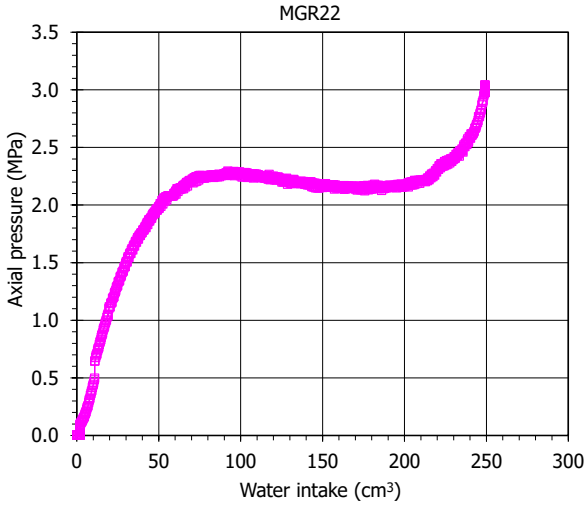

Figure A- 9. Evolution of axial pressure with water intake in test MGR22

Table A- 9. Final values along the column determined by mercury immersion and oven drying

Distance to hydration	w (%)	ρ_d (g/cm^3)	S_r (%)
9.18	30.3	1.46	96
7.42	30.5	1.45	95
5.67	31.3	1.44	96
3.99	33.2	1.41	98
2.39	34.2	1.39	98
0.80	35.0	1.39	100
Average[a]	32.4	1.42	97

[a] w and S_r weighted by dry density of each subsample

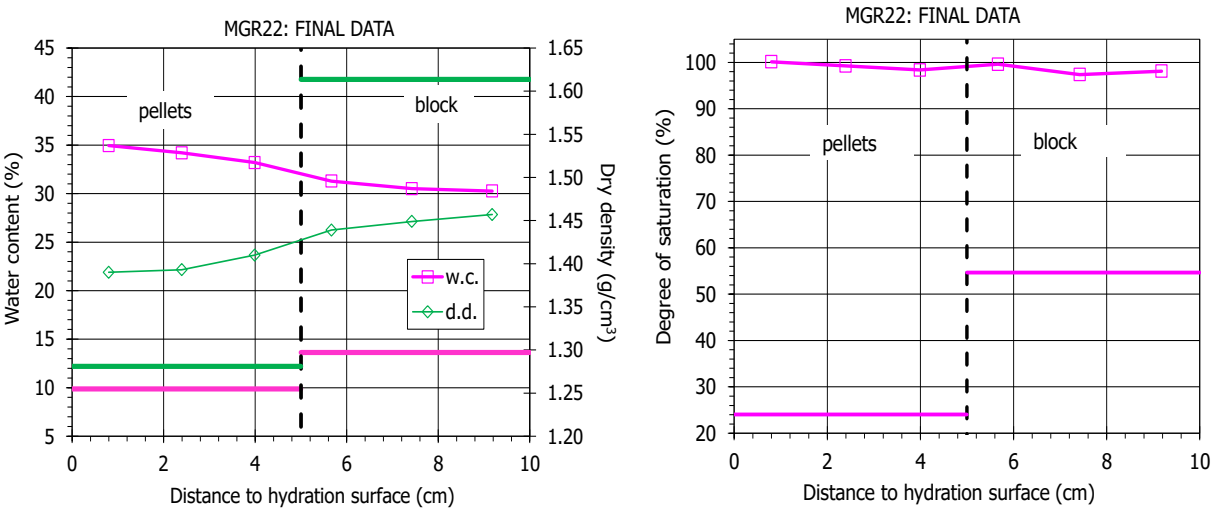

Figure A- 10. Final values measured along the column

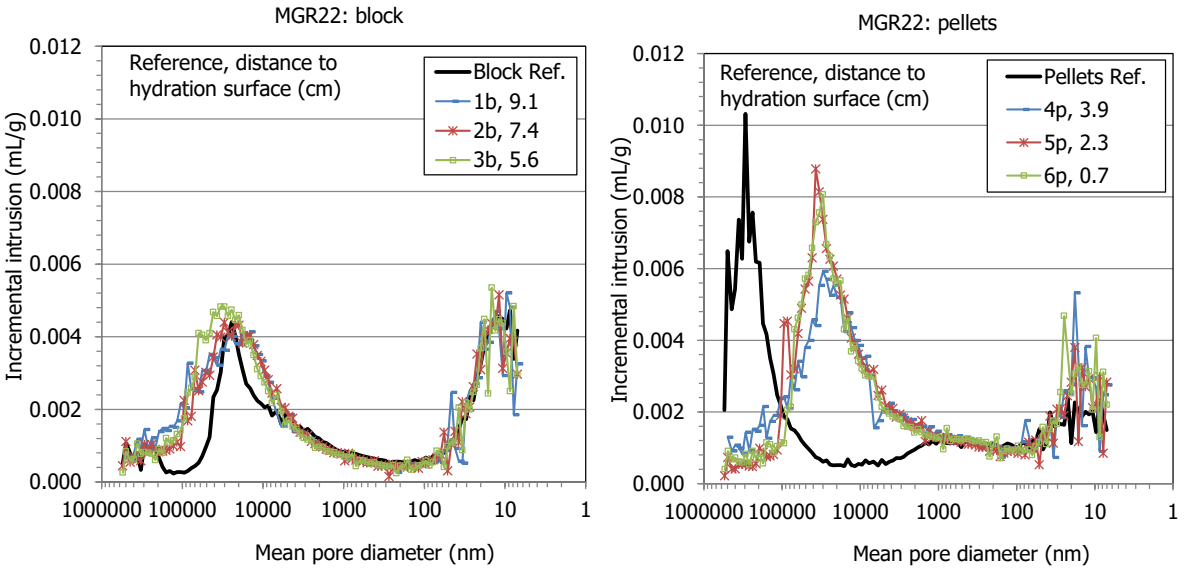

Figure A- 11. Pore size distribution of samples from block (left) and pellets (right)

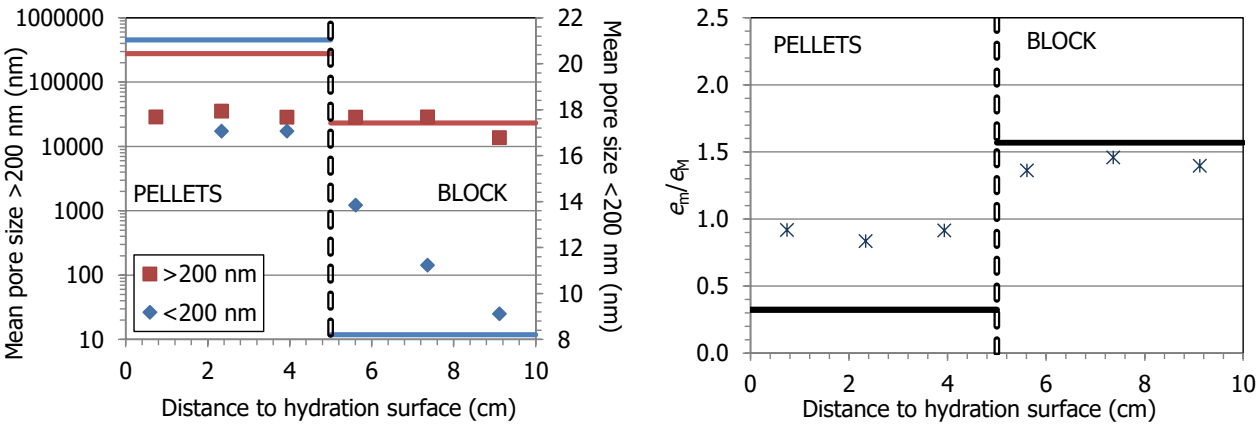

Figure A- 12. Test MGR22: Mean pore size for values above and below 200 nm (left); relation between void ratio corresponding to pores smaller (e_m) and larger (e_M) than 200 nm (right)

Table A- 10. Pore size distribution obtained with MIP of samples from MGR22 test (e: void ratio)

Reference	Distance to hydration (cm)	Intruded *e* (% of total)	*e* pores >200 nm (-)	Mode pores >200 (nm)	*e* pores <200 nm (-)	Mode pores <200 (nm)
1b	9.1	63	0.354	13714	0.495	9
2b	7.4	61	0.351	28561	0.511	11
3b	5.6	62	0.371	28545	0.504	14
4p	3.9	69	0.478	28543	0.437	17
5p	2.3	70	0.514	35208	0.429	17
6p	0.7	69	0.492	28549	0.451	23
Pellets	-	47	0.826	277326	0.267	21
Block	-	68	0.302	20863	0.401	9

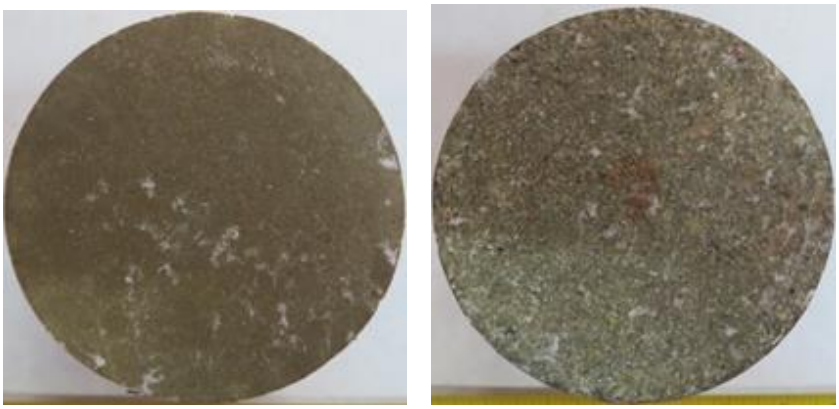

Figure A- 13. Bottom pellets (left) and upper block (right) appearance after the MGR22 test

Figure A- 14. Left: appearance of the column after extraction from the test cell MGR22 (bottom: pellets, top: block); right: separation of the two parts for sampling

TEST MGR23

Table A- 11. Characteristics of test MGR23

Characteristics	Data
Material bottom	FEBEX pellets (EB)
Material top	FEBEX block
Hydration, water, pressure	Through bottom, deionised water, 15 kPa
Duration	210 days (Aug 2018-March 2019)
Diameter	10 cm
Height	10 cm

Table A- 12. Initial and final characteristics of test MGR23

	Initial				Final			
	w (%)	h (cm)	ρ_d (g/cm^3)	S_r (%)	w (%)	ρ_d (g/cm^3)	h (cm)	S_r (%)
Average[a]	-	-	-	-	33.2	1.45	10.01	103
Pellets	3.5	5	1.30	9	35.7	1.34	4.84	95
Block	14.2	4.98	1.60	56	31.1	1.51	5.29	107
Average[b]	9.4	9.98	1.45	29	33.2	1.43	10.12	101

[a] from online measurements, [b] from measurement of dimensions and water content, the final values affected by decompression

Table A- 13. Axial pressure, vertical deformation, water intake, dry density (ρ_d), water content (w) and degree of saturation (S_r) recorded during hydration. MGR23

Time hydration (days)	Axial pressure (MPa)	Vertical deformation (mm)	Water intake (cm^3)	ρ_d (g/cm^3)	w (%)	S_r (%)
0	0.00	0.00	0	1.45	9.4	29
1	0.01	0.00	71	1.45	15.6	49
2	0.12	0.02	84	1.45	16.7	52
3	0.19	0.03	95	1.45	17.7	56
4	0.24	0.04	104	1.45	18.5	58
7	0.46	0.07	130	1.45	20.8	65
10	0.74	0.09	143	1.45	22.0	69
14	1.14	0.13	148	1.45	22.4	70
21	1.78	0.17	148	1.45	22.4	70
34	2.35	0.21	175	1.45	24.8	77
60	2.32	0.22	218	1.45	28.6	89
76	2.33	0.22	229	1.45	29.5	92
90	2.40	0.22	236	1.45	30.1	94
120	2.63	0.24	254	1.45	31.7	99
132	2.68	0.24	260	1.45	32.3	101
150	2.82	0.25	265	1.45	32.7	102
180	2.93	0.25	271	1.45	33.2	103
210	2.95	0.26	271	1.45	33.2	103

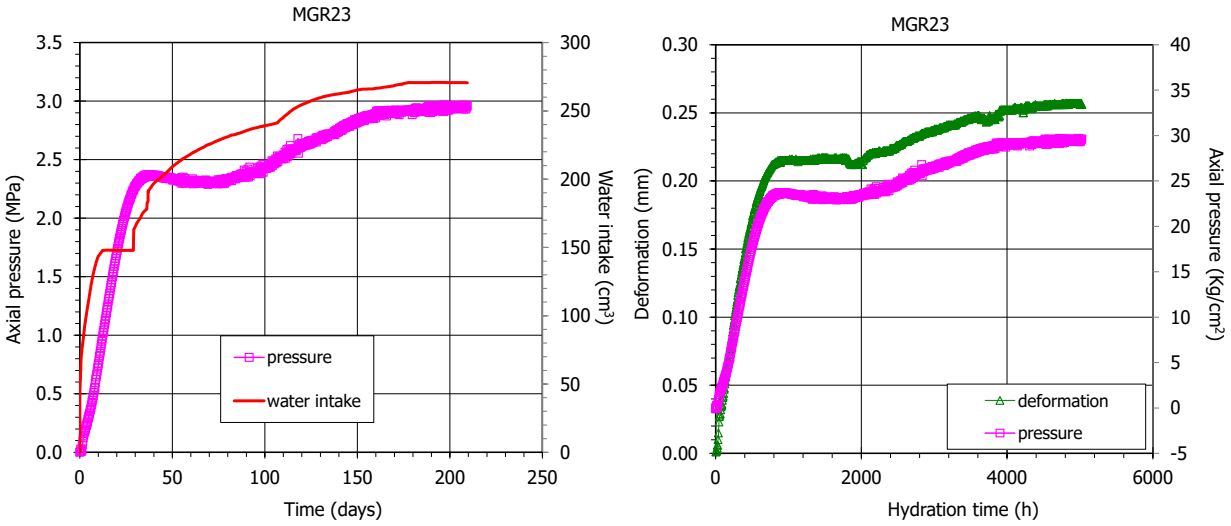

Figure A- 15. Evolution of axial pressure, axial strain and water intake in test MGR23

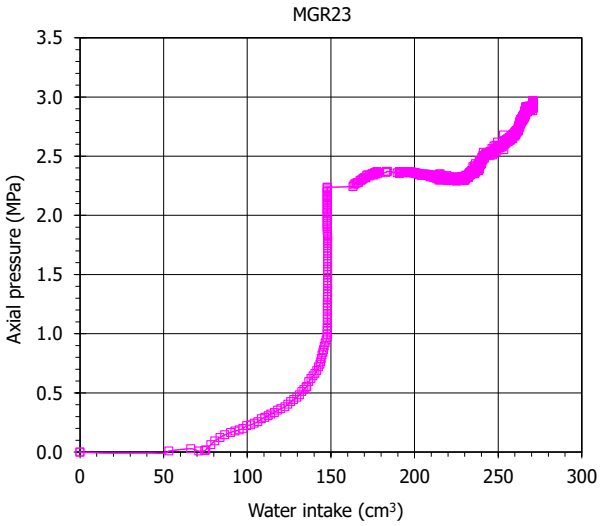

Figure A- 16. Evolution of axial pressure with water intake in test MGR23

Table A- 14. Final values along the column determined by mercury immersion and oven drying

Distance to hydration	w (%)	ρ_d (g/cm^3)	S_r (%)
9.24	31.6	1.46	100
7.48	31.8	1.45	100
5.72	32.5	1.44	100
4.03	33.3	1.42	99
2.42	34.7	1.37	97
0.81	36.8	1.37	102
Average[a]	33.4	1.42	100

[a] w and S_r weighted by dry density of each subsample

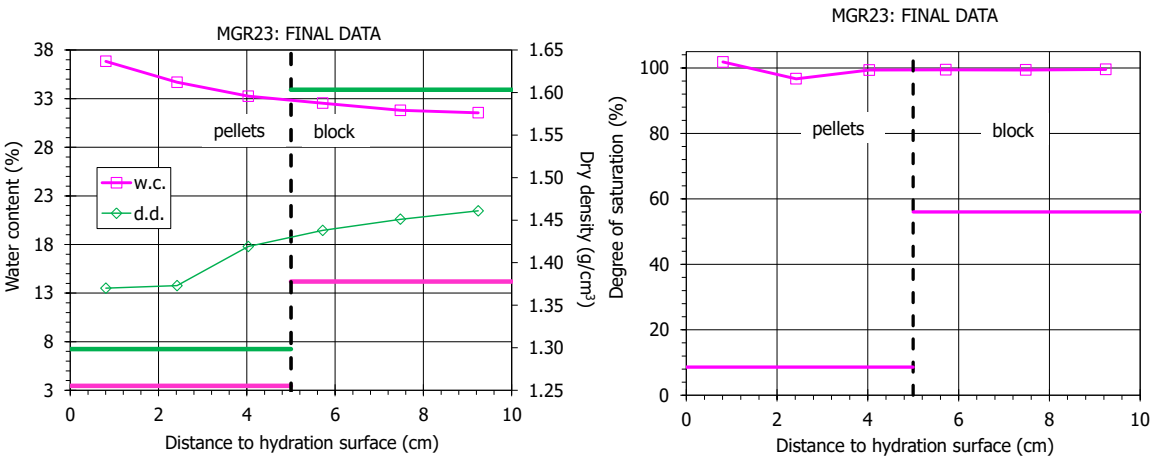

Figure A- 17. Final values measured along the column

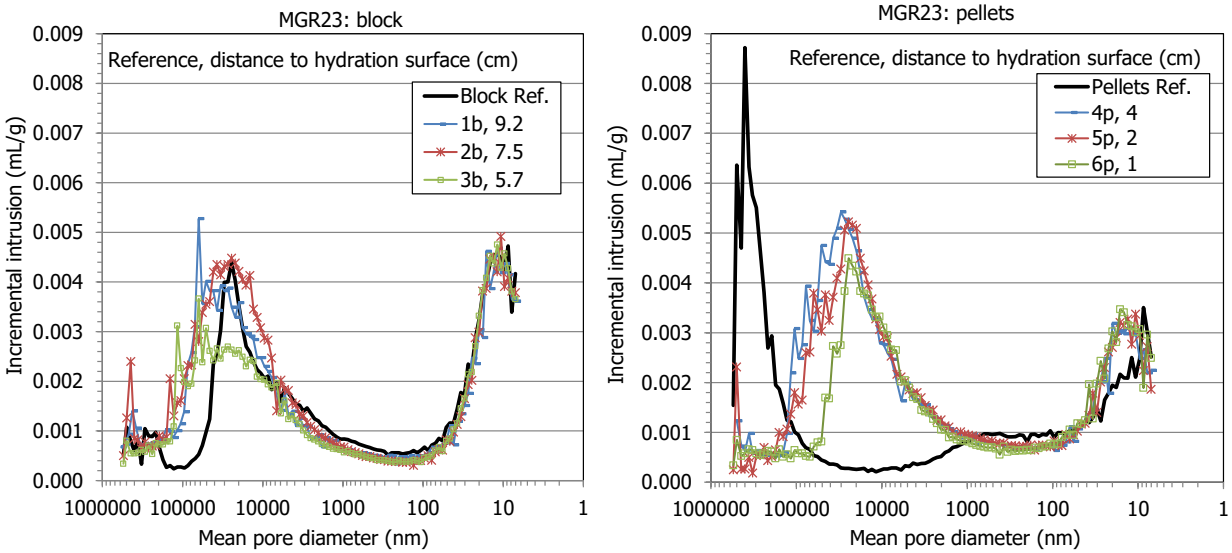

Figure A- 18. Pore size distribution of samples from block (left) and pellets (right)

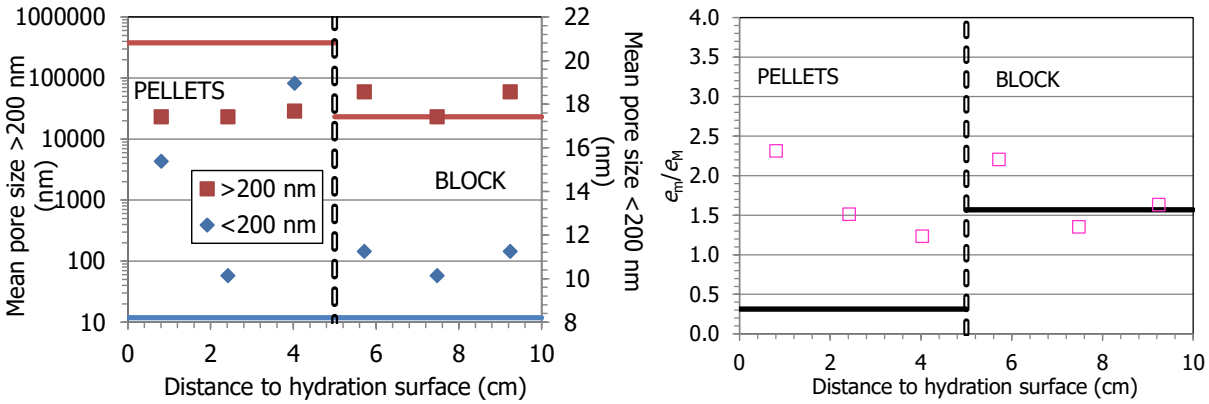

Figure A- 19. Test MGR23: Mean pore size for values above and below 200 nm (left); relation between void ratio corresponding to pores smaller (e_m) and larger (e_M) than 200 nm (right)

Table A- 15. Pore size distribution and BET surface area obtained with MIP and adsorption isotherms of samples from MGR23 (e: void ratio)

Reference	Distance to hydration (cm)	Intruded *e* (% of total)	*e* pores >200 nm (-)	Mode pores >200 (nm)	*e* pores <200 nm (-)	Mode pores <200 (nm)	BET a_s (m^2/g)	*t*-plot µ-pore volume (cm^3/g)
1b	9.2	58	0.322	59431	0.526	11	60	0.009
2b	7.5	62	0.366	23184	0.495	10	63	0.010
3b	5.7	51	0.274	59450	0.604	11	61	0.010
4p	4.0	61	0.404	28556	0.499	19	66	0.010
5p	2.4	55	0.385	23186	0.582	10	67	0.010
6p	0.8	46	0.293	23185	0.678	15	65	0.009
6p-rep	0.8	65	0.642	31700	0.571	14	n.d.	n.d.
Pellets	-	36	0.819	378852	0.258	8	59	0.010
Block	-	68	0.302	20863	0.401	9	60	0.008

Figure A- 20. Bottom pellets (left) and upper block (right) appearance after the MGR23 test

Figure A- 21. Appearance of the column after extraction from the test cell MGR 23 (left: pellets, right: block)

TEST MGR24

Table A- 16. Characteristics of test MGR24

Characteristics	Data
Material bottom	FEBEX pellets (EB)
Material top	FEBEX block
Hydration, water, pressure	Through bottom, deionised water, 15 kPa
Duration	14 days (March - April 2019)
Diameter	10 cm
Height	10 cm

Table A- 17. Initial and final characteristics of test MGR24

	Initial				Final			
	w (%)	*h* (cm)	ρ_d (g/cm^3)	S_r (%)	*w* (%)	ρ_d (g/cm^3)	*h* (cm)	S_r (%)
Average[a]	-	-	-	-	23.0	1.45	10.00	72
Pellets	5.7	5.02	1.28	14	31.0	1.30	4.93	78
Block	13.7	4.97	1.62	55	16.2	1.57	5.13	61
Average[b]	10.1	9.99	1.45	32	22.8	1.43	10.06	70

[a] from online measurements, [b] from measurement of dimensions and water content, the final values affected by decompression

Table A- 18. Axial pressure, vertical deformation, water intake, dry density (ρ_d), water content (w) and degree of saturation (S_r) recorded during hydration. MGR24

Time hydration (days)	Axial pressure (MPa)	Vertical deformation (mm)	Water intake (cm^3)	ρ_d (g/cm^3)	*w* (%)	S_r (%)
0	0.00	0.00	0	1.45	10.1	32
1	0.05	0.01	57	1.45	15.1	47
2	0.05	0.01	70	1.45	16.3	51
3	0.04	0.01	82	1.45	17.3	54
4	0.08	0.02	90	1.45	18.1	56
7	0.27	0.05	112	1.45	20.0	62
10	0.52	0.09	129	1.45	21.5	67
14	0.95	0.95	147	1.45	23.0	72

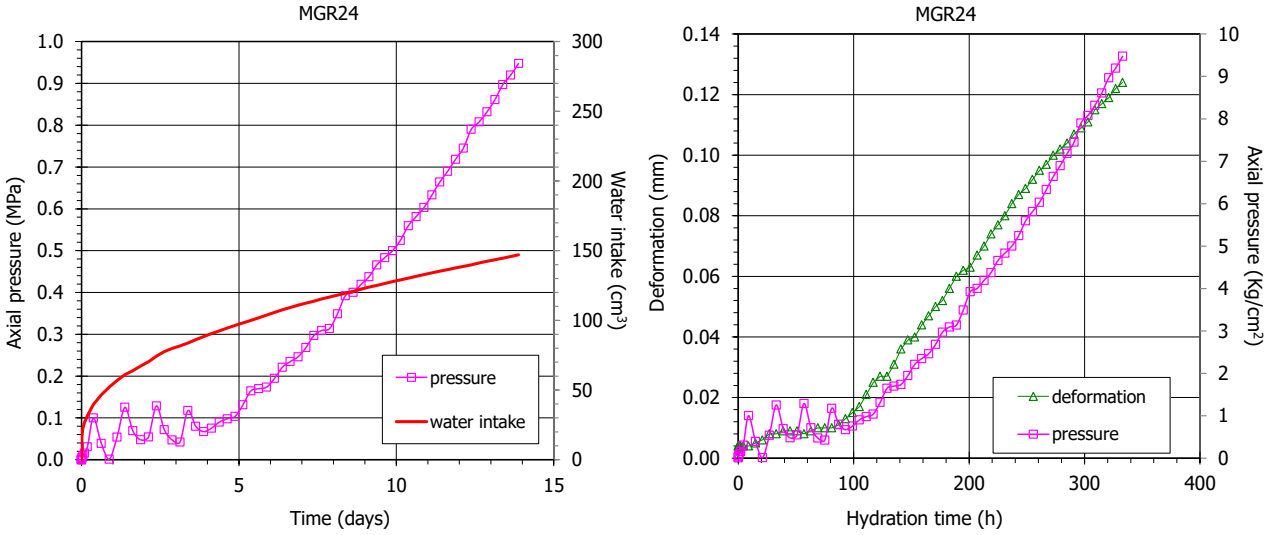

Figure A- 22. Evolution of axial pressure, axial strain and water intake in test MGR24

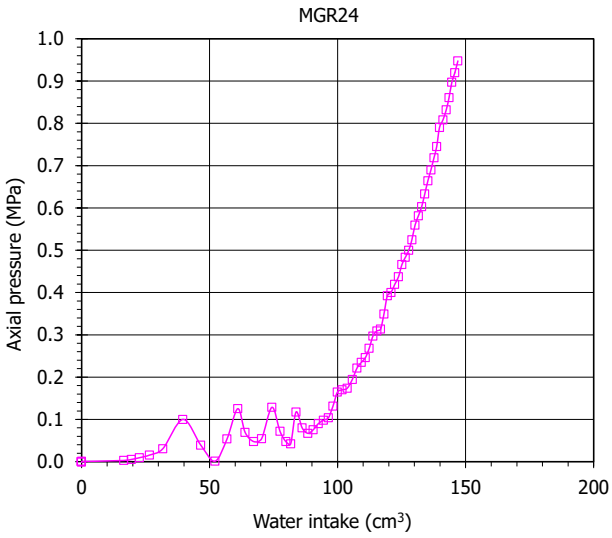

Figure A- 23. Evolution of axial pressure with water intake in test MGR24

Table A- 19. Final values along the column determined by mercury immersion and oven drying

Distance to hydration	w (%)	ρ_d (g/cm^3)	S_r (%)
9.20	14.1	1.59	55
7.49	15.0	1.58	58
5.78	17.3	1.54	62
4.11	22.2	1.35	60
2.46	32.6	1.33	85
0.82	44.3	1.22	99
Average[a]	23.3	1.44	71

[a] w and S_r weighted by dry density of each subsample

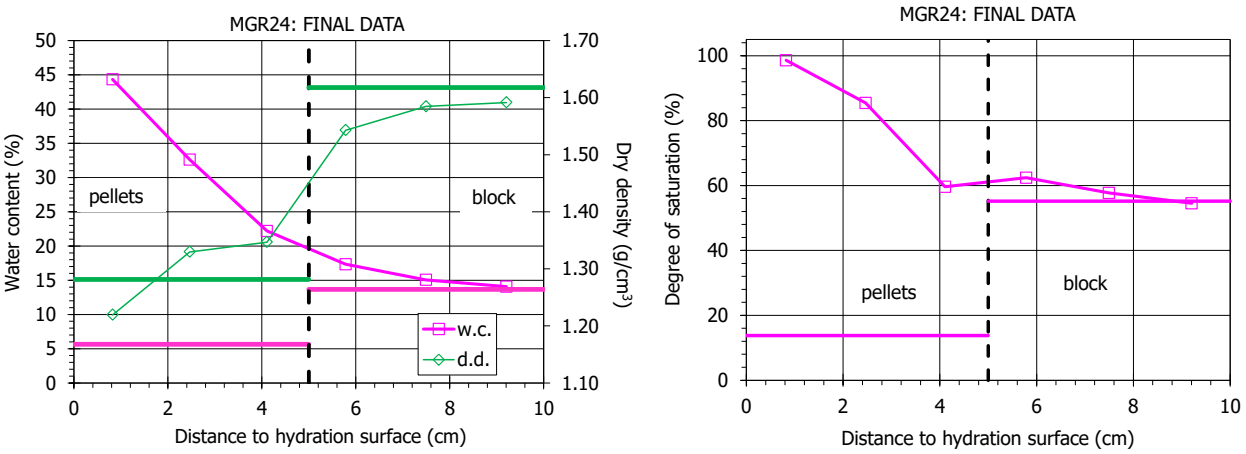

Figure A- 24. Final values measured along the column

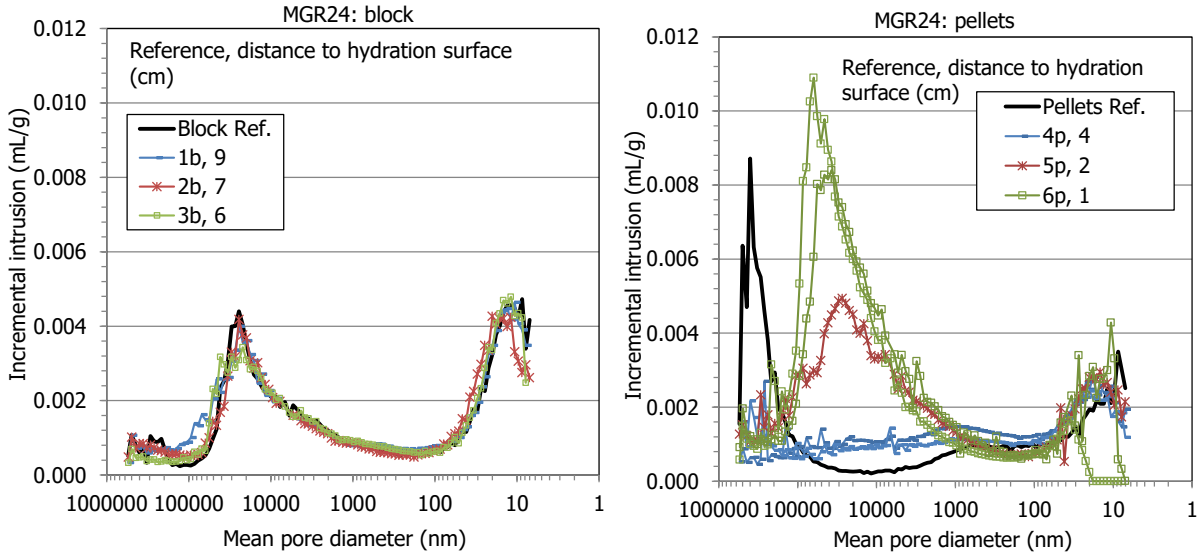

Figure A- 25. Pore size distribution of samples from block (left) and pellets (right)

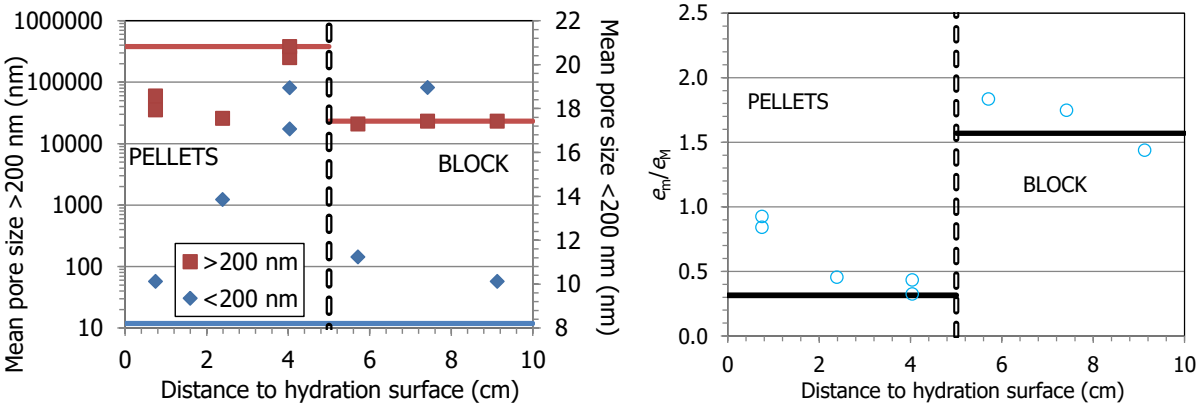

Figure A- 26. Test MGR24: Mean pore size for values above and below 200 nm (left); relation between void ratio corresponding to pores smaller (e_m) and larger (e_M) than 200 nm (right)

Table A- 20. Pore size distribution and BET surface area obtained with MIP and adsorption isotherms of samples from MGR24 (e: void ratio)

Reference	Distance to hydration (cm)	Intruded *e* (% of total)	*e* pores >200 nm (-)	Mode pores >200 (nm)	*e* pores <200 nm (-)	Mode pores <200 (nm)	BET a_s (m^2/g)	*t*-plot µ-pore volume (cm^3/g)
1b	9.1	67	0.286	23178	0.412	10	60	0.009
2b	7.4	63	0.258	23184	0.451	19	58	0.009
3b	5.7	59	0.266	20885	0.488	11	61	0.009
4p	4.0	38	0.698	250123	0.302	17	60	0.009
4p-rep	4.0	35	0.754	377209	0.246	19	n.d.	n.d.
5p	2.4	60	0.708	25730	0.322	14	67	0.010
6p	0.8	59	0.659	59450	0.554	32	65	0.010
6p-rep	0.8	63	0.630	35207	0.583	10	n.d.	n.d.
Pellets	-	36	0.819	378852	0.258	8	59	0.010
Block	-	68	0.302	20863	0.401	9	60	0.008

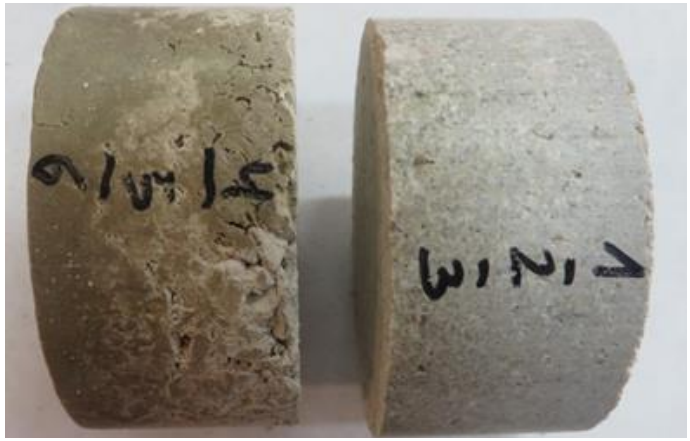

Figure A- 27. Appearance of the column after extraction from the test cell MGR 24 (left: pellets, right: block)

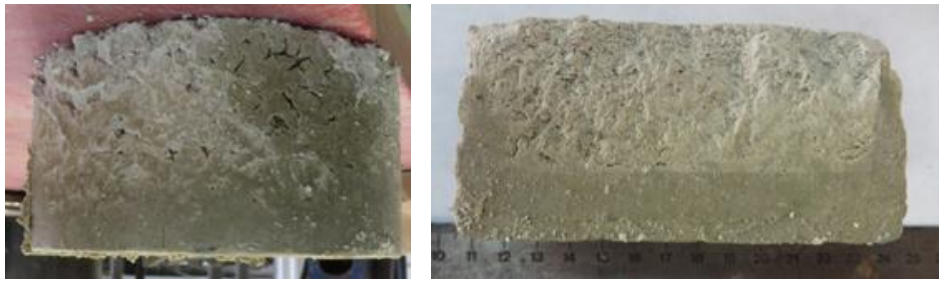

Figure A- 28. Samples from test MGR24 (left: preferential rise of water along the lateral surface; right: cross section of the pellets part)

TEST MGR25

Table A- 21. Characteristics of test MGR25

Characteristics	Data
Material bottom	FEBEX pellets (EB)
Material top	FEBEX block
Hydration, water, pressure	Through bottom, deionised water, 15 kPa
Duration	76 days (May-July 2019)
Diameter	10 cm
Height	10 cm

Table A- 22. Initial and final characteristics of test MGR25

	Initial				Final			
	w (%)	h (cm)	ρ_d (g/cm^3)	S_r (%)	w (%)	ρ_d (g/cm^3)	h (cm)	S_r (%)
Average[a]	-	-	-	-	23.0	1.45	10.00	72
Pellets	5.7	5.02	1.28	14	31.0	1.30	4.93	78
Block	13.7	4.97	1.62	55	16.2	1.57	5.13	61
Average[b]	10.1	9.99	1.45	32	22.8	1.43	10.06	70

[a] from online measurements, [b] from measurement of dimensions and water content, the final values affected by decompression

Table A- 23. Axial pressure, vertical deformation, water intake, dry density (ρ_d), water content (w) and degree of saturation (S_r) recorded during hydration. MGR25

Time hydration (days)	Axial pressure (MPa)	Vertical deformation (mm)	Water intake (cm^3)	ρ_d (g/cm^3)	w (%)	S_r (%)
0	0.00	0.01	0	1.44	9.2	29
1	0.04	0.03	9	1.44	10.0	31
2	0.08	0.04	17	1.44	10.6	33
3	0.12	0.07	23	1.44	11.2	35
4	0.17	0.09	30	1.44	11.8	37
7	0.40	0.14	46	1.44	13.2	41
10	0.66	0.18	63	1.44	14.8	46
14	1.12	0.23	88	1.44	16.9	52
21	1.76	0.28	123	1.44	20.1	62
34	2.24	0.31	170	1.44	24.2	75
60	2.19	0.31	233	1.44	29.7	92
76	2.20	0.31	252	1.44	31.4	97

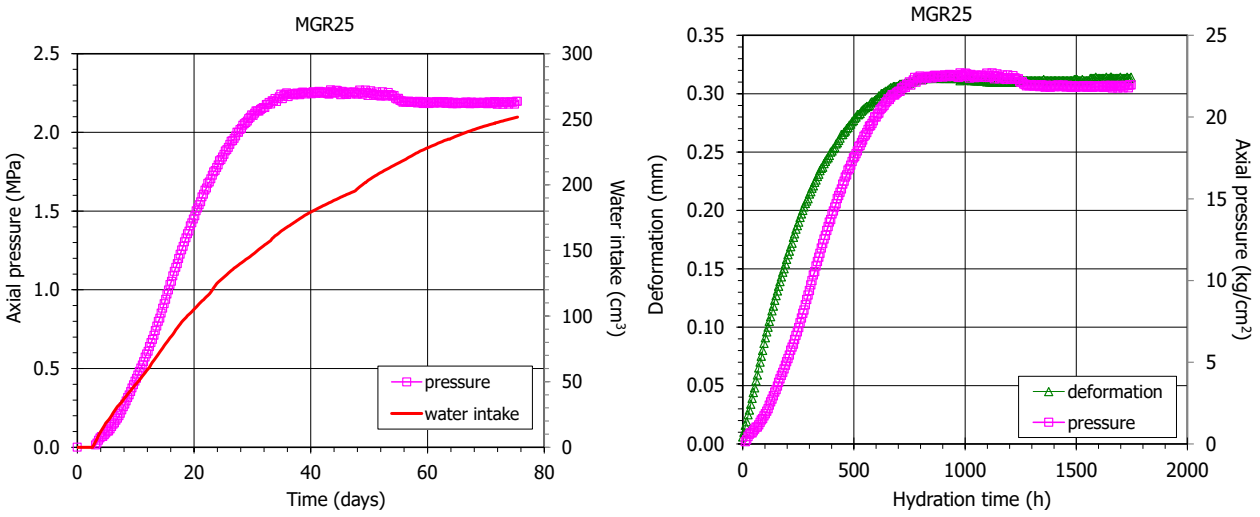

Figure A- 29. Evolution of axial pressure, axial strain and water intake in test MGR25

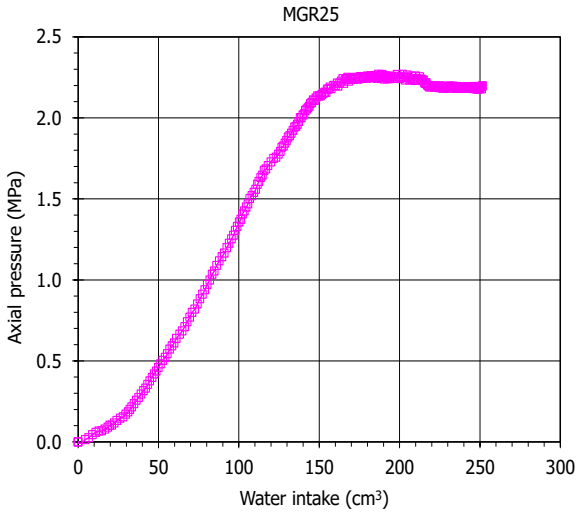

Figure A- 30. Evolution of axial pressure with water intake in test MGR25

Table A- 24. Final values along the column determined by mercury immersion and oven drying

Distance to hydration	w (%)	ρ_d (g/cm^3)	S_r (%)
9.24	26.5	1.49	88
7.50	27.4	1.48	90
5.75	30.9	1.44	95
4.06	32.4	1.41	96
2.43	35.4	1.38	100
0.81	39.3	1.32	102
Average[a]	31.8	1.42	95

[a] w and S_r weighted by dry density of each subsample

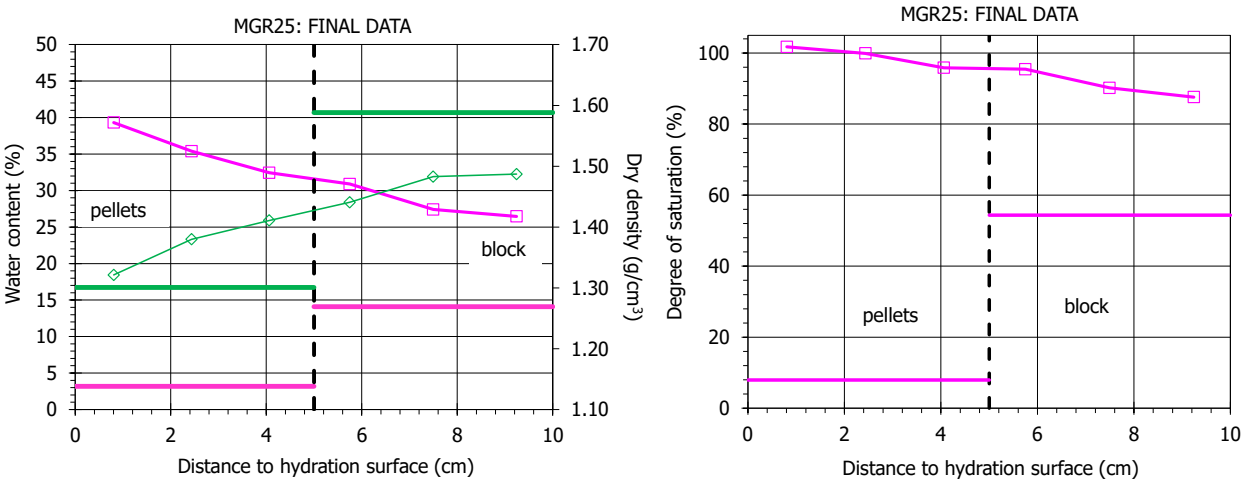

Figure A- 31. Final values measured along the column

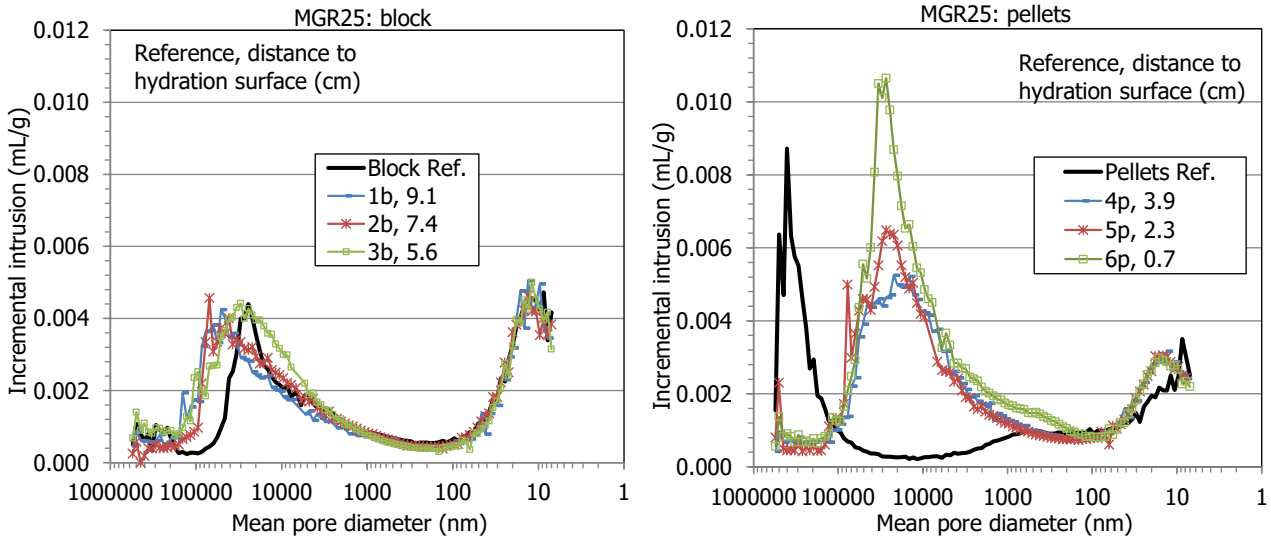

Figure A- 32. Pore size distribution of samples from block (left) and pellets (right)

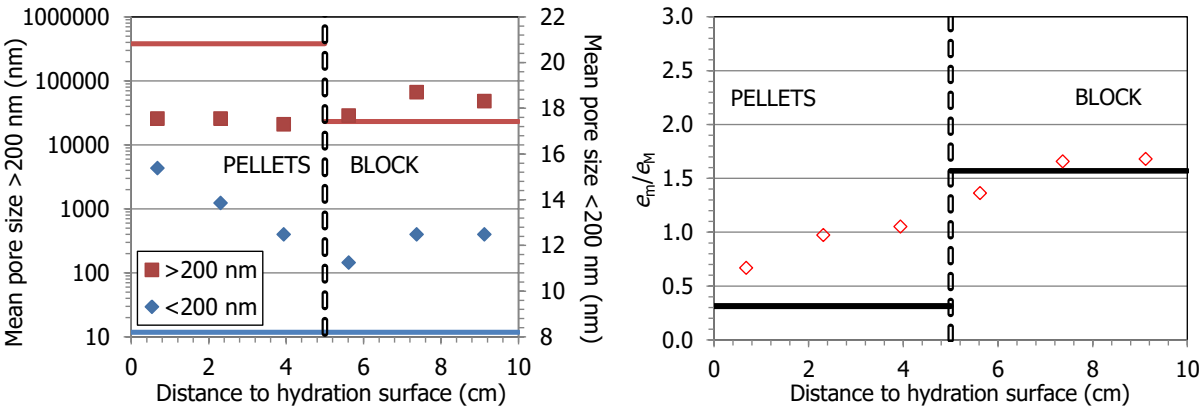

Figure A- 33. Test MGR25: Mean pore size for values above and below 200 nm (left); relation between void ratio corresponding to pores smaller (e_m) and larger (e_M) than 200 nm (right)

Table A- 25. Pore size distribution obtained with MIP, BET specific surface area and basal spacing of samples from MGR25 (e: void ratio)

Reference	Distance to hydration (cm)	Intruded *e* (% of total)	*e* pores >200 nm (-)	Mode pores >200 (nm)	*e* pores <200 nm (-)	Mode pores <200 (nm)	BET a_s (m^2/g)	*t* -plot µ-pore volume (cm^3/g)	d_{001} (nm)
1b	9.1	58	0.303	48237	0.509	12	59	0.008	15.27
2b	7.4	59	0.310	66092	0.514	12	58	0.009	15.23
3b	5.6	62	0.370	28562	0.505	11	63	0.009	14.89
4p	3.9	65	0.446	20882	0.469	12	64	0.010	15.59
5p	2.3	66	0.485	25734	0.472	14	71	0.010	15.22
6p	0.7	74	0.627	25727	0.419	15	68	0.010	14.92
Pellets	-	36	0.819	378852	0.258	8	59	0.010	14.80
Block	-	68	0.302	20863	0.401	9	60	0.008	14.80

Table A- 26. Semi-quantitative analysis of the crystalline phases in the powder bulk sample obtained by XRD. Values expressed as weight percentage

Reference	Quartz	Crist.	Tridy.	Phylos.	Plag.	K-Feld	Calcite	Dolom.	Goeth.	Magn.	Hemat.
1b	4	4	-	85	4	-	1	-	1	1	-
2b	4	1	1	87	3	-	3	-	-	1	-
3b	3	2	1	88	3	-	2	-	-	1	-
4p	9	3	3	67	11	1	-	5	-	1	-
5p	11	2	2	65	12	1	4	-	-	2	1
6p	8	4	4	66	11	1	4	-	-	2	-
Pellets	9	3	3	66	11	1	4	5		2	1
Block	4	2	1	87	3	-	2	-	1	1	-

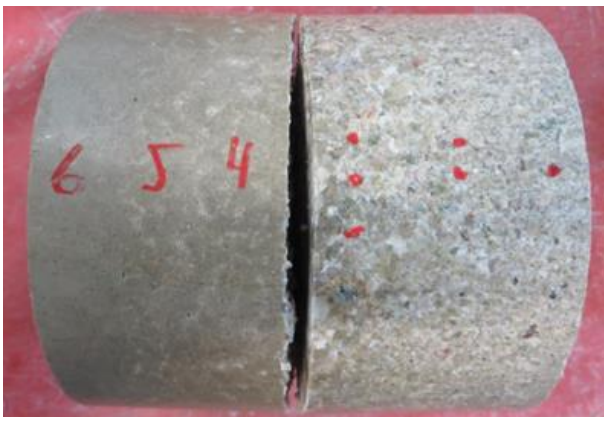

Figure A- 34. Bottom pellets (left) and upper block (right) appearance after the MGR25 test

TEST MGR26

Table A- 27. Characteristics of test MGR26

Characteristics	Data
Material bottom	FEBEX pellets (EB)
Material top	FEBEX block
Hydration, water, pressure	Through bottom, deionised water, ramp of 0.045 cm^3/h
Duration	132 days (Sep 2019 – Jan 2020)
Diameter	10 cm
Height	10 cm

Table A- 28. Initial and final characteristics of test MGR26

	Initial				Final			
	w (%)	h (cm)	ρ_d (g/cm^3)	S_r (%)	w (%)	ρ_d (g/cm^3)	h (cm)	S_r (%)
Average[a]	-	-	-	-	23.0	1.45	10.00	72
Pellets	5.7	5.02	1.28	14	31.0	1.30	4.93	78
Block	13.7	4.97	1.62	55	16.2	1.57	5.13	61
Average[b]	10.1	9.99	1.45	32	22.8	1.43	10.06	70

[a] from online measurements, [b] from measurement of dimensions and water content, the final values affected by decompression

Table A- 29. Axial pressure, vertical deformation, water intake, dry density (ρ_d), water content (w) and degree of saturation (S_r) recorded during hydration. MGR26

Time hydration (days)	Axial pressure (MPa)	Vertical deformation (mm)	Water intake (cm^3)	ρ_d (g/cm^3)	w (%)	S_r (%)
0	0.00	0.00	0	1.45	9.2	29
1	0.00	0.00	0	1.45	9.2	29
2	0.00	0.00	0	1.45	9.2	29
3	0.00	0.00	0	1.45	9.2	29
4	0.00	0.00	0	1.45	9.2	29
7	0.01	0.00	1	1.45	9.3	29
10	0.01	0.00	5	1.45	9.7	30
14	0.01	0.00	9	1.45	10.1	31
21	0.02	0.00	18	1.45	10.8	34
34	0.17	0.06	32	1.45	12.1	38
60	0.62	0.23	62	1.44	14.7	46
76	1.00	0.35	81	1.44	16.3	51
90	1.16	0.46	97	1.44	17.7	55
120	1.35	0.65	129	1.44	20.6	63
132	1.35	0.67	137	1.44	21.3	66

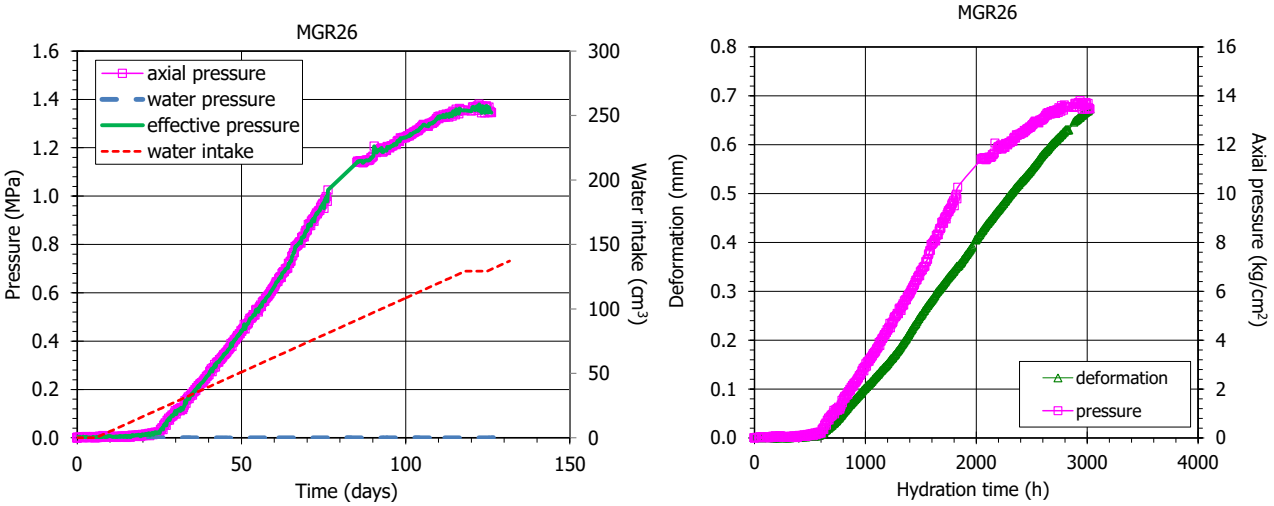

Figure A- 35. Evolution of axial and effective pressure, axial strain and water intake in test in test MGR26

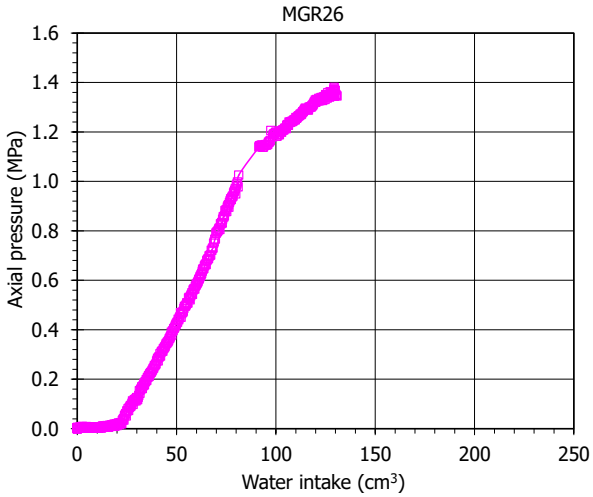

Figure A- 36. Evolution of axial pressure with water intake in test MGR26

Table A- 30. Final values along the column determined by mercury immersion and oven drying

Distance to hydration	w (%)	ρ_d (g/cm^3)	S_r (%)
9.39	19.9	1.50	67
7.60	20.8	1.50	70
5.82	21.5	1.48	70
4.10	19.1	1.39	55
2.46	21.0	1.37	58
0.82	22.4	1.39	64
Average[a]	20.8	1.44	64

[a] w and S_r weighted by dry density of each subsample

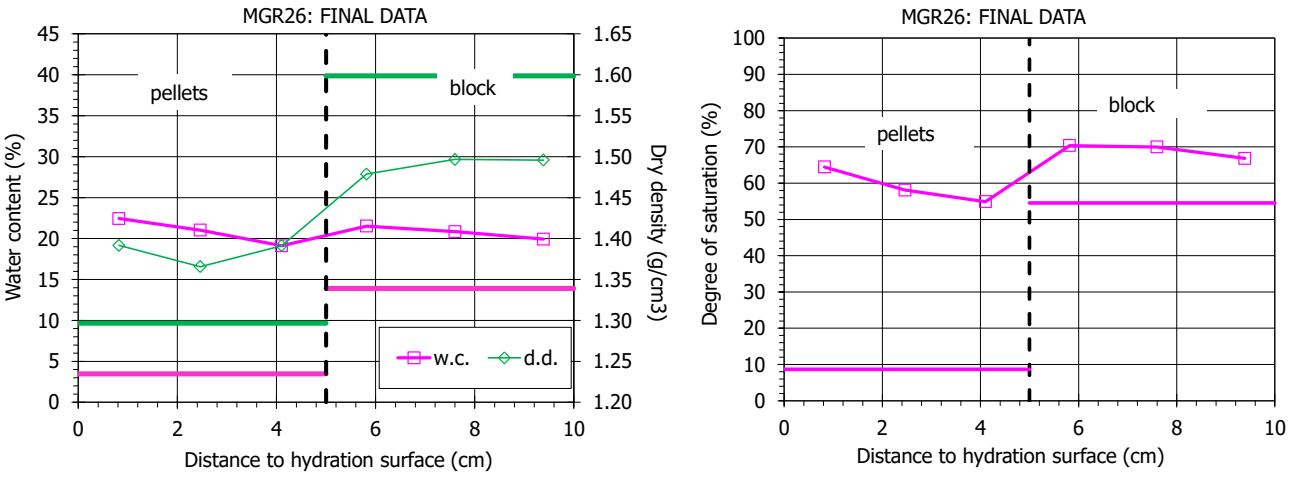

Figure A- 37. Final values measured along the column

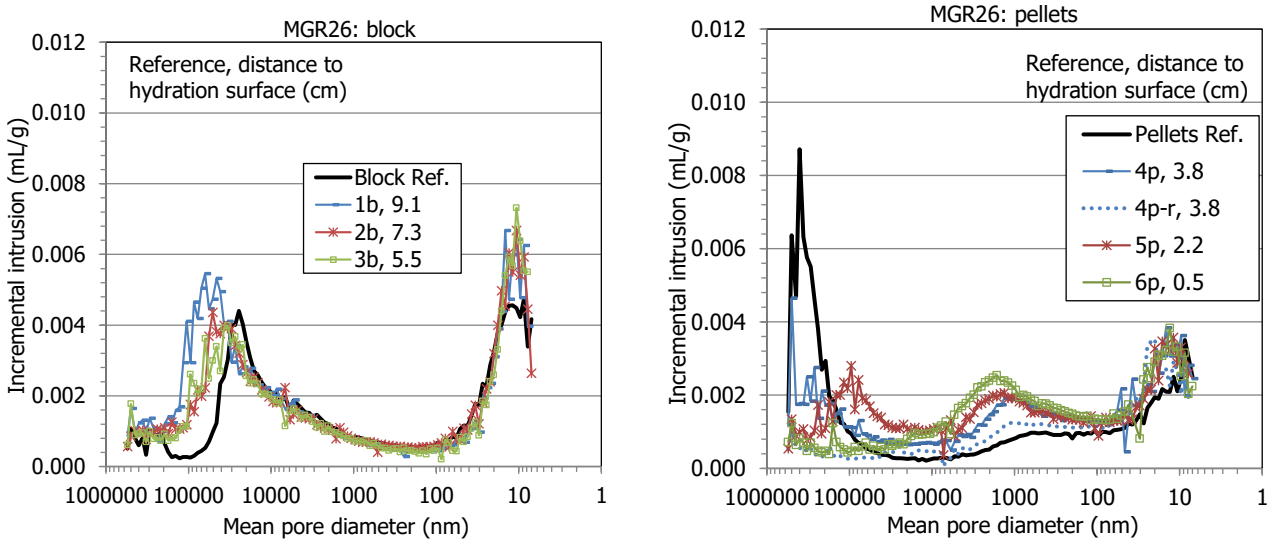

Figure A- 38. Pore size distribution of samples from block (left) and pellets (right)

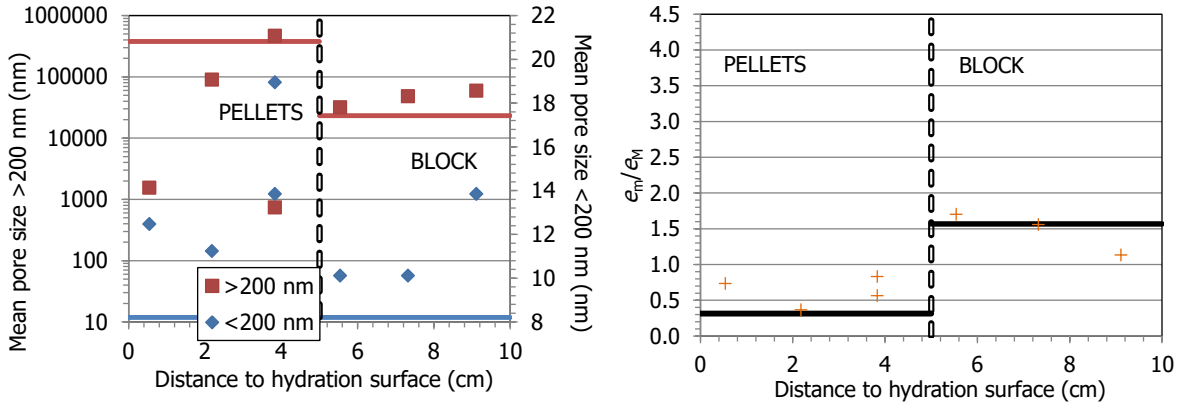

Figure A- 39. Test MGR26: Mean pore size for values above and below 200 nm (left); relation between void ratio corresponding to pores smaller (e_m) and larger (e_M) than 200 nm (right)

Table A- 31. Pore size distribution and BET surface area obtained with MIP and adsorption isotherms of samples from MGR26 (e: void ratio)

Reference	Distance to hydration (cm)	Intruded *e* (% of total)	*e* pores >200 nm (-)	Mode pores >200 (nm)	*e* pores <200 nm (-)	Mode pores <200 (nm)	BET a_s (m^2/g)	*t* -plot µ-pore volume (cm^3/g)
1b	9.1	70	0.378	59,491	0.427	14	54	0.008
2b	7.3	64	0.314	48,251	0.489	10	57	0.008
3b	5.5	60	0.306	31,719	0.520	10	56	0.008
4p	3.8	47	0.514	466,514	0.427	14	61	0.009
4p-rep	3.8	30	0.603	740	0.338	19	60	0.008
5p	2.2	48	0.717	90,016	0.259	11	60	0.009
6p	0.5	46	0.543	1,548	0.396	12	63	0.009
Pellets	-	36	0.819	378,852	0.258	8	59	0.010
Block	-	68	0.302	20,863	0.401	9	60	0.008

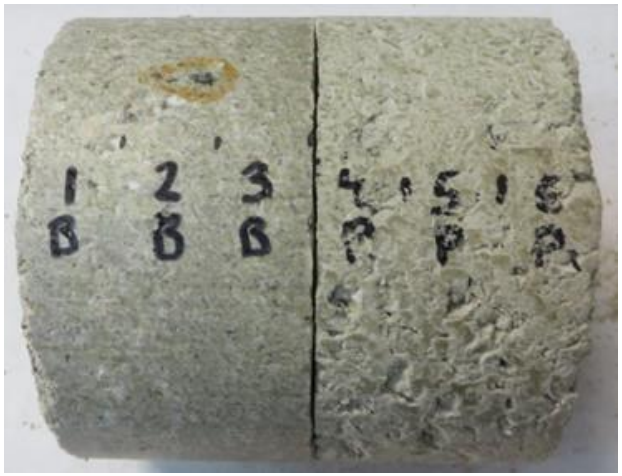

Figure A- 40. Appearance of the column after extraction from the test cell MGR26 (left: block, right: pellets). Rusty mark on section 2B

TEST MGR27

Table A- 32. Characteristics of test MGR27

Characteristics	Data
Material bottom	FEBEX block
Material top	FEBEX pellets (EB)
Hydration, water, pressure	Through bottom, deionised water, 15 kPa
Duration	278 days (Feb 2020 – Nov 2020)
Diameter	10 cm
Height	10 cm

Table A- 33. Initial and final characteristics of test MGR27

	Initial				Final			
	w (%)	h (cm)	ρ_d (g/cm^3)	S_r (%)	w (%)	ρ_d (g/cm^3)	h (cm)	S_r (%)
Average[a]	-	-	-	-	23.0	1.45	10.00	72
Pellets	5.7	5.02	1.28	14	31.0	1.30	4.93	78
Block	13.7	4.97	1.62	55	16.2	1.57	5.13	61
Average[b]	10.1	9.99	1.45	32	22.8	1.43	10.06	70

[a] from online measurements, [b] from measurement of dimensions and water content, the final values affected by decompression

Table A- 34. Axial pressure, vertical deformation, water intake, dry density (ρ_d), water content (w) and degree of saturation (S_r) recorded during hydration. MGR27

Time hydration (days)	Axial pressure (MPa)	Vertical deformation (mm)	Water intake (cm^3)	ρ_d (g/cm^3)	w (%)	S_r (%)
0	0.00	0.00	0	1.45	9.8	30
1	0.32	0.04	13	1.45	10.9	34
2	0.38	0.05	19	1.45	11.4	36
3	0.41	0.06	24	1.45	11.9	37
4	0.44	0.06	28	1.45	12.3	38
7	0.51	0.07	38	1.45	13.1	41
10	0.56	0.08	46	1.45	13.8	43
14	0.63	0.08	56	1.45	14.7	46
21	0.71	0.09	72	1.45	16.1	50
34	0.85	0.11	95	1.45	18.1	57
60	0.93	0.12	132	1.45	21.4	67
76	0.96	0.14	150	1.45	22.9	71
90	0.99	0.13	163	1.45	24.1	75
120	1.00	0.13	185	1.45	26.0	81
132	1.00	0.13	192	1.45	26.7	83
150	1.06	0.13	202	1.45	27.5	86
180	1.14	0.14	218	1.45	28.9	90
210	1.22	0.15	230	1.45	30.0	93
240	1.22	0.16	241	1.45	31.0	96
266	1.33	0.16	249	1.45	31.6	99
278	1.29	0.16	250	1.45	31.7	99

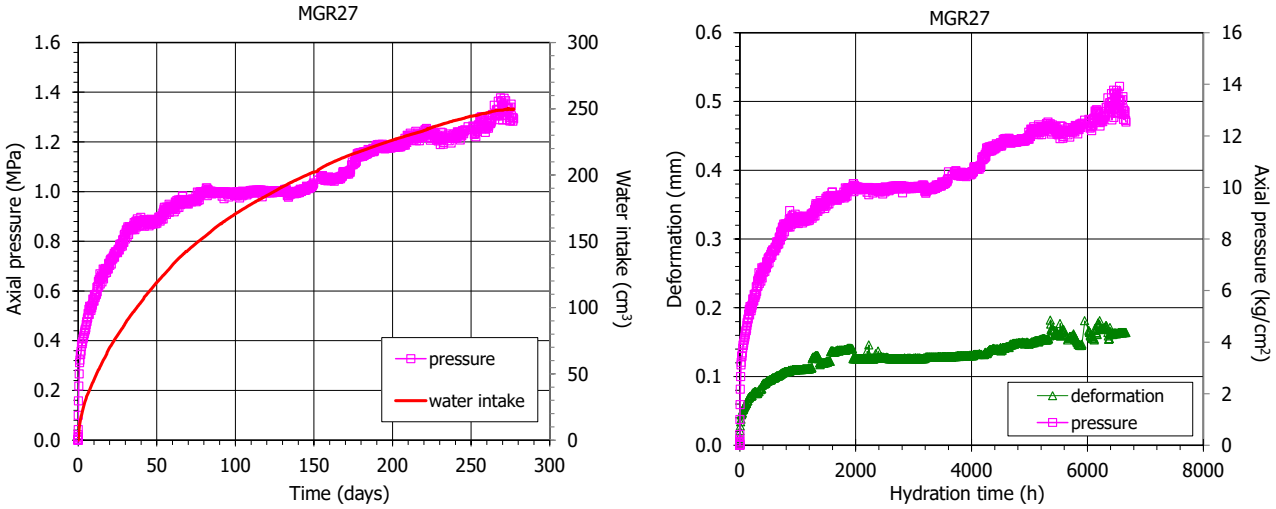

Figure A- 41. Evolution of axial pressure, axial strain and water intake in test MGR27

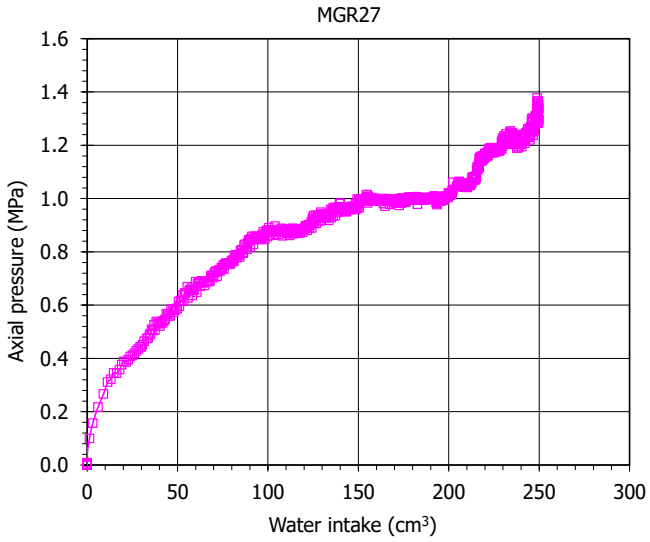

Figure A- 42. Evolution of axial pressure with water intake in test MGR27

Table A- 35. Final values along the column determined by mercury immersion and oven drying

Distance to hydration	w (%)	ρ_d (g/cm^3)	S_r (%)
9.26	28.9	1.42	87
7.75	29.2	1.44	91
6.23	29.3	1.45	92
4.56	30.6	1.45	96
2.75	31.0	1.44	96
0.91	32.4	1.42	97
Average[a]	30.2	1.44	93

[a] w and S_r weighted by dry density of each subsample

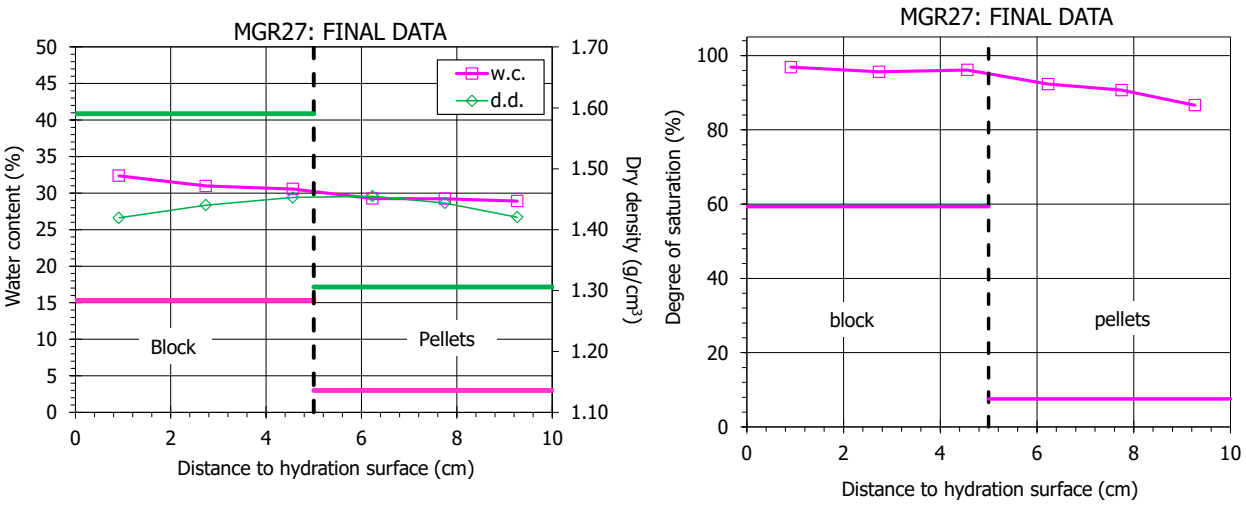

Figure A- 43. Final values measured along the column

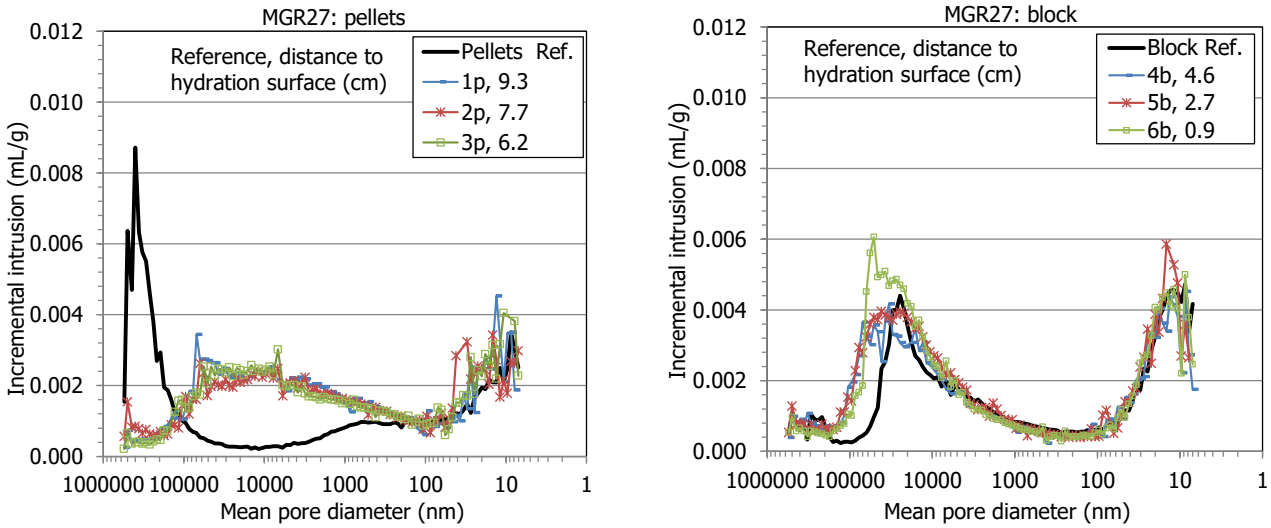

Figure A- 44. Pore size distribution of samples from pellets (left) and block (right)

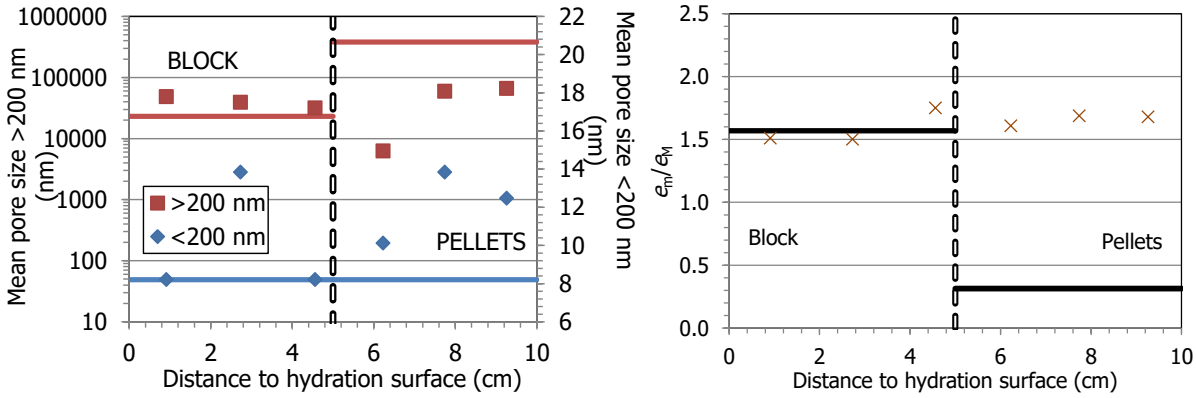

Figure A- 45. Test MGR27: Mean pore size for values above and below 200 nm (left); relation between void ratio corresponding to pores smaller (e_m) and larger (e_M) than 200 nm (right)

Table A- 36. Pore size distribution obtained with MIP, BET specific surface area and basal spacing of samples from test MGR25 (e: void ratio)

Reference	Distance to hydration (cm)	Intruded *e* (% of total)	*e* pores >200 nm (-)	Mode pores >200 (nm)	*e* pores <200 nm (-)	Mode pores <200 (nm)	BET a_s (m^2/g)	*t* -plot µ-pore volume (cm^3/g)	d_{001} (nm)
1p	9.3	53	0.337	66057	0.565	12	65	0.009	17.04
2p	7.7	54	0.324	59493	0.546	14	65	0.009	19.42
3p	6.2	56	0.328	6232	0.527	10	66	0.009	16.27
4b	4.6	57	0.312	31713	0.546	8	63	0.010	17.58
5b	2.7	60	0.350	39117	0.525	14	66	0.010	20.12
6b	0.9	60	0.360	48259	0.543	8	67	0.010	18.42
Pellets	-	36	0.819	378852	0.258	8	59	0.010	14.80
Block	-	68	0.302	20863	0.401	9	60	0.008	14.80

Figure A- 46. Appearance of the bentonite column after extraction from the test cell MGR27 (left: pellets, right: block)

TRANSPARENT CELL (CW)

TEST CW1

Table A- 37. Characteristics of test CW1

Characteristics	Data
Material bottom	FEBEX pellets (EB)
Material top	FEBEX block
Hydration, water, pressure	Through bottom, deionised water, 25 kPa
Duration	379 days, (Feb 2018 - Mar 2019)
Length	12.0 cm
Height	11.8 cm
Thickness	2.0 cm

Table A- 38. Final values along the column determined by mercury immersion and oven drying in CW1

Distance to hydration surface (cm)	Distance to left border (cm)	w (%)	ρ_d (g/cm^3)	S_r (%)
10.90	2.30	33.4	1.42	99
10.90	6.10	32.6	1.42	98
10.90	9.90	31.8	1.43	96
8.40	2.30	32.4	1.41	95
8.40	6.10	33.1	1.40	97
8.40	9.90	31.8	1.41	94
6.00	2.30	34.7	1.37	96
6.00	5.00	31.6	-	-
6.00	7.10	35.9	-	-
6.00	9.90	34.4	1.36	94
3.60	2.30	37.7	1.31	96
3.60	6.10	38.2	-	-
3.60	9.90	37.8	1.30	95
1.20	2.30	43.3	1.24	99
1.20	6.10	39.1	1.28	96
1.20	9.90	42.9	1.26	101

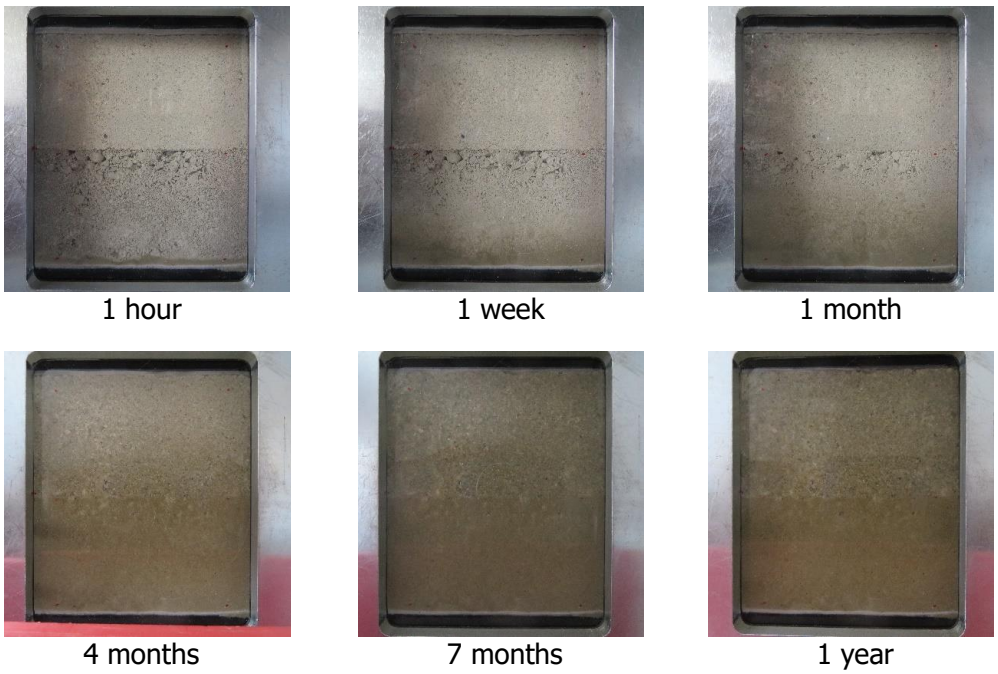

Figure A- 47. Comparison, in face B, of the evolution of the hydration front for six different moments of test CW1

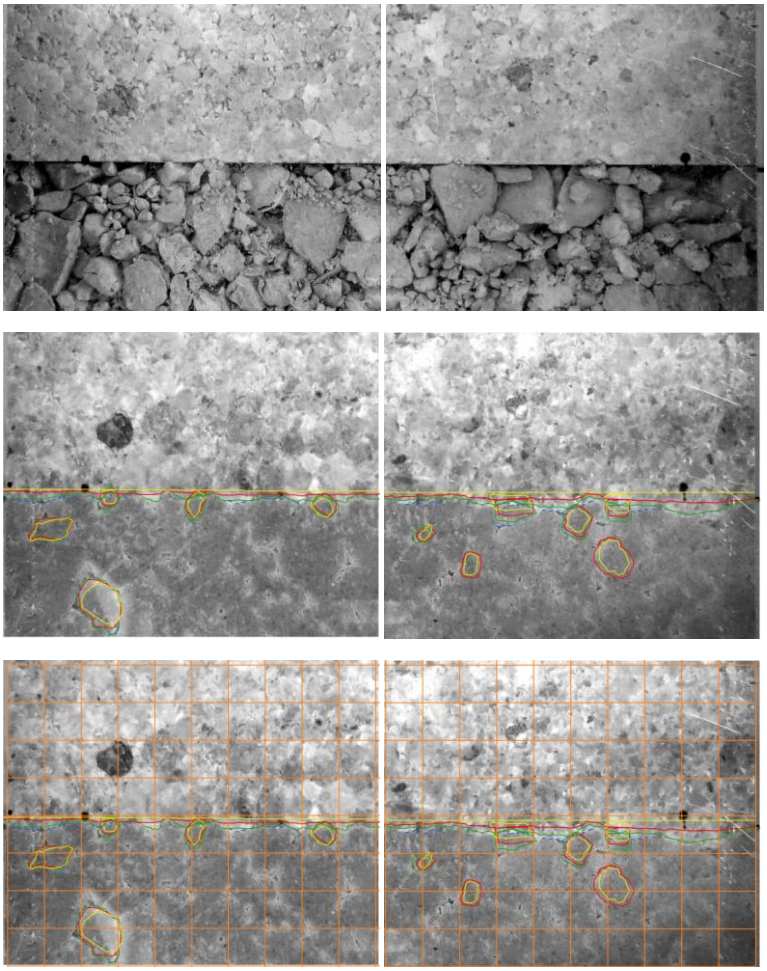

Figure A- 48. Texture evolution of the interface since the beginning of the CW1 test (yellow), after a month (red), after two months (green) and after three months of hydration (blue). A 5x5 mm mesh has been represented

Table A- 39. Pore size distribution and BET surface area obtained with MIP and adsorption isotherms and basal spacing obtained in wet sample by XRD of samples from test CW1 (e: void ratio, b: block, p: pellets, b/p: block and pellets)

Reference	Distance to hydration (cm)	Intruded *e* (% of total)	*e* pores >200 nm (-)	Mode pores >200 (nm)	*e* pores <200 nm (-)	Mode pores <200 (nm)	BET a_s (m^2/g)	*t* -plot µ-pore volume (cm^3/g)	d_{001} (nm)
CW1_1.1_b	10.85	66	0.425	25730	0.476	12	63	0.009	16.82
CW1_1.2_b	10.85	62	0.385	35223	0.517	11	63	0.009	18.33
CW1_1.3_b	10.85	58	0.377	23192	0.511	12	62	0.009	16.59
CW1_2.1_b	8.44	63	0.402	28569	0.513	15	63	0.010	16.02
CW1_2.2_b	8.44	61	0.408	28556	0.520	12	64	0.010	16.82
CW1_2.3_b	8.44	60	0.369	23178	0.546	11	64	0.010	16.45
CW1_3.1_b/p	6.03	68	0.504	20877	0.467	7	64	0.009	16.71
CW1_3.3_b/p	6.03	62	0.431	18814	0.554	11	64	0.010	19.15
CW1_4.1_p	3.62	66	0.551	35230	0.510	21	65	0.010	18.98
CW1_4.3_p	3.62	67	0.576	25728	0.501	10	68	0.010	18.59
CW1_5.1_p	1.21	52	0.555	6293	0.622	26	67	0.009	19.19
CW1_5.2_p	1.21	71	0.640	6241	0.469	12	66	0.009	19.01
CW1_5.3_p	1.21	64	0.657	6226	0.485	23	65	0.009	19.21
CW1_rA_b/p	6.03	28	0.090	6160	0.866	23	n.d.	n.d.	n.d.
CW1_rB_b/p	6.03	30	0.109	48228	0.792	15	n.d.	n.d.	n.d.
Pellets	-	47	0.826	277326	0.267	21	59	0.010	14.80
Block	-	68	0.302	20863	0.401	7	60	0.008	14.80

TEST CW2

Table A- 40. Characteristics of test CW2

Characteristics	Data
Material bottom	FEBEX block
Material top	FEBEX pellets (EB)
Hydration, water, pressure	Through bottom, deionised water, 25 kPa
Duration	420 days, (May 2019 - Jul 2020)
Length	12.0 cm
Height	11.6 cm
Thickness	2.0 cm

Table A- 41. Final values along the column determined by mercury immersion and oven drying in test CW2

Distance to hydration surface (cm)	Distance to left border (cm)	w (%)	ρ_d (g/cm^3)	S_r (%)
11	2.30	32.9	1.26	77
11	6.00	32.5	1.28	79
11	9.70	32.4	1.26	76
8.6	2.30	32.7	1.28	80
8.6	6.00	32.0	1.33	84
8.6	9.70	32.2	1.28	79
6.1	2.30	31.9	1.38	90
6.1	9.70	30.6	1.37	85
3.7	2.30	31.9	1.40	93
3.7	6.00	31.9	1.43	97
3.7	9.70	30.3	1.44	93
1.2	2.30	33.1	1.39	94
1.2	6.00	32.6	1.41	97
1.2	9.70	32.2	1.41	94

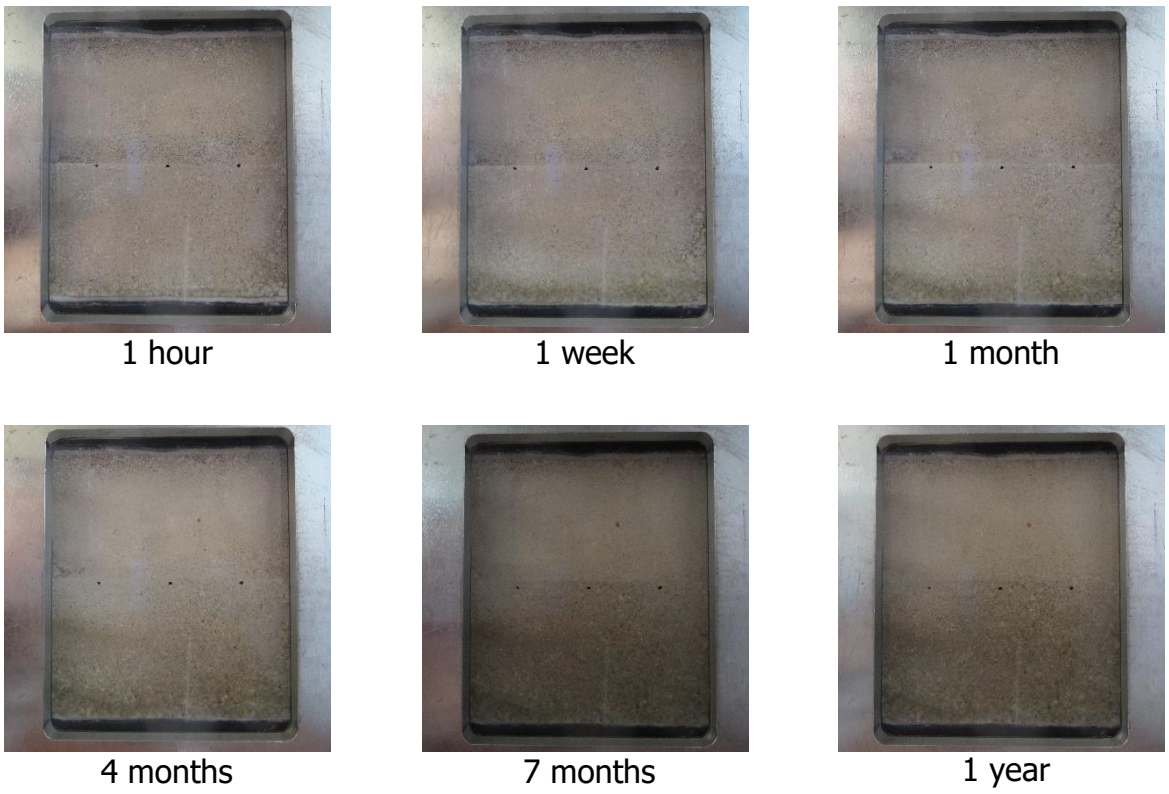

Figure A- 49. Comparison, in face B, of the evolution of the hydration front for six different moments in test CW2

Table A- 42. Pore size distribution and BET surface area obtained with MIP and adsorption isotherms and basal spacing obtained in wet sample by XRD of samples from CW2 (e: void ratio, b: block, p: pellets, b/p: block and pellets)

Reference	Distance to hydration (cm)	Intruded *e* (% of total)	*e* pores >200 nm (-)	Mode pores >200 (nm)	*e* pores <200 nm (-)	Mode pores <200 (nm)	BET a_s (m^2/g)	*t* -plot µ-pore volume (cm^3/g)	d_{001} (nm)
CW2_1.1_p	10.99	62	0.846	462369	0.297	7	63	0.009	17.81
CW2-1.2_p	10.99	58	0.755	9024	0.354	21	65	0.010	16.28
CW2-1.3_p	10.99	55	0.737	150250	0.406	17	63	0.009	15.56
CW2-2.1_p	8.55	59	0.771	6239	0.339	21	65	0.010	15.63
CW2-2.2_p	8.55	58	0.581	276906	0.449	8	63	0.010	15.69
CW2-2.3_p	8.55	52	0.821	110271	0.288	8	65	0.009	15.62
CW2-3.1_b/p	6.11	64	0.463	12351	0.493	11	63	0.009	15.42
CW2-3.3_b/p	6.11	61	0.412	28562	0.559	15	63	0.010	15.50
CW2-4.1_b	3.66	64	0.415	43391	0.513	14	64	0.010	15.27
CW2-4.2_b	3.66	63	0.372	43396	0.517	9	62	0.010	15.18
CW2-4.3_b	3.66	61	0.348	31702	0.527	11	66	0.010	15.48
CW2-5.1_b	1.22	76	0.531	39104	0.411	12	64	0.010	17.40
CW2-5.2_b	1.22	73	0.488	28546	0.427	15	65	0.010	15.80
CW2-5.3_b	1.22	67	0.429	31703	0.486	12	63	0.010	15.18
Pellets	-	47	0.826	277326	0.267	21	59	0.010	14.80
Block	-	68	0.302	20863	0.401	7	60	0.008	14.80

INSTRUMENTED CELL (CT31)

Table A- 43. Relative humidity, temperature and pressure recorded by sensors (sensor "up" placed at 12.8 cm from the bottom porous stone, sensor "mid" at 7.8 cm and sensor "dwn" at 1.3 cm)

Time (days)	RH-up (%)	RH-mid (%)	RH-dwn (%)	*T* (°C)	*P*-up (MPa)	*P*-mid (MPa)	*P*-dwn (MPa)	Pore *P* (MPa)
0	43	42	41	24	-0.01	-0.01	-0.02	0.09
1	43	43	-	25	-0.01	-0.10	0.70	0.11
2	43	44	100	25	-0.02	-0.14	0.69	0.09
3	43	45	100	25	-0.02	-0.15	0.70	0.09
4	43	47	100	25	-0.01	-0.28	0.84	0.09
5	43	48	100	25	0.00	-0.30	0.84	0.09
6	43	49	100	25	-0.03	-0.27	0.93	0.09
7	43	50	100	24	-0.03	-0.30	1.00	0.09
8	43	51	100	24	-0.03	-0.26	1.08	0.09
9	43	51	100	24	-0.03	-0.38	1.22	0.09
13	44	54	100	23	-0.03	-0.43	1.40	0.10
15	45	56	100	23	-0.04	-0.35	1.43	0.10
17	45	57	100	24	-0.02	-0.47	1.49	0.09
19	46	58	100	24	-0.02	-0.49	1.55	0.09
21	46	60	100	24	-0.01	-0.50	1.58	0.10
23	47	61	100	24	-0.01	-0.48	1.64	0.10
26	48	63	100	24	0.00	-0.42	1.74	0.09
29	49	65	100	24	-0.01	-0.27	1.83	0.10
33	50	67	100	24	-0.03	0.15	1.93	0.09
36	51	69	100	24	-0.01	0.71	2.00	0.10
39	52	71	100	23	0.00	1.16	2.14	0.10
41	52	72	100	23	0.00	1.51	2.18	0.09
45	53	73	100	23	0.00	2.13	2.22	0.10
51	55	76	100	23	0.01	2.68	2.38	0.09
57	57	78	100	23	0.02	3.10	2.48	0.10
63	58	79	100	23	0.03	3.47	2.54	0.09
69	61	81	100	26	0.05	3.67	2.64	0.10
75	62	82	100	23	0.05	3.97	2.68	0.09
81	64	83	100	22	0.08	4.02	2.76	0.09
87	66	84	100	22	0.08	4.11	2.88	0.10
94	68	85	100	24	0.13	4.18	2.87	0.09
100	70	86	100	21	0.12	4.26	2.97	0.09
106	71	87	100	22	0.13	4.29	3.03	0.09
112	73	88	100	21	0.15	4.30	3.10	0.10
118	75	88	100	23	0.16	4.24	3.06	0.09
131	78	90	100	22	0.15	4.24	3.23	0.10
156	83	92	100	20	0.10	4.25	3.34	0.10
168	85	92	100	21	0.11	4.10	3.40	0.10
180	86	93	100	24	0.08	4.04	3.38	0.11
192	88	94	100	22	0.10	4.01	3.45	0.10
204	89	94	100	23	0.19	3.97	3.44	0.11
228	91	95	100	24	0.54	3.91	3.54	0.10
240	92	95	100	22	0.78	3.90	3.57	0.10
254	92	95	100	23	1.04	3.98	3.54	0.10
263	93	96	100	24	1.22	3.98	3.62	0.10
275	93	96	100	23	1.44	3.96	3.65	0.10
288	94	96	100	22	1.61	4.09	3.75	0.10
300	94	96	100	23	1.75	4.09	3.70	0.10
324	95	97	100	23	1.99	4.17	3.81	0.10
337	95	97	100	23	2.12	4.15	3.80	0.10
351	95	97	100	23	2.22	4.23	3.84	0.10
363	96	97	100	24	2.34	4.26	3.89	0.10
375	96	97	100	23	2.42	4.33	3.89	0.09
387	96	97	100	23	2.53	4.32	3.95	0.09
399	96	98	100	22	2.64	4.33	3.99	0.09

Time (days)	RH-up (%)	RH-mid (%)	RH-dwn (%)	*T* (°C)	*P*-up (MPa)	*P*-mid (MPa)	*P*-dwn (MPa)	Pore *P* (MPa)
411	96	98	100	23	2.72	4.35	3.98	0.09
423	97	98	100	21	2.81	4.41	4.10	0.09
435	96	98	100	25	2.91	4.47	4.04	0.10
448	97	98	100	23	3.00	4.51	4.13	0.09
473	97	98	100	23	3.25	4.66	4.14	0.09
485	97	98	100	21	3.34	4.81	4.19	0.09
497	98	99	100	20	3.47	4.77	4.19	0.09
509	98	99	100	21	3.56	4.91	4.20	0.09
522	98	99	100	19	3.68	4.96	4.25	0.10
534	99	100	100	16	3.82	5.11	4.41	0.10
546	98	99	100	22	3.90	5.08	4.28	0.11
558	99	99	100	19	4.04	5.14	4.28	0.11
570	98	99	100	21	4.29	5.46	4.45	0.12
582	98	99	100	22	4.45	5.60	4.47	0.13
596	99	99	100	21	4.61	5.85	4.50	0.14
611	99	99	100	23	4.95	6.19	4.57	0.15
623	99	99	100	21	4.95	6.13	4.54	0.15
635	99	99	100	20	5.07	6.12	4.48	0.15
647	99	99	100	20	5.13	6.15	4.58	0.16
659	99	99	100	21	5.48	6.50	4.67	0.16
671	99	99	100	21	5.53	6.43	4.65	0.16
683	99	99	100	20	5.37	6.26	4.54	0.16
695	99	99	100	23	5.76	6.66	4.75	0.17
707	99	99	100	22	5.47	6.24	4.48	0.17
719	99	99	100	23	5.61	6.54	4.61	0.18
732	99	99	100	22	5.55	6.34	4.54	0.18
744	99	99	100	23	5.60	6.38	4.63	0.18
756	98	99	100	23	5.59	6.38	4.64	0.18
780	98	99	100	22	5.63	6.48	4.66	0.18
793	99	99	100	22	5.65	6.55	4.67	0.18
805	99	99	100	21	5.64	6.45	4.64	0.18
817	99	99	100	20	5.60	6.40	4.67	0.17
829	99	99	100	21	5.66	6.41	4.72	0.18
841	98	99	100	21	5.73	6.47	4.69	0.18
853	99	100	-	20	5.81	6.59	4.82	0.18
865	99	100	-	21	5.74	6.42	4.66	0.18
887	-	100	-	-	5.77	6.52	4.67	0.18
902	-	-	100	-	5.82	6.49	4.73	0.17
914	-	-	100	-	5.82	6.55	4.67	0.18

Table A- 44. Final water content (w), dry density (ρ_d) and degree of saturation (S_r) of the subsamples analysed

Reference	Section	Distance to bottom (cm)	Distance to axis (cm)	*w* (%)	ρ_d (g/cm^3)	S_r (%)
7X1	7P	1.00	6.10	32.9	1.42	95
7X5	7P	1.00	6.10	36.6	1.37	99
7Y1	7P	1.00	6.10	34.0	1.41	98
7Y5	7P	1.00	6.10	33.6	1.42	98
7X2	7P	1.00	3.35	32.5	1.45	99
7X4	7P	1.00	3.35	32.7	1.44	98
7Y2	7P	1.00	3.35	33.0	1.45	100
7Y4	7P	1.00	3.35	32.8	1.44	98
7XY3	7P	1.00	0.00	32.4	1.45	98

Reference	Section	Distance to bottom (cm)	Distance to axis (cm)	w (%)	ρ_d (g/cm^3)	S_r (%)
6X1	6P	3.00	6.10	29.5	1.51	97
6X5	6P	3.00	6.10	31.6	1.45	96
6Y1	6P	3.00	6.10	30.4	1.50	98
6Y5	6P	3.00	6.10	29.8	1.50	98
6X2	6P	3.00	3.35	30.0	1.49	97
6X4	6P	3.00	3.35	30.6	1.48	96
6Y2	6P	3.00	3.35	30.4	1.49	98
6Y4	6P	3.00	3.35	30.2	1.50	98
6XY3	6P	3.00	0.00	30.3	1.48	96
5X1	5P	5.00	6.10	28.8	1.52	96
5X5	5P	5.00	6.10	29.6	1.51	97
5Y1	5P	5.00	6.10	29.1	1.52	98
5Y5	5P	5.00	6.10	29.0	1.52	97
5X2	5P	5.00	3.35	29.1	1.51	96
5X4	5P	5.00	3.35	29.4	1.51	97
5Y2	5P	5.00	3.35	29.3	1.50	96
5Y4	5P	5.00	3.35	29.4	1.50	96
5XY3	5P	5.00	0.00	29.1	1.51	96
4X1	4BP	7.23	6.10	28.7	1.52	96
4X5	4BP	7.23	6.10	29.0	1.51	96
4Y1	4BP	7.23	6.10	29.2	1.52	98
4Y5	4BP	7.23	6.10	28.9	1.53	98
4X2	4BP	7.23	3.35	29.2	1.51	96
4X4	4BP	7.23	3.35	29.5	1.50	97
4Y2	4BP	7.23	3.35	29.3	1.51	97
4Y4	4BP	7.23	3.35	29.2	1.51	97
4XY3	4BP	7.23	0.00	29.2	1.51	97
3X1	3B	9.45	6.10	29.5	1.49	95
3X5	3B	9.45	6.10	29.2	1.49	94
3Y1	3B	9.45	6.10	29.4	1.50	96
3Y5	3B	9.45	6.10	29.2	1.51	96
3X2	3B	9.45	3.35	29.6	1.51	98
3X4	3B	9.45	3.35	29.6	1.50	96
3Y2	3B	9.45	3.35	29.5	1.50	96
3Y4	3B	9.45	3.35	29.3	1.50	96
3XY3	3B	9.45	0.00	29.6	1.50	97
2X1	2B	11.45	6.10	29.3	1.51	96
2X5	2B	11.45	6.10	29.6	1.49	95
2Y1	2B	11.45	6.10	29.4	1.50	96
2Y5	2B	11.45	6.10	29.4	1.50	95
2X2	2B	11.45	3.35	29.2	1.51	96
2X4	2B	11.45	3.35	29.3	1.50	95
2Y2	2B	11.45	3.35	29.3	1.51	96
2Y4	2B	11.45	3.35	29.5	1.50	97
2XY3	2B	11.45	0.00	29.1	1.50	95
1X1	1B	13.45	6.10	29.5	1.50	96
1X5	1B	13.45	6.10	30.4	1.46	94
1Y1	1B	13.45	6.10	29.8	1.49	96
1Y5	1B	13.45	6.10	30.1	1.48	95
1X2	1B	13.45	3.35	28.8	1.51	95
1X4	1B	13.45	3.35	29.4	1.51	97
1Y2	1B	13.45	3.35	29.5	1.50	96
1Y4	1B	13.45	3.35	29.1	1.50	96
1XY3	1B	13.45	0.00	28.8	1.51	95

Table A- 45. Pore size distribution and BET specific surface area obtained with MIP and adsorption isotherms of samples from test CT31 (e: void ratio)

Reference	Distance to hydration (cm)	Intruded *e* (% of total)	*e* pores >200 nm (-)	Mode pores >200 (nm)	*e* pores <200 nm (-)	Mode pores <200 (nm)	BET a_s (m^2/g)	t-plot µ-pore volume (cm^3/g)	d_{001} (nm)
1B	13.45	72	0.305	35233	0.516	21	34	0.004	1.53
2B	11.45	77	0.345	25729	0.476	19	35	0.004	1.55
3B	9.45	75	0.332	250894	0.489	19	32	0.004	1.56
4BP	7.23	69	0.329	28560	0.492	17	35	0.004	1.56
5P	5.00	73	0.332	66107	0.489	19	34	0.004	1.55
6P	3.00	74	0.358	31705	0.488	21	32	0.004	1.57
7P	1.00	72	0.372	31706	0.511	19	33	0.004	1.58
Pellets	-	-	-	-	-	-	31	0.004	-
Powder	-	-	-	-	-	-	25	0.004	-
Block	-	84	0.392	12362	0.442	19	-	-	~1.3


2695-8864